

A model for energy and morphology of crystalline grain boundaries with arbitrary geometric character

a Thesis by

Brandon Scott Runnels

in partial fulfillment of the requirements

for the degree of

Doctor of Philosophy



Division of Engineering and Applied Science
California Institute of Technology
Pasadena, California, United States of America

2016

(Defended June 15, 2015)

©2015

Brandon Scott Runnels

All rights reserved

To my family

Acknowledgments

I must begin by expressing my gratitude to my parents, Scott and Joy Runnels. In addition to providing me with constant support and encouragement during all of my academic endeavors, they homeschooled me from first grade through high school. All of my values—academic and otherwise—were instilled in me by them, and it is no exaggeration to say that this thesis is the result of their hard work as much as it is mine. I am also grateful for the encouragement and support (and delicious care packages) from my siblings and fellow *Runnels Mountain Academy* alumni: Joel, Rebecca, and Catherine.

I am indebted to my advisor, Professor Michael Ortiz, for his patience and guidance during my time at Caltech. It is a rare privilege to study under an individual with his breadth and depth of knowledge, and learning from him has been exciting and fulfilling. I was the beneficiary of his constant encouragement and kindness, particularly in the midst of my academic setbacks, and I am grateful for the opportunity to work with him.

I thank Dr. Irene Beyerlein, with whom I had the privilege of working for multiple summers at Los Alamos National Laboratory. Her enthusiastic support and efforts to help me with my research and career development (not to mention amazingly prompt feedback on papers and abstracts) were an integral part of my graduate studies. I would also like to thank Professor Dennis Kochmann, whose remarkably excellent teaching formed the foundation for my knowledge of solid mechanics, and who was always willing to help me with my various questions despite his busy schedule. I am also grateful to Professor Kaushik Bhattacharya for serving on my committee, taking the time to meet with me, and providing excellent guidance on variational methods and geometric measure theory. Finally, I am indebted to Professor Julia Greer for agreeing to serve as a fourth committee member at the last minute.

I have been truly blessed to be surrounded by wonderful fellow students and postdocs throughout

my Caltech experience. I would like to thank my fellow past and present research group members: Gwen Johnson, Landry Fokoua Djodom, Stephanie Mitchell, Stefanie Heyden, Jonathan Chiang, Panos Natsiavas, Sarah Mitchell, Arnold Durel Deffo Nde, Juan Granado, and Amuthan Ramabathiran. I would also like to thank Jeff Amelang, my MCE “big sib,” for his help and support; his family for the great conversations, dinners, and friendship; and Cindy Wang for always asking great questions. I thank my fellow MCE first-year students whose friendship was one of the highlights of my first year (and on whom I perpetually relied for help with problem sets): Lucas Meza, Chengyun Hua, Brock Bobbitt (and his family), Edward Burns, Vinamra Agrawal, and Hyun-Sik Kim.

I would like to express my gratitude to the Ortiz group support team. I am thankful to Lydia Suarez for the many conversations in her office and the enumerable kind words that always helped me to look on the bright side and, of course, for keeping everything running smoothly. I’m also grateful to Marta Kahl for taking care of all our computer needs and handling all of my computing questions.

In addition to my wonderful friends at Caltech, I had the privilege of getting to know many great people off-campus. I thank the Bible Study Fellowship crew for all of the wonderful Monday and Tuesday nights over the past two and a half years: Steve and Tina Quatro, Matthew and Carol Lynn Rothert, my fellow 2014-2015 leaders and the great group of guys that I had in my discussion group. I also thank my Cornerstone Bible Church extended family for reaching out to me; my thanks especially to Jon and Tammy Milhon for opening their home every week, Doug and Julie Davis for the lunches, Annaka Price for all the LA-area adventures, Steve and Allison Jung, Greg and Gloria Hendrix, Rich and Jeannie Springer, David and Denise Agron, and Lindsay Bruggman.

Last, but most importantly, I thank my Lord and Savior Jesus Christ. By him alone I am saved, through him alone I can do all things, and from him alone come all things worth studying.

“The heavens declare the glory of God; the skies proclaim the work of his hands. Day after day they pour forth speech; night after night they reveal knowledge.”

Psalm 19:1, NIV

Abstract

It has been well-established that interfaces in crystalline materials are key players in the mechanics of a variety of mesoscopic processes such as solidification, recrystallization, grain boundary migration, and severe plastic deformation. In particular, interfaces with complex morphologies have been observed to play a crucial role in many micromechanical phenomena such as grain boundary migration, stability, and twinning. Interfaces are a unique type of material defect in that they demonstrate a breadth of behavior and characteristics eluding simplified descriptions. Indeed, modeling the complex and diverse behavior of interfaces is still an active area of research, and to the author's knowledge there are as yet no predictive models for the energy and morphology of interfaces with arbitrary character. The aim of this thesis is to develop a novel model for interface energy and morphology that i) provides accurate results (especially regarding "energy cusp" locations) for interfaces with arbitrary character, ii) depends on a small set of material parameters, and iii) is fast enough to incorporate into large scale simulations.

In the first half of the work, a model for planar, immiscible grain boundary is formulated. By building on the assumption that anisotropic grain boundary energetics are dominated by geometry and crystallography, a construction on lattice density functions (referred to as "covariance") is introduced that provides a geometric measure of the order of an interface. Covariance forms the basis for a fully general model of the energy of a planar interface, and it is demonstrated by comparison with a wide selection of molecular dynamics energy data for FCC and BCC tilt and twist boundaries that the model accurately reproduces the energy landscape using only three material parameters. It is observed that the planar constraint on the model is, in some cases, over-restrictive; this motivates an extension of the model.

In the second half of the work, the theory of faceting in interfaces is developed and applied to the

planar interface model for grain boundaries. Building on previous work in mathematics and materials science, an algorithm is formulated that returns the minimal possible energy attainable by relaxation and the corresponding relaxed morphology for a given planar energy model. It is shown that the relaxation significantly improves the energy results of the planar covariance model for FCC and BCC tilt and twist boundaries. The ability of the model to accurately predict faceting patterns is demonstrated by comparison to molecular dynamics energy data and experimental morphological observation for asymmetric tilt grain boundaries. It is also demonstrated that by varying the temperature in the planar covariance model, it is possible to reproduce *a priori* the experimentally observed effects of temperature on facet formation.

Finally, the range and scope of the covariance and relaxation models, having been demonstrated by means of extensive MD and experimental comparison, future applications and implementations of the model are explored.

Contents

Acknowledgments	iv
Abstract	vi
Table of Contents	x
List of Figures	xiii
List of Tables	xiv
1 Introduction	1
1.1 Motivating applications	3
1.1.1 Multiscale modeling of material strength in extreme strain rate deformation	5
1.1.2 Grain boundary spallation	6
1.1.3 Accumulated roll bonded composites	7
1.2 Background	7
1.2.1 Crystallography	8
1.2.2 Measure theory	11
1.2.3 Nonconvex optimization	11
1.3 Organization of thesis	13
2 Literature Review	15

2.1	Interface energy models	15
2.1.1	Interface classification	16
2.1.2	Atomistic simulations	16
2.1.3	Current approaches	17
2.2	Relaxation	19
3	The Covariance Interface Energy Model	22
3.1	Theory	22
3.1.1	Problem definition and notation	22
3.1.2	Density measures of lattices	24
3.1.3	Thermalization by maximum entropy	25
3.1.4	Fourier expansions of convolved periodic measures	27
3.1.5	Lattice deformation	28
3.1.6	Interface covariance	29
3.1.7	Bounds on covariance	31
3.1.8	Microscopic degrees of freedom	32
3.1.9	Covariance as a measure of grain boundary energy	34
3.2	Results for homophase boundaries	37
3.2.1	Grain boundary geometry	38
3.2.2	Crystal structure and material parameters	39
3.2.3	FCC symmetric tilt grain boundaries	41
3.2.4	BCC symmetric tilt grain boundaries	42
3.2.5	FCC twist grain boundaries	43
3.2.6	BCC twist grain boundaries	45
3.3	Conclusions and future work	47
3.4	Acknowledgements	48

4	The Convexification Algorithm for Relaxed Energy and Morphology	49
4.1	Theory	49
4.1.1	Faceting construction	52
4.1.2	Convexification on the unit sphere	54
4.2	Implementation	56
4.2.1	Covariance model for interface energy	56
4.2.2	Stereographic projections of interface energy surfaces	57
4.2.3	Procedure	59
4.2.4	Computation of results	59
4.3	Examples	60
4.3.1	Symmetric tilt grain boundaries	61
4.3.2	Twist grain boundaries	65
4.3.3	Asymmetric tilt grain boundaries	70
4.4	Conclusion	78
4.5	Acknowledgements	79
5	Conclusions and Future Work	81
5.1	Summary	81
5.2	Future work	83
A	Positivity of Fourier Coefficients for FCC and BCC Lattices	84
B	Supplementary Validation	86
B.1	Molecular Dynamics	86
B.2	Experimental Energy Data	88
B.3	Read-Shockley Comparison	89
	Bibliography	102

List of Figures

1.1	Macro- and microscopic view of metal structure. (image credit: imsoup.com, wikipedia.org)	2
1.2	Spallation is often observed to occur at grain boundaries in materials undergoing rarefaction.	6
1.3	Accumulated roll bonded composites use a macroscopic manufacturing method to generate ultra-strong composites with an interface-dominated microstructure [22].	7
1.4	Nonconvexity and minimizing sequences.	12
3.1	We begin with a uniform crystal with no boundary (center). A symmetric tilt grain boundary is formed by symmetric rotation about an in-plane tilt axis (left). A symmetric twist grain boundary results from asymmetric rotation about the normal twist axis (right).	38
3.2	Optimal geometry of unit cells for FCC and BCC crystal structures.	39
3.3	FCC STGB results of the covariance model for Copper and Gold, compared with molecular dynamics results using the Embedded Atom Method (EAM) and Lennard-Jones (LJ) potentials. MD results from [41]. Annotations on the top indicate the boundary plane for the top crystal at cusp locations.	41
3.4	BCC STGB results of the covariance model for Molybdenum and α -Iron, compared with MD results using FS (for Mo) and Johnson (for Fe) potentials. MD results from [49]. Annotations on the top indicate the boundary plane for the top crystal at cusp locations.	43

3.5	FCC TwGB results of the covariance model for Copper and Gold, compared with MD results using EAM (for gold) and LJ (for copper). The boundary planes (constant for all twist angles) are indicated by the graph labels. MD results for symmetric twist from [42], asymmetric twist from [43].	44
3.6	BCC StwGB results of the covariance model for α -Iron, compared with MD results using a Johnson potential. MD data from [50,51].	45
3.7	BCC ATwGB results of the covariance model for Molybdenum and α -Iron, compared with MD results using a Finnis-Sinclair (FS) potential for Mo and a Johnson potential for Fe. MD results from [51].	46
4.1	We choose a coordinate system between the materials and add z , a perturbation to the interface.	50
4.2	Two plots of the same data demonstrating the connection between convexity in gradient space and convexity on the unit sphere. The “convex hull” on the unit sphere is equivalent to the convex hull of the energy multiplied by $\sqrt{1 + \nabla z ^2}$. (The shaded region is the Wulff construction.)	54
4.3	Faceting algorithm	58
4.4	Geometry of symmetric tilt grain boundaries	61
4.5	FCC STGB results of the covariance model (relaxed and unrelaxed) for Copper and Gold, compared with molecular dynamics results using the Embedded Atom Method (EAM) and Lennard-Jones (LJ) potentials. MD results from [41]. Annotations on the top indicate the boundary plane for the top crystal at cusp locations.	62
4.6	BCC STGB results of the covariance model (relaxed and unrelaxed) for Molybdenum and α -Iron, compared with MD results using FS (for Mo) and Johnson (for Fe) potentials. MD results from [49]. Annotations on the top indicate the boundary plane for the top crystal at cusp locations.	64
4.7	Geometry of asymmetric tilt grain boundaries.	66

4.8	FCC TwGB results of the covariance model (relaxed and unrelaxed) for Copper and Gold, compared with MD results using EAM (for gold) and LJ (for copper). The boundary planes (constant for all twist angles) are indicated by the graph labels. MD results for symmetric twist from [42], asymmetric twist from [43].	67
4.9	BCC StwGB results of the covariance model (relaxed and unrelaxed) for α -Iron, compared with MD results using a Johnson potential. MD data from [50, 51].	68
4.10	BCC ATwGB results of the covariance model (relaxed and unrelaxed) for Molybdenum and α -Iron, compared with MD results using a Finnis-Sinclair (FS) potential for Mo and a Johnson potential for Fe. MD results from [51].	69
4.11	Geometry of asymmetric tilt grain boundaries	71
4.12	MD data for Cu from [45, 47]. MD data for Al from [47].	72
4.13	Evolution of the facet microstructure for ϕ varying from 0° to 90°	74
4.14	Comparison of experimentally observed faceting in a $\{111\}\langle 112 \rangle$ ATGB with the relaxation method's predicted facet pattern.	75
4.15	Model prediction of energy for $\{111\}\langle 112 \rangle$ ATGBs in Copper. Results are presented for the planar model (dash), relaxed using 2-facets (thin), relaxed using 3-facets (thick). MD results computed with an EAM potential are included for comparison (dot-dash). MD data from [44].	76
4.16	Predicted evolution of the planar energy surface (thin line) and the relaxed energy surface (thick line) with the temperature σ ; shaded region is Wulff shape.	77
4.17	Experimentally observed faceting in Al changing with temperature [116, Figure 8a]. The superimposed white lines in the figures are an approximation of the interface using predicted facet slopes.	79
B.1	Model comparison with MD results for FCC and BCC Iron [113].	87
B.2	Comparison of the relaxed covariance model with experimental data for [100] and [110] STGBs in Cu. Experimental data for [100] STGBs from [29], for [110] STGBs from [118]	88
B.3	Model results for FCC Cu compared with the Read-Shockley model	89

List of Tables

3.1	Locations of atoms in the Fourier periodic unit cell for BCC, FCC, and HCP lattices. . .	40
3.2	Material parameter values used for materials in all GB tests	40
4.1	Material parameters for covariance model	57

Conventions

Acronyms

The following acronyms are used in this work:

ATGB Asymmetric tilt grain boundary

ATwGB Asymmetric twist grain boundary

BCC Body-centered cubic

CSL Coincident site lattice

EAM Embedded atom model

FCC Face-centered cubic

FS Finnis-Sinclair

GB Grain boundary

HCP Hexagonal close-packed

LJ Lennard-Jones pair potential

MD Molecular Dynamics

OR Orientation relationship

STGB Symmetric tilt grain boundary

STwGB Symmetric twist grain boundary

TwB Twist grain boundary

Nomenclature

To the extent possible, we follow standard conventions. Where new quantities are used, they are defined and used consistently throughout the work. The following is a reference for many of the commonly used symbols in this thesis.

$GL(n)$ The space of full-rank linear transformations in \mathbb{R}^n

$SO(n)$ The space of rotation matrices in \mathbb{R}^3

S_n The unit n-sphere

$[abc]$ Miller index notation for directions

$\langle abc \rangle$ Miller index notation for a family of directions

(abc) Miller index notation for (normal vectors to) planes

$\{abc\}$ Miller index notation for families of (normal vectors to) planes

γ Interface energy per unit area

ϱ Density measure

ρ Mollified (thermalized) density function

ψ Thermalization function

ϕ Window function

θ_E Density on a set E

c Covariance

C Normalized covariance

Chapter 1

Introduction

Why do we care about interfaces in crystalline materials? To the everyday observer, it is often not immediately intuitive that microscopic crystalline interfaces should be of any consequence: as there are no significant static effects on the visible length scale, effects of interfaces are often considered to be small enough to be safely ignored. However, despite the negligible effect of interfaces at the visible lengthscale, they play a much stronger role at the microscopic level. This counter-intuitive difference between the relative mechanical influence at these different levels is, in fact, a result of scaling laws. Interfacial effects scale with surface area, while other quantities, such as elastic or potential energy, scale with volume. Volume is proportional to the object's length cubed, while surface area scales as the length *squared*. Thus, we expect bulk effects to dominate at large scales, with surface effects dominating at small scales. Flypaper or Scotch tape provide a practical example of this effect. One can easily catch insects or dust with these sticky materials, because at the millimeter lengthscale the adhesive force (scaling with contact area) dominates the gravitational force (scaling with volume). On the other hand, a human could not be caught in the same way—even with an entire wall covered with flypaper or Scotch tape—because at the meter lengthscale, the forces scaling with volume dominate those scaling with surface area. The same is true with crystalline materials: though surface effects seem negligible to the observer, we should expect that they will eventually dominate (become “sticky”) at small enough scales. Thus, it is important to account for area-scaling effects in order to understand the mechanics of a wide variety of micromechanical processes.

Effects of this type are visible in many cases. Surface tension in liquids and interfacial energy in



Figure 1.1: Macro- and microscopic view of metal structure. (image credit: imsoup.com, wikipedia.org)

multimaterial composites are some examples of area-scaling phenomena. For this work, the example of interest are **grain boundaries** (GBs). As shown in Figure 1.1, most metals used in structural applications are composed of microscopic grains, distinguishable from one another only by their crystallographic orientation. The interface separating two grains is referred to as a grain boundary. Grain boundaries affect the macroscopic properties of the material in many ways; for instance, grain boundaries raise the yield strength of the material by restricting dislocation transmission and, consequently, effecting the obstruction of plastic flow. GBs are often treated isotropically; that is, all GBs are treated the same way regardless of the relative crystallographic orientation. However, grain boundaries exhibit strong anisotropy, so understanding and modeling this anisotropy is of great importance in understanding, modeling, and creating strong materials.

Materials are exceedingly complicated mechanical systems and all effective material models must take into account a wide range of mechanisms by which the material body responds to physical inputs. The best way to account for all of these competing mechanical effects is by means of variational (or energy) methods. Variational methods provide an elegant and efficient mathematical framework for studying complex mechanical processes. By computing the energy of each competing mechanical process, one can show that the combined result is computed simply by minimizing the total energy, and it can always be guaranteed that the minimizing result satisfies the conservation constraints on the system. From a modeling perspective, variational methods are convenient because they allow a formulation of a model using generalized degrees of freedom, essentially decoupling the materials physics from the kinematics

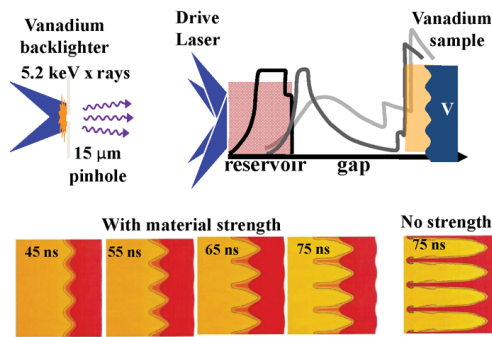
and geometry of the system. Additionally, solving a problem with a variational structure allows for a modular approach where the different physical mechanisms are isolated from each other until the final minimizing step. As such, modeling of interfaces and grain boundaries is done most conveniently by formulating a model for their energy.

Over the course of the past two centuries or so, but even more within the past several decades, the focus of a great deal of research has been directed towards understanding and characterizing how materials behave at microscopic scale in order to understand, quantify, predict, and even design their behavior on the macroscopic scale. Broad and extensive work has been done to model a variety of micromechanical phenomena, but study of the behavior of grain boundaries is comparatively undeveloped. In fact, to the best of the author's knowledge, there are no models that can robustly predict grain boundary energy for an arbitrary homophase configuration. Indeed, the grain boundary community has yet to reach consensus even on the dominant mechanisms involved in determining grain boundary energy: though it has been proposed many times that the anisotropy is driven by geometry, no geometric quantity has yet been produced that consistently correlates to grain boundary energy.

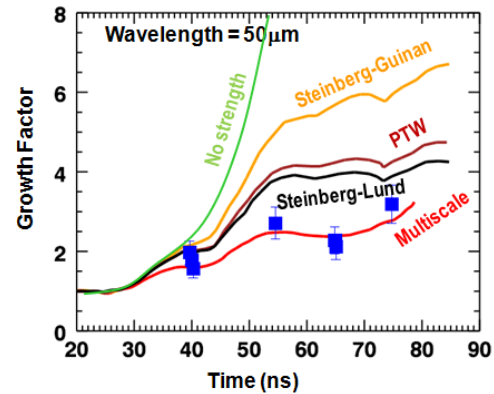
In this work we present a new model for anisotropic grain boundary energy. The development proceeds in two stages. First, we propose a model for strictly planar grain boundaries, and we show that it is i) able to find location of energy minimizers in configuration space, ii) defined for an GB with arbitrary configuration, and iii) computationally efficient. Second, following previous work, we describe the variational principle for GBs from which a faceting scheme for relaxation is constructed. We then are able to show that the relaxation scheme combined with the grain boundary energy model accurately reproduces the relaxed energy and interfacial morphology of a wide range of crystals. We note here that the work in this thesis is taken from current work of the author along with Dr. Irene Beyerlein, Professor Sergio Conti, and Professor Michael Ortiz [1, 2].

1.1 Motivating applications

The applications for grain boundary energy research are wide and varied. Recrystallization [3], microstructure formation in solidification [4], and microstructure evolution [5] are all examples of phenom-



(a) Schematic of a high strain rate Rayleigh Taylor experiment in a vanadium rippled surface [16].



(b) Comparison of computational modeling attempts, with a close match obtained using a multiscale approach [17].

ena that are significantly influenced by grain boundary anisotropy. Because of the many cases in which grain boundaries play a significant role, it is of great interest to be able to understand and predict the free energy of grain boundaries in a broad range of cases.

In addition to predicting the energy of grain boundaries, it is also of interest to predict their morphology. The need for predictive morphological modeling is motivated by many observations and applications. In particular, faceted interfaces (interfaces with a piecewise affine zig-zag structure) are ubiquitous in experimental observation and molecular dynamics simulations [6]. Some of the observed phenomena influenced by faceted interfaces are deformation twinning [7], interface sliding under deformation [8], interface mobility [9–14], and solidification [15]. Because they are frequently observed and because their discrete and ordered structure is conducive to analysis, faceted grain boundaries and interfaces are of great interest.

Of particular relevance to GB energy and morphology research are the applications towards high energy physics simulations and multiscale modeling, spallation at grain boundaries, and optimal manufacturing of accumulated roll bonded composites. We discuss these applications briefly in the following sections.

1.1.1 Multiscale modeling of material strength in extreme strain rate deformation

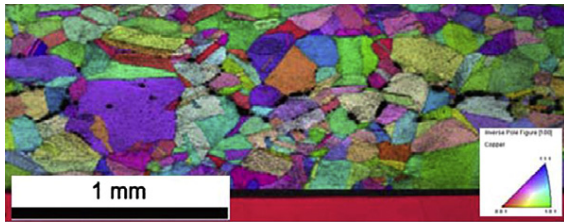
Knowledge of material behavior in extreme dynamics and environments is of great importance in a wide range of applications. For the military, knowledge of extreme material properties is crucial in the design of weapons and shielding. Other applications of relevant high energy density materials physics include, for example, the mechanics of inertial confinement fusion.

To this end, there is a great experimental effort to observe and characterize these high strain rate properties. One example is illustrated in Figure 1.2a. This figure illustrates an experimental apparatus in which a drive laser is used to cause a shock wave to propagate through a rippled interface in a sample of vanadium. By examining the growth rate of the ripples, it is possible to quantitatively characterize the role of material strength in this extreme environment.

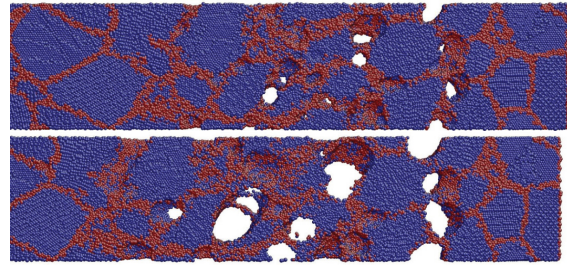
Experiments provide valuable insight into high energy density material behavior, but are inherently difficult and expensive operation. In order to predict material behavior in a wide range of high energy density cases, there is a great need for accurate material models for large-scale simulations. The creation of accurate extreme models for materials is a highly active research area.

There are many types of approaches to material behavior at high strain rates ranging from *ab initio* to heuristic. Recently, the multiscale materials modeling paradigm has gained traction as a possible means of predicting material behavior without relying on empirical models. Many of the results have been promising: Figure 1.2b illustrates the predicted ripple growth rate from a variety of simulations using different material strength models with drastically differing results. Clearly the multiscale model predictions are the most reliable.

The goal of multiscale modeling is, broadly speaking, to capture the effects of a wide variety of material behavior on multiple length and time scales. While material behavior is generally well-characterized (if only phenomenologically) on the large scale, there are many physical phenomena that can only be explained by linking the large scale response to small scale phenomena. However, because of the vast difference in scaling, it is unfeasible to resolve small scales completely if a large simulation is to be run. Thus the challenge is to bridge scales by creating large scale models informed by small scale physics. To this end, grain boundaries play a strong role. In addition to the GB-related effects described above,



(c) Experimental results for copper [19].



(d) MD simulation results for lead [20].

Figure 1.2: Spallation is often observed to occur at grain boundaries in materials undergoing rarefaction.

GB energy models are able to inform and improve existing models for other mechanical models, such as models of microstructure and phase transition in which GBs energy determines the length scale of energy-minimizing laminated microstructure [18].

1.1.2 Grain boundary spallation

A specific high energy density mechanism of great interest is the behavior of materials undergoing extreme tension. By applying a near-instantaneous application of a very high pressure to a sample of material, a shock wave is created that propagates through the material. Because failure rarely occurs under pure compression, materials generally do not fail under compressive shock loading. However, when the shock reaches the free end of a material the compressive shock can no longer be sustained. As a consequence of the conservation of energy and momentum, a resulting tensile wave (called a rarefaction wave) is reflected from the free end that propagates back through the material. When a rarefaction wave encounters a free surface, the response is another wave propagating in the opposite direction. This can create a region in the material where the rarefaction wave overlaps itself, causing the tensile stress to double. This often causes failure in the material by the creation and unstable growth of small nanovoids. This is referred to as *spallation*, and is a significant effect in many large-scale applications.

Grain boundaries have been observed to play a significant role in spallation during rarefaction. Particularly, grain boundaries with higher energy are more likely to spall than those with low energy [21]. Consequently, it is important to account for grain boundary anisotropy when analyzing and designing materials designed to undergo shock loading.

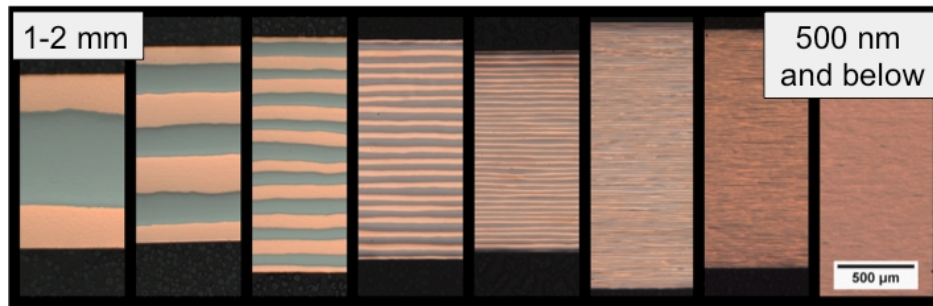


Figure 1.3: Accumulated roll bonded composites use a macroscopic manufacturing method to generate ultra-strong composites with an interface-dominated microstructure [22].

1.1.3 Accumulated roll bonded composites

Accumulated roll bonded (ARB) composites are a class of composites created using severe plastic deformation (SPD). ARB show great promise due to their high strength and straightforward method for manufacture. It has been demonstrated that at high layer density layer evolution is dominated by interface mechanics [23, 24]. To be able to maintain layer stability for very small laminate scales, it is necessary to understand the mechanics of the interfaces as well. By accurately understanding and modeling the mechanics of grain boundaries, the same modeling approach may be extended towards general multi-material applications.

1.2 Background

Work in the mechanics of materials at very small scales frequently is said to lie in “the intersection of materials science and engineering” and, as such, motivates the need for a brief discussion of some of the techniques used. Because (as is concluded) grain boundary energy is driven by geometrical effects, it is essential to lay the groundwork for working with crystallographic terminology. On the other hand, the implementation of the covariance model for grain boundary energy relies initially on some of the developments in measure theory, and the formulation of the convexification method for relaxation uses some of the developments in the calculus of variations. Therefore we include a brief discussion of some of the mathematical preliminaries upon which the theory is built.

1.2.1 Crystallography

In this work, interfaces between exclusively crystalline materials are considered, where by “crystalline” it is implied that the material is made up of lattices of atoms. A broad range of lattices occur naturally, but in this work, all are assumed to be of the “Bravais” variety. A Bravais lattice in an n -dimensional space is one generated by integral combinations of basis vectors; for instance, $\mathbf{r}(l, m, n) = l\mathbf{a} + m\mathbf{b} + n\mathbf{c}$ generates the lattice by enumerating atomic sites indexed by the integers l, m, n , given lattice basis vectors $\mathbf{a}, \mathbf{b}, \mathbf{c}$.

Another concept that will be used here is the crystallographic *unit cell*. The unit cell, defined informally, is the smallest subsection of a Bravais lattice that generates the entire crystal structure. Some lattices are conveniently represented by cubic unit cells and are referred to as “cubic lattices.” **Body-centered cubic** (BCC) lattices are one example: the BCC unit cell has an atom at each corner of the cube and an additional atom in the center. **Face-centered cubic** (FCC) lattices similarly have an atom located at each corner of the cube; the remaining atoms are located at the center of each face. Here and subsequently, we treat cubic lattices only.

Unit cells provide a basis for describing crystallographic geometry that is more convenient than the Bravais basis, because the Bravais vectors are generally not orthogonal, even for FCC and BCC lattices. Geometric quantities defined relative to the unit cell are generally defined using triplets of integers lmn referred to as Miller indices. (By convention, an overbar is used to denote negativity, e.g. $\bar{5} \equiv -5$.)

Vectors (often referred to as “directions”) are denoted using Miller indices with square brackets, e.g. $[lmn]$. Crystallographic planes are denoted using parentheses, e.g. (lmn) , where the indices lmn are the indices of the vector normal to the surface. Mathematically, crystallographic directions correspond to vectors in \mathbb{R}^3 (column vectors) whereas crystallographic planes correspond to 1-forms (alternatively: covectors, dual vectors, row vectors). Cubic materials generally have high symmetry, and so many directions/planes differ only by the coordinate system used to describe them. Therefore, generalized directions and planes are often used to denote families of directions/planes that are crystallographically identical. Angle brackets denote families of directions, e.g. $\langle lmn \rangle$; curly braces denote families of planes, e.g. $\{lmn\}$. In general, use of direction/plane family notation is kept to a minimum in this work to

avoid ambiguity.

Of primary interest in this work is the crystallographic conventions needed to precisely and consistently characterize boundaries between two crystalline bodies. To begin let us consider two semi-infinite Bravais lattices occupying the halfspaces $\{\mathbf{x} \in \mathbb{R}^3, x_3 > 0\}$, $\{\mathbf{x} \in \mathbb{R}^3, x_3 < 0\}$; without loss of generality adopting the convention that \mathbb{R}^2 is the boundary plane.

Suppose that for each crystal there exists a reference configuration. Then the top and bottom crystals are generated by the images of their reference configurations under the mappings $\phi^\pm(\mathbf{x}) = u^\pm(x_3)(R^\pm\mathbf{x} + \mathbf{t}^\pm)$, where u^\pm are the indicator functions for the upper/lower halfspaces, $R^\pm \in SO(3)$ are rotation transformations, and $\mathbf{t}^\pm \in \mathbb{R}^3$ are offset vectors. The rotations R^\pm are referred to as macroscopic degrees of freedom and the offsets \mathbf{t}^\pm as microscopic degrees of freedom. General categorization of grain boundaries considers the macroscopic DOFs only; that is, an implicit minimization with respect to \mathbf{t}^\pm is assumed.

By parameterizing all grain boundaries using pairs of upper and lower rotations, the space of all GBs can be represented as the direct product $\mathcal{I} = SO(3) \times SO(3)$. The definition of the operation

$$R_X R_Y = (R_X^+ R_Y^+, R_X^- R_Y^-) \quad R_{X,Y} = (R_{X,Y}^+, R_{X,Y}^-) \in \mathcal{I} \quad (1.1)$$

gives \mathcal{I} the structure of a Lie group. The requirements of closure, associativity, and identity/inverse elements follow from the Lie group structure of $SO(3)$. Then we observe that $\dim(\mathcal{I}) = \dim(SO(3)) + \dim(SO(3)) = 6$, the topological dimension of the corresponding Lie manifold

We identify an equivalence class on the elements of \mathcal{I} corresponding to grain boundaries that are identical up to mutual rotation of both halves about the grain boundary normal. We define the equivalence relation \sim on \mathcal{I} : for $R_X = (R_X^+, R_X^-)$, $R_Y = (R_Y^+, R_Y^-) \in \mathcal{I}$

$$R_X \sim R_Y \Leftrightarrow \exists R \in \text{im}(f) \text{ s.t. } R_1^X = R R_1^Y, R_2^X = R R_2^Y, \quad (1.2)$$

where $f : SO(2) \rightarrow SO(3)$, the embedding of $SO(2)$ corresponding to the set of rotations about the grain boundary normal. This definition is cumbersome, so we define \sim alternatively in terms of the Lie

subgroup

$$\mathcal{I}_2 = \{(R^+, R^-) \in \mathcal{I} : R^+ = R^- \in \text{im}(f)\}. \quad (1.3)$$

The reader may verify that, as before, the Lie group structure follows from the structure of $SO(2)$. It is easily shown that \mathcal{I}_2 is isomorphic to $SO(2)$; consequently $\dim(\mathcal{I}_2) = \dim(SO(2)) = 1$. With this definition we write \sim as

$$R_X \sim R_Y \Leftrightarrow R_X R_Y^{-1} \in \mathcal{I}_2. \quad (1.4)$$

This definition of the equivalence relation allows us to quantify the set of unique grain boundary orientations as the quotient group \mathcal{I}/\sim or $\mathcal{I}/\mathcal{I}_2$, the set of equivalence classes in \mathcal{I} . We see that $\dim(\mathcal{I}/\mathcal{I}_2) = \dim(\mathcal{I}) - \dim(\mathcal{I}_2) = 6 - 1 = 5$ and conclude that the space of grain boundary configurations has topological dimension of 5.

It is possible that other equivalence classes exist that may further reduce the topological dimension of the space of grain boundaries; such a reduction would make the problem of interface characterization and energy quantification significantly easier. Some work has been done that may indicate such a reduction [25, 26], but for now, we will treat the space of grain boundary configurations as five-dimensional.

A more intuitive argument for the 5d domain follows by considering the interface as being defined by two quantities: the *orientation relationship* (OR) and the interface orientation. Again assuming the existence of a reference configuration for both lattices, one may find a transformation matrix $R^+(R^-)^T$ that maps from the bottom crystal's orientation to the top. This set of relative orientations is $SO(3)$. Now, with the OR fixed, the interface is allowed to vary from its original orientation. This set of interface orientations is S_2 , the unit 2-sphere. All interfaces can be represented in this way. Thus the space can be represented as the direct product $SO(3) \times S_2$ so that $\dim(SO(3) \times S_2) = 3 + 2 = 5$. This characterization is generally more convenient when discussing classes of interfaces, and references to the orientation and interface orientation will be made extensively in this work.

1.2.2 Measure theory

In the formulation of the covariance model, it is convenient to introduce a function that describes the geometry of each crystal. In the case of a rigid lattice with no thermal atomic vibrations, a natural description of the lattice is as a collection of point masses. In order to describe point masses mathematically, it is necessary to use measures.

Before discussing measures, it is necessary to introduce the concept of “generalized functions” or “distributions.” Distributions are defined strictly in functional form; for instance, the Dirac distribution is defined in terms of test functions as

$$\delta[\phi(x)] = \phi(0) \quad (1.5)$$

for any (well-behaved) function ϕ . Building on this definition it is possible to define derivatives, transforms, and most of the usual properties of functions for distributions, in terms of the test function.

Measures, then, are distributions that have the additional constraint of i) non-negativity for positive valued functions and ii) value of zero for the null set. The Dirac distribution (and additive combinations thereof) is also a measure, and this allows the use of more restrictive mathematical tools. In this work, Dirac measures are used to represent point densities of atoms for a lattice in which each atom is considered to be absolutely rigid (i.e., at a temperature of absolute zero.)

1.2.3 Nonconvex optimization

The section on convexification for relaxed energy and morphology relies heavily on many of the developments in the mathematical fields of optimization and the calculus of variations. These tools have been applied widely with great success to many problems in mechanics ranging from crystal plasticity to microstructure of martensite. Specifically, in the context of variational methods in mechanics, it has been shown that in order to minimize energy, materials tend to form very fine alternating microstructures when the energy functional is *nonconvex*. Here, a brief introduction to convexity and nonconvex optimization is presented.

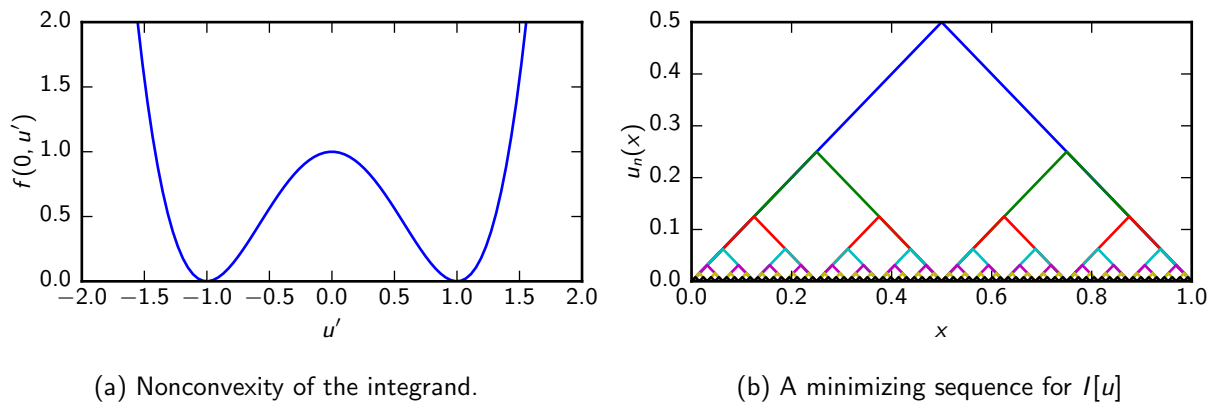


Figure 1.4: Nonconvexity and minimizing sequences.

A function over a linear space $f : V \rightarrow \mathbb{R}$ is said to be *convex* if

$$f(\lambda x + (1 - \lambda)y) \leq \lambda f(x) + (1 - \lambda)f(y) \quad \forall x, y \in V, \lambda \in [0, 1]. \quad (1.6)$$

This is the *zeroth-order* convexity inequality and only requires $f \in C_0(V)$. It may be described informally by stating “ f is convex if it lies on or below its chords.” If $f \in C_1(V)$ then an equivalent inequality for convexity is

$$f(y) \geq f(x) + \nabla f(x)^T (y - x) \quad \forall x, y \in V. \quad (1.7)$$

This is the *first-order* convexity inequality, and may be informally described by stating “ f is convex if it lies above its tangent planes.” Finally, restricting $f \in C_2(V)$, an equivalent inequality is

$$x^T \nabla^2 f(y) x^T \geq 0 \quad \forall x, y \in V, \quad (1.8)$$

where $\nabla^2 f$ is the Hessian matrix. This is the *second-order* convexity inequality and may be described informally by stating “ f is convex if its second derivative is positive-definite.” For a function f it is useful to define f_C the greatest possible convex function on or below f . f_C is referred to as the *convex envelope*, the *convexification*, or as the function of the *convex hull* of the epigraph of f .

A common example of the consequence of nonconvexity can be seen in the following functional

$I : C_0([0, 1]) \rightarrow \mathbb{R}^+$.

$$I[u] = \int_0^1 f(u, u') dx = \int_0^1 \left((u'(x)^2 - 1)^2 + u^2(x) \right) dx. \quad (1.9)$$

It is easily seen that $I \geq 0$ for all u , so a u^* such that $I[u^*] = 0$ is a minimizer. But does such a u^* exist? From the second part of the integrand we get that a minimizer must $u(x) = 0 \quad \forall x$. But from the first part of the integrand we see that a minimizer must also satisfy $u'(x) = \pm 1$ for all $x \in [0, 1]$. This indicates that f is nonconvex in its second argument, as shown in Figure 1.4a. We see that these two competing terms drive the minimizing function to create infinitesimally small corrugations with slope ± 1 , as shown in Figure 1.4b, but arbitrarily small value; that is

$$\liminf_{z \rightarrow 0} I[z] = 0. \quad (1.10)$$

Thus, it is impossible to actually attain the minimum, rendering the problem ill-posed. There are two possible solutions: in the present example, one can regularize the solution by adding $(u''(x))^2$ to the integrand. Alternatively, one can define the relaxation

$$I_C[z] = \liminf_{\bar{z} \rightarrow z} I[\bar{z}] = 0, \quad (1.11)$$

which, as can be demonstrated, is equivalent to the convexification of I . This technique forms the groundwork for the algorithm proposed in the chapter on relaxation, where notions of convexification for interfaces will be discussed.

1.3 Organization of thesis

The work is presented in the following way. We present a literature review surveying the broad range of previous work in Chapter 2. We develop the covariance model for grain boundary energy of planar interfaces in Chapter 3 and present a selection of examples for validation. We then develop the relaxation algorithm in Chapter 4 and present examples of its use with the covariance model towards a wide variety

of grain boundaries applications. Finally, in Chapter 5, we present a summary of the covariance and relaxation models and then briefly discuss future directions.

Chapter 2

Literature Review

The work in this thesis is intended to contribute to the field of interface energy by the development of a novel grain boundary energy model. As such, in order to give the proper context for a new energy formulation, it is essential to give a broad overview of the previous work done towards the same objective. The work can be divided cleanly into two sections: the development of planar (unrelaxed) rigid models, and the prediction of relaxation via faceting. The content of this chapter is taken from current work by the author on the development of the covariance model [1], and from the work on the convexification method [2].

2.1 Interface energy models

Developing models for interfaces has been a subject of research for many decades. They are unique among material defects in their variety and complexity, and attempts to characterize them in a general sense are ongoing. The plethora of interface models is as wide and varied as the selection of interfaces themselves, and elude many attempts to cohesively organize and categorize them. Approaches range from ab-initio quantum-based methods to heuristic geometrical constructions, and in the following subsections we discuss some of the most prominent.

2.1.1 Interface classification

The space of interface configurations is exceedingly large, and it is in general difficult to identify one unifying characteristic to which the energy of each interface can be linked. Consequently it becomes necessary to distinguish between and create models for different interface types. Interfaces between like materials are referred to as **grain boundaries**. The simplest types of non-trivial grain boundaries are **twin boundaries**, which require no displacement of individual atoms in either lattice from the reference in order to maintain registry at the boundary. Twin boundaries have the highest degree of order possible in a non-trivial interface and have relatively low energy.

Many types of high-order boundaries are not twin boundaries, but have a high degree of order and locally minimize the energy. Energy minimizing configurations in the space of interface energy orientations form **energy cusps** near their location in configuration space [27–29]. Though the interfaces themselves are well-understood, a current challenge is to find the locations of the cusps from which the stability of interfaces in configuration space can be assessed.

The remainder of interface types are **low-order boundaries** due to the large rotation required to obtain them from the nearest high-order boundary, and quantifying their energy can present a challenge for low order models.

2.1.2 Atomistic simulations

It is difficult to obtain experimental data for the energy of grain boundaries, and we are not aware of the existence of enough data for validating a model for the energy of a general GB. Thus, to validate low-order models in lieu of raw experimental energy data, the common approach is to recourse to atomistic simulations. Other than solving Schrödinger's equation directly, the most fundamental method for computing interface energy is density functional theory (DFT), which solves a reduced formulation of the ground state energy eigenproblem in terms of the electron density. DFT has been used to examine the properties of some grain boundaries and interfaces [30, 31]. However, computing energy for a wide range of grain boundaries is currently prohibitively expensive, although we anticipate improvements in the DFT theory that will make grain boundary and interface computations more feasible [32].

The phase-field crystal method is an atomistic approach that has recently gained some popularity [33–35]. It has been applied to grain boundary migration [14] and computation of GB energy [36].

Currently the *de facto* method for studying grain boundary energy is molecular dynamics (MD) [37]. The typical computational procedure is to create adjacent lattices of atoms, apply periodic boundary conditions, and relax to static equilibration by minimizing the energy calculated with an interatomic potential. All MD simulations require the use of interatomic potential. The simplest types of potentials possible are empirical or effective pair potential, such as Lennard-Jones (LJ). Significant fundamental shortcomings were found with the use of pair potentials [38], and the most commonly used potential in modern interface calculations is the Embedded Atom Model (EAM) potential [39]. However, it has been observed that, though often insufficient, pair potentials tend to give the correct result when computing grain boundary energy [40]. The literature is rich with MD data on a wide variety of subsets of the five-dimensional configuration space of interfaces. Data for FCC-FCC [41–48], BCC-BCC [49–51], HCP-HCP [52, 53], and FCC-BCC [6, 54] provide solid benchmarks for model verification.

2.1.3 Current approaches

Perhaps the most satisfying and physically justifiable low-order models for interface energy are those that build on the firmly established theory of dislocations. Theories of this nature rest upon the assumption that the interface possesses a sufficient degree of order so that distinct interfacial defects can be identified. This perspective can be traced back to the original insight of G.I. Taylor [55] whose treatment of dislocation surfaces led to the celebrated work of Read and Shockley [56]. They considered a generic low-angle tilt boundary between two cubic lattices, and used geometry to determine the dislocation density. By using the solution for the stress state resulting from ordered infinite rows of dislocations, they were able to compute the interaction analytically and to integrate the expression, obtaining the classic equation for tilt interface energy as a function of tilt angle $E = E_0\theta[A - \ln \theta]$. The model has been shown to work well for low angle tilt, and Wolf demonstrated that the model can be adapted to large-angle tilt boundaries to some degree [57], although this relationship is generally recognized as strictly empirical [58]

Read and Shockley's contemporary, JH van der Merwe, approached the problem of interface energy by devising a periodic interplanar potential and solving for the elastic response of the interface for symmetric tilt grain boundaries [59–61]. In a similar vein, Bullough extended the established theory of Peierls-Nabarro [60] for edge dislocations to symmetric tilt boundaries by treating interfaces as arrays of evenly spaced edge dislocations [62].

It has been observed empirically that the crystallography of many interfaces drives the energy; e.g., that most FCC crystals have similar GB anisotropy (up to a multiplicative constant) [63]. As a result, a reasonable hypothesis is that models informed heavily by geometry may ultimately be the most predictive. Several have been proposed that connect the energy of an interface to a geometrically determined quantity, and we discuss some of them below.

No geometric quantity is more commonly encountered in interface theory than the coincident site lattice (CSL) construction. When two misoriented lattices are adjacent to each other, the set of lattice sites common to both form an additional lattice, called the coincident site lattice. The ratio of the area of the CSL unit cell to the area of the lattice unit cell gives the so-called “ Σ ” value of the interface. Because low Σ values correspond, in general, to low energy grain boundaries, the CSL has been proposed as a model for GB energy [64, 65]. However the validity of such models has been questioned [66] and even now there is no general consensus about its reliability for grain boundary energy [67].

The “structural unit model” is a well-known geometric approach [68–72]. This is a heuristic method that attempts to characterize interfaces by determining the requisite structures needed for (or resulting from) compatibility between the crystals. The model is helpful in understanding the geometry of an unstructured interface, but it does not provide a means for predicting GB energy.

Frank and Bilby developed a theory that predicts the Burgers vector associated with a dislocation at an interface [73, 74]. The approach considers two crystals with some arbitrary orientation and then effects an arbitrary interface character by applying linear transformations F^A, F^B to the lattices. The resultant formula $\mathbf{b} = (F^{A-1} - F^{B-1})\mathbf{t}$ relates the dislocation Burgers vector (\mathbf{b}) for the interface to an in-plane measurement vector (\mathbf{t}). A similar construction is the O-lattice of Bollmann that provides a geometrical sense of the number of coincident points (“O-points”) in two interpenetrating lattices, from

which the registry (and, ostensibly, the dislocation content) may be inferred [75]. By using geometric constructions of the Frank-Bilby/O-lattice types and assuming the existence of ordered networks of interfacial dislocations, it is possible to use anisotropic elasticity theory to compute the resultant energy as well as the full stress field [76]. However, we are not aware of any procedure for predicting the location of energy cusps (for arbitrary configurations) by means of these methods.

A number of approaches have also been developed that capitalize on the lattice periodicity and use it to connect the evaluation of pairwise potentials and the geometric structure of the interface. Sutton [77] proposed an analytic model for grain boundaries' cleavage energy, and Widjaja et. al [78] developed a similar model based on original work by Fletcher [79] that modeled the energy in quasicrystal-crystal epitaxy. However, these approaches are not designed to handle the arbitrary case and cannot determine *a priori* the locations of the cusps.

In an attempt to understand grain boundaries with arbitrary orientation and to model them from a purely physical perspective, many researchers have formulated models for strictly large-angle grain boundaries. The model proposed by Li attempts to model *a posteriori* the excess elastic energy between energy cusps using a disclination-based model [80,81]. Bulatov et al proposed an alternative model based on the concept of so-called "grofs" to build an interpolation that gives an energy function covering a broad range of grain boundary orientations [82]. These models capture the known regions of grain boundary energy well, but their strong dependence on previously available data may compromise their predictive ability.

2.2 Relaxation

The propensity of crystal interfaces to equilibrate by forming piecewise-affine interface segments ("facets") is a phenomenon that has been studied for more than a century. As with most problems in mechanics, the theory of interface morphology begins with the *ansatz* that equilibrium interface shapes are energy minimal, allowing the problem to be posed in a variational framework. In general, crystalline interfaces have a strongly anisotropic energy, resulting in nonconvexity of the integrand. Many non-convex variational problems are eminently treatable in mechanics [18,83–85]; however, minimal surface

problems generally lack coercivity, making a recourse to the familiar calculus of variations approach impossible [86]. Treating problems of this variety (among others) led to the development of geometric measure theory, which provides the necessary tools for minimal surface problems [87].

More than a century ago, Wulff proposed a construction for predicting the equilibrium shape of a crystalline inclusion given that a method exists for computing the interface as a function of normal vector [88]. This formed the basis for the study of crystalline inclusions [89]. The study of crystalline inclusions is well developed; however, it is often the case that an interface is formed in a material that is not globally energy-minimal. For instance, in large crystals, the energy dissipation for reorientation is prohibitively high so that interface energy-minimal shape is inaccessible. Alternatively interfaces between bodies large enough to be treated as semi-infinite crystals face a similar restriction. A major insight into the behavior of such interfaces may be attributed to Herring, who observed that interfaces whose macroscopic orientation does not coincide with one of the equilibrium shape boundaries tend to form a “hill-and-valley” (faceted) structure that is locally energy-minimal [90]. Put mathematically, faceted structures arise as a result of the nonconvexity of the interface energy functional. This interpretation connects the theory of faceted structures to a variety of other nonconvex optimization problems in mechanics [91]. This led to a number of equivalent expressions for energy-minimal facet patterns: Cahn’s use of the vectorized energy formalism to formulate a facet optimization problem [92]; Taylor’s formulation of the problem in terms of convexity [93]; the use of varifolds to represent infinitely finely corrugated surfaces with a macroscopic shape [94–96]; a common tangent construction [97]; and standard convexification with the problem posed in terms of graphs [98]. Independently from the developments in the mathematical community, materials scientists observed that the energy of faceted interfaces can be quantified by rotational interpolation between the facet planes or by constructing a lever-type rule [45, 99].

In the past, relaxation interpretation of faceting has been presented only as a means of explaining the phenomenon, or in a highly reduced form. This is because the development of the relaxation theory in the arbitrary case relies on the existence of a hypothetical interface energy functional γ for all possible interface orientations, from which the relaxed energy γ_C may be computed. However, as discussed

in the previous section, the problem of computing such a γ is still an open question in the modeling community. Because of the lack of a general planar interface model, it has not been possible to use the relaxation model predictively in the general sense. However, with the introduction of a fast and general planar model, we will show that it is possible to use convexification in a predictive way.

Chapter 3

The Covariance Interface Energy Model

In this chapter, a general model for grain boundary energy is formulated by constructing thermalized density measures and defining the covariance as a bilinear functional on them. Results for the covariance model (without any relaxation) are presented to demonstrate the model's range and scope and for validation. The following sections are from the paper "A geometry-based model for the energy of grain boundaries" by Runnels, Beyerlein, Ortiz, currently under review for publication in JMPS [1].

3.1 Theory

3.1.1 Problem definition and notation

The specific aim of the present work is to characterize the interface energy of infinite planar interfaces separating two semi-infinite grains. We consider two general clusters of atoms, labeled b and w ("black" and "white"), interacting through a general interatomic potential. Without approximation, the resulting total energy can be formally written as

$$E_{tot}^{bw}(\{\mathbf{r}^b\}, \{\mathbf{r}^w\}), \quad (3.1)$$

where $E_{tot}^{bw}(\{\mathbf{r}^b\}, \{\mathbf{r}^w\})$ is an energy function and $\{\mathbf{r}^b\}, \{\mathbf{r}^w\}$ are collections of atomic coordinates. Following the definition of Gibbs [100], we define the “excess energy” to be

$$E_{xs} = E_{tot}^{bw}(\{\mathbf{r}^b\}, \{\mathbf{r}^w\}) - E^b - E^w, \quad (3.2)$$

where $E^{b,w}$ are the energies of the black and white crystals as if they were homogeneous [58, 101, 102].

When considering infinite systems, direct evaluation of (3.1) or (3.2) results in infinite energies in general; however the “interfacial energy”, or excess energy density per unit area of the interface, may be expected to be well defined. We define a computable interfacial energy by means of the following limiting process. Consider a sequence of finite systems consisting of the atoms contained in an orthogonal parallelepiped $[-L/2, L/2]^2 \times [-H/2, H/2]$, where the square $[-L/2, L/2]^2$ is contained in the plane of the interface. Let $\{\mathbf{r}_{L,H}^{bw}\}$ be the atomic positions at equilibrium in the finite subsystem thus defined. Then the interfacial energy per unit area follows as the limit

$$\gamma^{bw} = \lim_{L \rightarrow +\infty} \frac{1}{L^2} \left(\lim_{H \rightarrow +\infty} (E_{tot}^{bw}(\{\mathbf{r}_{L,H}^{bw}\}) - N_{L,H}^b E_{coh}^b - N_{L,H}^w E_{coh}^w) \right), \quad (3.3)$$

where $E_{tot}^{bw}(\{\mathbf{r}_{L,H}^{bw}\})$ is the total energy at equilibrium, $E_{coh}^{b,w}$ are the cohesive energies per atom in infinite crystals of type b, w , respectively, and $N_{L,H}^{b,w}$ are the number of atoms of type b and w in the finite subsystem, respectively. Provided that the limits are well-defined, (3.3) supplies a means of computing the interfacial energy per unit area of an infinite planar interface.

We note that the surface energies per unit area of the half-crystals, γ^b and γ^w , follow as special cases as

$$\gamma^b = \lim_{L \rightarrow +\infty} \frac{1}{L^2} \left(\lim_{H \rightarrow +\infty} (E_{tot}^b(\{\mathbf{r}_{L,H}^b\}) - N_{L,H}^b E_{coh}^b) \right) \quad (3.4)$$

and

$$\gamma^w = \lim_{L \rightarrow +\infty} \frac{1}{L^2} \left(\lim_{H \rightarrow +\infty} (E_{tot}^w(\{\mathbf{r}_{L,H}^w\}) - N_{L,H}^w E_{coh}^w) \right), \quad (3.5)$$

where $\{\mathbf{r}_{L,H}^b\}$ and $\{\mathbf{r}_{L,H}^w\}$ are the atomic positions for the free-standing half-crystals b, w at equilibrium, respectively, and $E_{tot}^b(\{\mathbf{r}_{L,H}^b\})$ and $E_{tot}^w(\{\mathbf{r}_{L,H}^w\})$ the corresponding total energies. Subtracting (3.4) and

(3.5) from (3.3) we obtain the alternative representation

$$\gamma^{bw} - \gamma^b - \gamma^w = \lim_{L \rightarrow +\infty} \frac{1}{L^2} \left(\lim_{H \rightarrow +\infty} (E^{bw}(\{\mathbf{r}_{L,H}^{bw}\}) - E^b(\{\mathbf{r}_{L,H}^b\}) - E^w(\{\mathbf{r}_{L,H}^w\})) \right). \quad (3.6)$$

The evaluation of (3.3) and (3.6) give an exact value for interface energy. The MD approach is to minimize γ^{bw} with respect to the atomic positions and then to evaluate it directly. In this work, we seek to model γ^{bw} directly, free from atomic-scale relaxation, with a suitable geometrical quantity.

3.1.2 Density measures of lattices

Consider a Bravais lattice in three dimensions generated by vectors \mathbf{a} , \mathbf{b} , \mathbf{c} . The atomic sites indexed by a 3-tuple $\mathbf{n} \in \mathbb{Z}^3$ with an offset vector \mathbf{t} are enumerated as

$$\mathbf{r}(\mathbf{n}) = \mathbf{t} + n_1\mathbf{a} + n_2\mathbf{b} + n_3\mathbf{c}. \quad (3.7)$$

Let $\varrho : C_0(\mathbb{R}^3) \rightarrow \mathbb{R}$ be a *density measure* defined by the following

$$\int_B d\varrho(\mathbf{x}) = \langle N_B \rangle \quad \forall B \subset \mathbb{R}^3, \quad (3.8)$$

where $\langle N_B \rangle$ is the expectation for the occupancy of B . If the lattice extends to infinity in all directions, is subject to no external forces, and atoms have a fixed (i.e., not fluctuating) position, then the density measure for the lattice is

$$\varrho = \sum_{\mathbf{n} \in \mathbb{Z}^3} \delta_{\mathbf{r}(\mathbf{n})}, \quad (3.9)$$

where $\delta_{\mathbf{x}}$ is the Dirac measure centered at \mathbf{x} . The density measure is *periodic* and therefore is characterized as a *tempered distribution* [103, p.165], and consequently has a Fourier transform [104]. For most crystal structures, there exists an orthogonal parallelepiped periodic cell. This periodic cell exists naturally for lattices with cubic crystal structure such as face-centered (FCC) and body-centered (BCC)

cubic. For lattices with lower symmetry such as hexagonal close-packed (HCP), the rectangular periodic cell is less natural.

3.1.3 Thermalization by maximum entropy

To regularize the model, we account for the effect of temperature on the density measure in a process we refer to as *thermalization*. Let $w_{\mathbf{n}}(\mathbf{x}) = w(\mathbf{x} - \mathbf{r}(\mathbf{n}))$ be a function that measures the energy required to displace atom \mathbf{n} when all of the other atoms in the crystal are held in a fixed position. In a zeroth order approximation, let the lattice density measure be additively decomposed into a sum of probability density measures

$$\varrho = \sum_{\mathbf{n} \in \mathbb{R}^3} \bar{\varrho}_{\mathbf{n}}, \quad (3.10)$$

where $\bar{\varrho}_{\mathbf{n}}$ is the density measure for the location of atom \mathbf{n} . Because it is for a single atom, $\bar{\varrho}_{\mathbf{n}}$ satisfies the normalization constraint, and for the unthermalized case, $\bar{\varrho}_{\mathbf{n}} = \delta_{\mathbf{r}(\mathbf{n})}$. For the regularized case we use a functional representation of ϱ , although this cannot be done in general [105]:

$$d\bar{\varrho}_{\mathbf{n}}(\mathbf{x}) = \rho_{\mathbf{n}}(\mathbf{x})d\mathbf{x}. \quad (3.11)$$

$\rho_{\mathbf{n}}(\mathbf{x})$ is the density *function* for atom \mathbf{n} . $\rho_{\mathbf{n}}$ satisfies the normalization condition $\int \rho_{\mathbf{n}}(\mathbf{x})d\mathbf{x} = 1$, and so it can be considered a probability density function for atom \mathbf{n} . We will use a statistical mechanical argument to compute the form of $\rho_{\mathbf{n}}$ at finite temperature.

The principle of maximum entropy (colloquially “MaxEnt”) provides an efficient and convenient framework for finding the probability density measure given a set of known constraints on a system [106]. Arising from information theory, MaxEnt was applied to thermodynamics by Jaynes [107, 108] and has since been successfully used in many applications [109, 110].

The Gibbs entropy is defined as

$$S[\rho_{\mathbf{n}}] = \int \rho_{\mathbf{n}}(\mathbf{x}) \ln \rho_{\mathbf{n}}(\mathbf{x}) d\mathbf{x}. \quad (3.12)$$

Following the MaxEnt procedure, we seek the maximizer of S subject to a normality constraint,

$$\int \rho_{\mathbf{n}}(\mathbf{x}) d\mathbf{x} = 1 \quad (3.13)$$

and an energy equality

$$\int \rho_{\mathbf{n}}(\mathbf{x}) w_{\mathbf{n}}(\mathbf{x}) d\mathbf{x} = \langle w_{\mathbf{n}} \rangle. \quad (3.14)$$

Enforcing (3.13) and (3.14) by means of Lagrange multipliers, we have

$$\rho_{\mathbf{n}} = \underset{\rho_{\mathbf{n}}}{\operatorname{argsup}} \left[- \int_{\mathbb{R}^n} \rho_{\mathbf{n}}(\mathbf{x}) \ln \rho_{\mathbf{n}}(\mathbf{x}) d\mathbf{x} - \lambda \left(\int_{\mathbb{R}^n} \rho_{\mathbf{n}}(\mathbf{x}) d\mathbf{x} - 1 \right) - \beta \left(\int_{\mathbb{R}^n} w_{\mathbf{n}}(\mathbf{x}) \rho_{\mathbf{n}}(\mathbf{x}) d\mathbf{x} - \langle w_{\mathbf{n}} \rangle \right) \right]. \quad (3.15)$$

Applying stationarity to (3.15) yields the Euler-Lagrange equation

$$\ln \rho_{\mathbf{n}}(\mathbf{x}) + 1 + \lambda + \beta w_{\mathbf{n}}(\mathbf{x}) = 0. \quad (3.16)$$

Using (3.13) to solve for λ we obtain the result

$$\rho_{\mathbf{n}}(\mathbf{x}) = \frac{1}{Q} e^{-\beta w(\mathbf{x}-\mathbf{r}(\mathbf{n}))} \quad Q = \int_{\mathbb{R}^n} e^{-\beta w(\mathbf{x}-\mathbf{r}(\mathbf{n}))} d\mathbf{x}, \quad (3.17)$$

where Q is the single atom partition function, and we identify $\beta = \frac{1}{k_B T}$ as the reciprocal temperature.

The *convolution* of a measure μ with a function f gives

$$(\mu * f)(\mathbf{x}) = \int f(\mathbf{x} - \bar{\mathbf{x}}) d\mu(\bar{\mathbf{x}}) \quad (3.18)$$

[103]. Thus we write (3.17) in convolution form:

$$\bar{\rho}_{\mathbf{n}} = \delta_{\mathbf{r}(\mathbf{n})} * \psi, \quad (3.19)$$

where

$$\psi(\mathbf{x}) = \frac{1}{Q} e^{-\beta w(\mathbf{x})}. \quad (3.20)$$

Now by (3.9) and the linearity of the convolution, we write the lattice density function at finite temperature in terms of the lattice density measure:

$$\rho(\mathbf{x}) = \left(\left(\sum_{\mathbf{n} \in \mathbb{Z}^3} \delta_{\mathbf{r}(\mathbf{n})} \right) \star \psi \right) (\mathbf{x}) = (\varrho \star \psi)(\mathbf{x}) \quad (3.21)$$

3.1.4 Fourier expansions of convolved periodic measures

The general reference for this discussion is Donoghue [103, pp.162-163]. Let μ be a tempered distribution with period 2π . If μ is a measure of finite total mass, that is, $\sum |\mu_k| < \infty$ where

$$\mu_k = \frac{1}{2\pi} \int_0^{2\pi} e^{-ikx} d\mu(x), \quad (3.22)$$

then there is a Fourier series representation for μ

$$d\mu(x) = f(x)dx = \sum_k \mu_k e^{ikx} dx. \quad (3.23)$$

Measures that do not have finite total mass can be regularized by convolution with a smoothing function as follows. Let $\phi : \mathbb{R} \rightarrow \mathbb{R}$ be a mollifying function with Fourier transform $\hat{\phi}$. Then

$$(\mu \star \phi)(x) = \sum_k e^{ikx} c_k \hat{\phi}(k), \quad (3.24)$$

which converges absolutely. It is worth mentioning that for the special cases of $\phi(x) = e^{-\sigma|x|}$ and $\phi(x) = e^{-\sigma|x|^2}$, we see that (3.22) is made *Abel* and *Gauss summable*, respectively, and that we recover the unthermalized limit as $\sigma \rightarrow 0$ [111].

It is easily verified that the lattice density measure ϱ does not have finite mass. Its Fourier transform is the point measure for the dual lattice [112], so the Fourier coefficients clearly do not decay. This

motivates the need for regularization, which is effected by the thermalization of the density functions as discussed in the previous section.

For the applications considered in this work, it suffices to consider lattices that are periodic in an orthogonal parallelepiped $E = [-a_1/2, a_1/2] \times [-a_2/2, a_2/2] \times [-a_3/2, a_3/2]$. With this cuboid periodic cell, (3.24) extends readily to three dimensions:

$$\rho(\mathbf{x}) = (\varrho * \psi)(\mathbf{x}) = \sum_{\mathbf{n} \in \mathbb{R}^3} e^{i\mathbf{k}(\mathbf{n}) \cdot \mathbf{x}} \varrho_{\mathbf{n}} \hat{\psi}(\mathbf{k}(\mathbf{n})), \quad (3.25)$$

where $\mathbf{k}(\mathbf{n}) = [2\pi n_1/a_1, 2\pi n_2/a_2, 2\pi n_3/a_3]$ are the reciprocal lattice vectors and the Fourier coefficients are given by

$$\varrho_{\mathbf{n}} = \frac{1}{|E|} \int_E e^{-i\mathbf{k}(\mathbf{n}) \cdot \mathbf{x}} d\varrho(\mathbf{x}). \quad (3.26)$$

Special care must be taken when evaluating (3.26), because many lattices have sites located on ∂E , the boundary of the periodic cell. Here it is useful to define the three dimensional *set density* [105, p.189]

$$\theta_E(\mathbf{x}) = \lim_{r \rightarrow 0} \frac{\mu(E \cap B^3(\mathbf{x}, r))}{r^3 \mu(B^3(\mathbf{0}, 1))}, \quad (3.27)$$

where μ is a Lebesgue measure and $B^3(\mathbf{x}, a)$ is the three-dimensional ball of radius a centered at \mathbf{x} . For an orthogonal parallelepiped, $\theta_E(\mathbf{x}) = 1$ on the interior, $\frac{1}{2}$ on a face, $\frac{1}{4}$ on an edge, $\frac{1}{8}$ on a corner, and 0 in the exterior. With the set density defined we easily write (3.28) explicitly in terms of the atoms in the unit cell:

$$\varrho_{\mathbf{n}} = \frac{1}{|E|} \sum_{\mathbf{n} \in I_E} \theta_E(\mathbf{r}(\mathbf{n})) e^{-i\mathbf{k}(\mathbf{n}) \cdot \mathbf{r}(\mathbf{n})}, \quad (3.28)$$

where $I_E = \{\mathbf{n} \in \mathbb{Z}^3 : \mathbf{r}(\mathbf{n}) \in E\}$, the index set of the lattice points in the unit cell.

3.1.5 Lattice deformation

Finally, we consider the action of a linear transformation on the lattice in real space. Let $F \in GL(3)$ be a linear map acting on the lattice such that $\mathbf{r}(\mathbf{m}) \mapsto F\mathbf{r}(\mathbf{m})$. We introduce the notation $\rho(\mathbf{x}, F)$ for the density function under the action of a linear transformation, where $\rho(\mathbf{x}) = \rho(\mathbf{x}, I)$ implicitly. Following

the same steps as above, but this time with the measure under the action of a linear transformation, we obtain

$$\rho(\mathbf{x}, F) = \sum_{\mathbf{n} \in \mathbb{Z}^3} \hat{\psi}(F^{-T} \mathbf{k}(\mathbf{n})) \varrho_{\mathbf{n}} e^{i F^{-T} \mathbf{k}(\mathbf{n}) \cdot \mathbf{x}}. \quad (3.29)$$

For the special case $F = R \in SO(3)$ with ψ isotropic we arrive at the simplified expression

$$\rho(\mathbf{x}, R) = \sum_{\mathbf{n} \in \mathbb{Z}^3} \hat{\psi}(\mathbf{k}(\mathbf{n})) \varrho_{\mathbf{n}} e^{i R \mathbf{k}(\mathbf{n}) \cdot \mathbf{x}}. \quad (3.30)$$

3.1.6 Interface covariance

With the lattice density measures and thermalized density functions formalized, we seek to define a geometric quantity that is reflective of the interface energy. We observe a strong correlation between low interface energy and the registry of the two lattices at the interface; therefore we look for a quantity that measures the degree of matched coincidence on the subspace of the interface plane. Let us consider an interface between two thermalized lattices, “black” and “white”, with lattice density measures ϱ^b, ϱ^w , thermalization functions ψ^b, ψ^w , thermalized density functions ρ^b, ρ^w , under linear transformations F^b, F^w . Both crystals are periodic, but not necessarily with respect to the same unit cell. Without a loss of generality, we let the $x_1 - x_2$ plane correspond to the shared interface between the black and white crystals. We define $P : \mathbb{R}^3 \rightarrow \mathbb{R}^2$ as the submersion operator

$$P = \begin{bmatrix} 1 & 0 & 0 \\ 0 & 1 & 0 \end{bmatrix}, \quad (3.31)$$

where $P^T : \mathbb{R}^2 \rightarrow \mathbb{R}^3$ is the embedding of the $x_1 - x_2$ plane into \mathbb{R}^3 . Thus $\rho^{b,w}(P^T \mathbf{y})$, $\mathbf{y} \in \mathbb{R}^2$ is the density function evaluated on the interface. With these established, we propose the following geometric quantity that we refer to here and subsequently as covariance.

Definition 3.1 (Covariance). *The covariance of two lattices with thermalized density functions ρ^b, ρ^w*

under the linear transformations $F^b, F^w \in GL(3)$ is defined as the bilinear functional

$$c[\rho^b(\cdot, F^b), \rho^w(\cdot, F^w)] = \frac{1}{\mu(\mathbf{1})} \int \rho^b(P^T \mathbf{y}, F^b) \rho^w(P^T \mathbf{y}, F^w) d\mu(\mathbf{y}), \quad (3.32)$$

with μ a measure on $L^2(\mathbb{R}^2)$ as

$$\mu(f) = \int_{\mathbb{R}^2} f(\mathbf{y}) \phi(\mathbf{y}) d\mathbf{y} \quad (3.33)$$

and $\phi : \mathbb{R}^2 \rightarrow \mathbb{R}$ an integrable window function

Some immediate simplifications of (3.32) are apparent. From [104, Example 7.16] we have

$$\mu(\mathbf{1}) = \int_{\mathbb{R}^2} \phi(\mathbf{y}) d\mathbf{y} = \hat{\phi}(\mathbf{0}). \quad (3.34)$$

Because we have explicit expressions for ρ^b, ρ^w , we can evaluate (3.32) directly.

$$\begin{aligned} c[\rho^b(\cdot, F^b), \rho^w(\cdot, F^w)] &= \\ &= \frac{1}{\hat{\phi}(\mathbf{0})} \sum_{\mathbf{m}, \mathbf{n} \in \mathbb{Z}^3} \varrho_{\mathbf{m}}^b \varrho_{\mathbf{n}}^{w*} \hat{\psi}(F^{b-T} \mathbf{k}^b(\mathbf{m})) \hat{\psi}^*(F^{w-T} \mathbf{k}^w(\mathbf{n})) \int e^{i(PF^{b-T} \mathbf{k}^b(\mathbf{m}) - PF^{w-T} \mathbf{k}^w(\mathbf{n})) \cdot \mathbf{y}} \phi(\mathbf{y}) d\mathbf{y} \\ &= \frac{1}{\hat{\phi}(\mathbf{0})} \sum_{\mathbf{m}, \mathbf{n} \in \mathbb{Z}^3} \varrho_{\mathbf{m}}^b \varrho_{\mathbf{n}}^{w*} \hat{\psi}(F^{b-T} \mathbf{k}^b(\mathbf{m})) \hat{\psi}^*(F^{w-T} \mathbf{k}^w(\mathbf{n})) \hat{\phi}(PF^{b-T} \mathbf{k}_m^b - PF^{w-T} \mathbf{k}_n^w). \end{aligned} \quad (3.35)$$

For the special case of $F = R \in SO(3)$ with ψ isotropic, (3.35) reduces to

$$c[\rho^b(\cdot, R^b), \rho^w(\cdot, R^w)] = \frac{1}{\hat{\phi}(\mathbf{0})} \sum_{\mathbf{m}, \mathbf{n} \in \mathbb{Z}^3} \varrho_{\mathbf{m}}^b \varrho_{\mathbf{n}}^{w*} \hat{\psi}(\mathbf{k}^b(\mathbf{m})) \hat{\psi}^*(\mathbf{k}^w(\mathbf{n})) \hat{\phi}(PR^b \mathbf{k}_m^b - PR^b \mathbf{k}_n^w). \quad (3.36)$$

An examination of (3.35) yields insight into the behavior of c . The double sum ensures that all possible matched periodicity between the two lattices is incorporated. The Fourier coefficients $\varrho_{\mathbf{m}, \mathbf{n}}^{b, w}$ contain the information about the lattice structure. The thermalization functions $\psi^{b, w}$ monotonically decrease to zero with increasing \mathbf{m}, \mathbf{n} , and thus they cause high order modes to be damped and to give convergence of the sum, as expected. The Fourier transformed window function $\hat{\phi}$ becomes a saturated measure of the coincidence between transformed reciprocal lattice vectors, returning a maximal value

when coincidence is attained.

Another useful fact about (3.35) is that it is given entirely in terms of $\hat{\phi}$ and $\hat{\psi}$, that is, expressions for ϕ and ψ are not needed. This is beneficial from a modeling perspective, as it eliminates the need to compute Fourier transforms, which is frequently nontrivial in two or more dimensions. Here we emphasize that, for the general formulation, the only restrictions on $\hat{\phi}$ and $\hat{\psi}$ are their square integrability. We restrict to specific forms only in the results section where we validate the model.

3.1.7 Bounds on covariance

We immediately note that (3.35) is *maximized* by coincidence. This suggests an inverse relationship with energy. Thus it is useful at this point to determine scaling relations that map the covariance to a reasonable range for energy.

By (3.8), we have that

$$\int_B \rho(\mathbf{x}) dx = \langle N_B \rangle \geq 0 \quad \forall B \subset \mathbb{R}^n \implies \rho(\mathbf{x}) \geq 0, \quad (3.37)$$

whence we establish a lower bound for the covariance functional

$$c[\rho^b, \rho^w] \geq 0 \quad \forall \rho^b, \rho^w. \quad (3.38)$$

We observe that the covariance functional defines an inner product over $L_2(\mathbb{R}^2)$, which in turn induces a norm over the space. This prompts an application of the Cauchy-Schwarz inequality, giving

$$\begin{aligned} c[\rho^b(\mathbf{x}, F^b), \rho^w(\mathbf{x}, F^w)]^2 &\leq c[\rho^b(\mathbf{x}, F^b), \rho^b(\mathbf{x}, F^b)] c[\rho^w(\mathbf{x}, F^w), \rho^w(\mathbf{x}, F^w)] \\ &\leq \sup_{\bar{F}^b, \bar{F}^w \in GL(3)} c[\rho^b(\mathbf{x}, \bar{F}^b), \rho^b(\mathbf{x}, \bar{F}^b)] c[\rho^w(\mathbf{x}, \bar{F}^w), \rho^w(\mathbf{x}, \bar{F}^w)] \\ &= \sup_{\bar{F}^b \in GL(3)} c[\rho^b(\mathbf{x}, \bar{F}^b), \rho^b(\mathbf{x}, \bar{F}^b)] \sup_{\bar{F}^w \in GL(3)} c[\rho^w(\mathbf{x}, \bar{F}^w), \rho^w(\mathbf{x}, \bar{F}^w)]. \end{aligned} \quad (3.39)$$

Here we restrict F^a, F^b to $SO(3)$, considering rigid lattice rotations only. Inequality (3.39) introduces a

notion of a ground-state covariance:

$$c_{gs}[\rho^b, \rho^w] = \left(\sup_{\bar{F}^b \in SO(3)} c[\rho^b(\cdot, \bar{F}^b), \rho^b(\cdot, \bar{F}^b)] \sup_{\bar{F}^w \in SO(3)} c[\rho^w(\cdot, \bar{F}^w), \rho^w(\cdot, \bar{F}^w)] \right)^{1/2} \quad (3.40)$$

Let the normalized covariance be defined as follows

$$C[\rho^b(\cdot, R^b), \rho^w(\cdot, R^w)] = 1 - \frac{c[\rho^b(\cdot, R^b), \rho^w(\cdot, R^w)]}{c_{gs}[\rho^b, \rho^w]}, \quad (3.41)$$

whence it is easily verified that

$$0 \leq C[\rho^b(\cdot, R^b), \rho^w(\cdot, R^w)] \leq 1. \quad (3.42)$$

3.1.8 Microscopic degrees of freedom

Up to this point, only the effect of macroscopic degrees of freedom—that is, the relative rotations and interface orientation—have been considered on the grain boundary energy. Now we investigate the effect of the microscopic degrees of freedom. In general, the microscopic degrees of freedom are the relative rigid-body displacement between the two crystals

$$\mathbf{t} = \mathbf{t}^b - \mathbf{t}^w, \quad (3.43)$$

where $\mathbf{t}^b, \mathbf{t}^w$ are the translation vectors referred to in (3.7). In atomistic simulations, the microscopic degrees of freedom are determined by relaxation. In an experimental context, it is generally not possible to prescribe a relative displacement in a grain boundary. It is therefore of no utility to incorporate the offset vector as a free variable into the covariance model. However, because it may significantly affect the result, we cannot neglect it. Therefore, we seek a method for the selection of an optimal offset vector.

We will show that the covariance is inversely correlated to grain boundary energy. Thus a natural choice for an offset vector is one that minimizes energy and, consequently, maximizes the covariance.

To find the optimal offset we first modify the expression for a density function (3.30) by giving the lattice an offset \mathbf{t} :

$$\rho(\mathbf{x}, F, \mathbf{t}) = \sum_{\mathbf{n} \in \mathbb{Z}^3} \hat{\psi}(F^{-T} \mathbf{k}(\mathbf{n})) \varrho_{\mathbf{n}} e^{i F^{-T} \mathbf{k}(\mathbf{n}) \cdot (\mathbf{x} - \mathbf{t})} \quad (3.44)$$

$$= \sum_{\mathbf{n} \in \mathbb{Z}^3} \hat{\psi}(F^{-T} \mathbf{k}(\mathbf{n})) \varrho_{\mathbf{n}} e^{-i F^{-T} \mathbf{k}(\mathbf{n}) \cdot \mathbf{t}} e^{i R \mathbf{k}(\mathbf{n}) \cdot \mathbf{x}}. \quad (3.45)$$

Let $\mathbf{t}^b, \mathbf{t}^w$ be the offset vectors for the two lattices so that the total offset is $\mathbf{t}^b - \mathbf{t}^w$. Substituting into (3.35) we have

$$\begin{aligned} c[\rho^b(\cdot, F^b, \mathbf{t}^b), \rho^w(\cdot, F^w, \mathbf{t}^w)] &= \\ &= \frac{1}{\hat{\phi}(\mathbf{0})} \sum_{\mathbf{m}, \mathbf{n} \in \mathbb{Z}^3} \varrho_{\mathbf{m}}^b \varrho_{\mathbf{n}}^{w*} \hat{\psi}(F^{b-T} \mathbf{k}^b(\mathbf{m})) \hat{\psi}^*(F^{w-T} \mathbf{k}^w(\mathbf{n})) e^{-i (F^{b-T} \mathbf{k}(\mathbf{m}) \cdot \mathbf{t}^b - F^{w-T} \mathbf{k}(\mathbf{n}) \cdot \mathbf{t}^w)} \times \\ &\quad \hat{\phi}(PF^{b-T} \mathbf{k}_m^b - PF^{w-T} \mathbf{k}_n^w). \end{aligned} \quad (3.46)$$

Proposition 3.1 (Minimal offset vector). *Let ϱ^b, ϱ^w be density measures. Let the thermalization function ψ and the window function ϕ be defined such that $\hat{\psi}$ and $\hat{\phi}$ are nonnegative. Let $F^b, F^w \in GL(3)$. If $\varrho_m^b, \varrho_n^w \in \mathbb{R}^+$ then*

$$\operatorname{argsup}_{\mathbf{t}^b, \mathbf{t}^w} c[\rho^b(\cdot, F^b, \mathbf{t}^b), \rho^w(\cdot, F^w, \mathbf{t}^w)] = (\mathbf{0}, \mathbf{0}). \quad (3.47)$$

Proof. Using the fact that all terms are nonnegative except the exponential term, we find

$$\begin{aligned} c[\rho^b(\cdot, F^b, \mathbf{t}^b), \rho^w(\cdot, F^w, \mathbf{t}^w)] &\leq |c[\rho^b(\cdot, F^b, \mathbf{t}^b), \rho^w(\cdot, F^w, \mathbf{t}^w)]| \\ &= \left| \frac{1}{\hat{\phi}(\mathbf{0})} \sum_{\mathbf{m}, \mathbf{n} \in \mathbb{Z}^3} \varrho_{\mathbf{m}}^b \varrho_{\mathbf{n}}^{w*} \hat{\psi}(F^{b-T} \mathbf{k}^b(\mathbf{m})) \hat{\psi}^*(F^{w-T} \mathbf{k}^w(\mathbf{n})) e^{-i (F^{b-T} \mathbf{k}(\mathbf{m}) \cdot \mathbf{t}^b - F^{w-T} \mathbf{k}(\mathbf{n}) \cdot \mathbf{t}^w)} \times \right. \\ &\quad \left. \hat{\phi}(PF^{b-T} \mathbf{k}_m^b - PF^{w-T} \mathbf{k}_n^w) \right| \\ &= \frac{1}{\hat{\phi}(\mathbf{0})} \sum_{\mathbf{m}, \mathbf{n} \in \mathbb{Z}^3} \varrho_{\mathbf{m}}^b \varrho_{\mathbf{n}}^{w*} \hat{\psi}(F^{b-T} \mathbf{k}^b(\mathbf{m})) \hat{\psi}^*(F^{w-T} \mathbf{k}^w(\mathbf{n})) \underbrace{|e^{-i (F^{b-T} \mathbf{k}(\mathbf{m}) \cdot \mathbf{t}^b - F^{w-T} \mathbf{k}(\mathbf{n}) \cdot \mathbf{t}^w)}|}_{\leq 1} \times \end{aligned}$$

$$\begin{aligned}
& \hat{\phi}(PF^{b-T}\mathbf{k}_m^b - PF^{w-T}\mathbf{k}_n^w) \\
& \leq \frac{1}{\hat{\phi}(\mathbf{0})} \sum_{\mathbf{m}, \mathbf{n} \in \mathbb{Z}^3} \varrho_{\mathbf{m}}^b \varrho_{\mathbf{n}}^{w*} \hat{\psi}(F^{b-T}\mathbf{k}^b(\mathbf{m})) \hat{\psi}^*(F^{w-T}\mathbf{k}^w(\mathbf{n})) \hat{\phi}(PF^{b-T}\mathbf{k}_m^b - PF^{w-T}\mathbf{k}_n^w) \\
& = c[\rho^b(\cdot, F^b, \mathbf{0}), \rho^w(\cdot, F^w, \mathbf{0})] \tag{3.48}
\end{aligned}$$

whence we conclude that $\mathbf{t}^b = \mathbf{t}^w = \mathbf{0}$ maximize the covariance.

Proposition 3.1 provides sufficient conditions to guarantee that no offset vector need be considered in covariance calculations. The conditions of nonnegativity for ψ and ϕ are satisfied naturally, but the constraints on $\varrho_{\mathbf{m}}^b, \varrho_{\mathbf{n}}^w$ are more restrictive. The property $\varrho_{\mathbf{n}} \in \mathbb{R}$ is satisfied automatically if the periodic cell E is chosen so that the lattice is symmetric, but the constraint of nonnegativity must be additionally verified. For the lattice structures considered in this work (FCC and BCC), the properties are verified easily. However we note that the rectangular periodic cell for other structures such as HCP are asymmetric. Consequently, the role of the offset vector will need to be considered for those cases.

3.1.9 Covariance as a measure of grain boundary energy

With the covariance defined as a geometric quantity, we hypothesize that the covariance controls the interface energy. Employing a simple linear scaling relationship, we have as the formulation of the general covariance model

$$\gamma^{bw}(R^b, R^w) = E_0 C[\rho^b(\cdot, R^b), \rho^w(\cdot, R^w)], \tag{3.49}$$

where E_0 is a material-dependent parameter.

The atomic embedding energy $w(\mathbf{x})$ (and hence $\psi(\mathbf{k})$) can be determined experimentally or theoretically, but for most purposes we find that a simple quadratic potential effects a sufficiently close result and, additionally, admits a ready formulation of its Fourier transform. The window function $\psi(\mathbf{x})$ appears to determine the near-cusp behavior of the energy, and we may expect that there is some connection between the choice of window function and the elastic constants of the crystals. However this observation is strictly, for the time being, empirical. We leave the selection of $\psi(\mathbf{x})$ (or, rather

$\hat{\psi}(\mathbf{k})$ —only the reciprocal function is needed for evaluation) open as a way to introduce near-cusp models into the general framework.

While the relationship between covariance and interface energy is as yet an empirical connection, the covariance formulation provides a number of useful insights into the relationship between interface energy and state variables. It is observed that the main motivator of the energy is the coherence of the interface, in the argument of $\hat{\phi}$. If $\hat{\phi}$ is maximized by $\mathbf{0}$, then the covariance increases when there is registry between the dual lattice vectors $\mathbf{k}(\mathbf{n})$ under their respective linear transformations.

The effect of the thermalization function ψ is to dampen higher order terms in the sum. For the case of $0K$, $\psi \rightarrow \delta$, and consequently $\hat{\psi} \rightarrow 1$. This destroys the convergence of the sum, effectively allowing an infinite number of terms to contribute equally, as expected. Alternatively, at higher temperature, $\sigma(\psi)$ (the standard deviation of ψ) decreases, damping higher order terms. From this it is clear that the fine structure of the interface energy function is visible at low temperatures, but is damped out with thermal fluctuations.

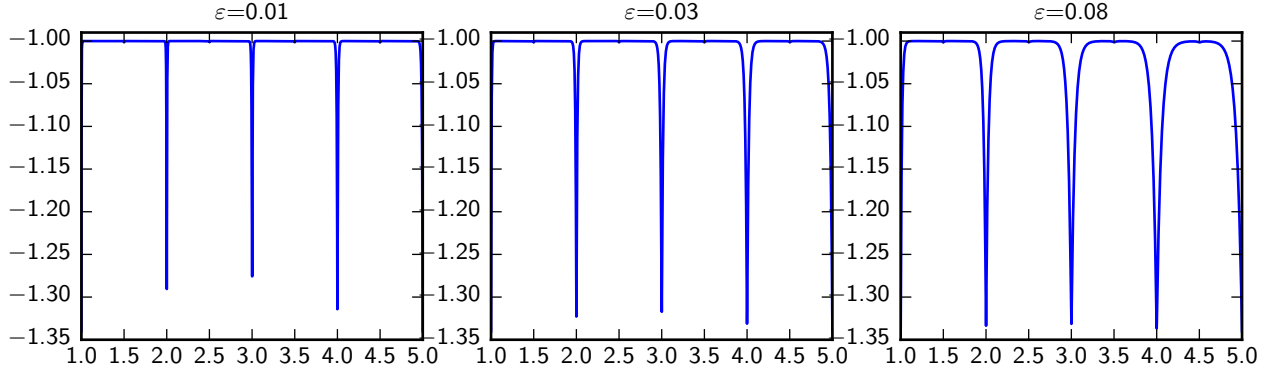
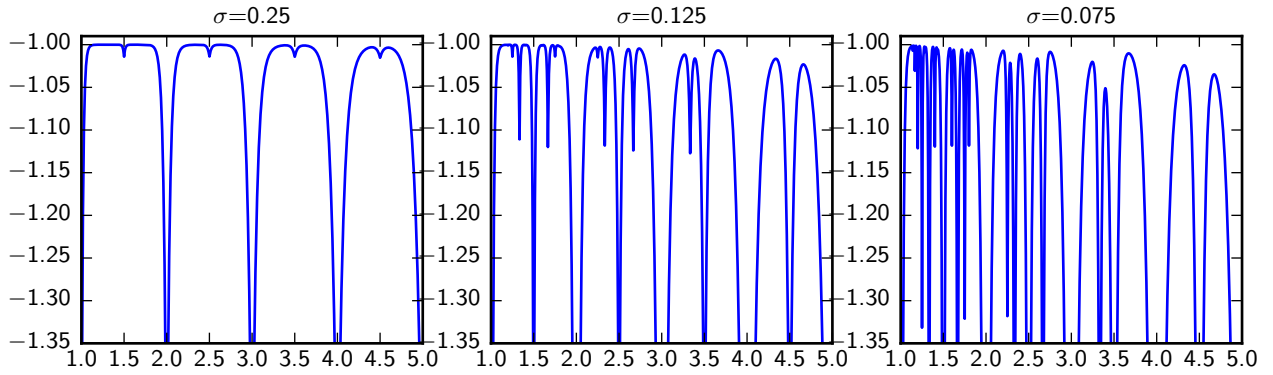
We conclude this section with a simple example that demonstrates the behavior of the model for the simplest possible nontrivial system. In the subsequent sections we validate the use of the model by comparison to molecular dynamics data for grain boundary energy.

Example 3.1 (1D chains). Let ρ^b, ρ^w be 1D lattices with lattice constants equal to a^b, a^w , respectively. Then for $0K$

$$\varrho^{b,w}(x) = \sum_{n \in \mathbb{Z}} \delta_{na^{b,w}}. \quad (3.50)$$

For both lattices, let

$$\psi_\sigma(x) = \frac{1}{\sigma\sqrt{\pi}} e^{-x^2/\sigma^2} \quad \implies \quad \hat{\psi}_\sigma(k) = e^{-\sigma^2 k^2/4}, \quad (3.51)$$

(a) (negative) covariance as a function of a with σ fixed at $\sigma = 0.3$.(b) (negative) covariance as a function of a with ε fixed at $\varepsilon = 0.1$.

where $\sigma = \sqrt{\frac{2k_B T}{E}}$, the thermalization constant. Then the thermalized lattice density function is

$$\rho^{b,w}(x) = \sum_{n \in \mathbb{Z}} \hat{\psi}(2\pi n/a^{b,w}) e^{i2\pi n/a^{b,w}}. \quad (3.52)$$

Let

$$\hat{\phi}_\varepsilon(k) = e^{-|k|/\varepsilon}. \quad (3.53)$$

In real space the integral formulation of the covariance is

$$c[\rho^a, \rho^b] = \int_{-\infty}^{\infty} \rho^a(x) \rho^b(x) dx \quad (3.54)$$

$$= \sum_{m,n \in \mathbb{Z}} \hat{\psi}(2\pi m/a^b) \hat{\psi}(2\pi n/a^w) \int_{-\infty}^{\infty} e^{i(2\pi n/a^b - 2\pi m/a^w)x} \phi(x) dx \quad (3.55)$$

$$= \sum_{m,n \in \mathbb{Z}} \hat{\psi}(2\pi m/a^b) \hat{\psi}(2\pi n/a^w) \hat{\phi}(2\pi n/a^w - 2\pi m/a^b) dx. \quad (3.56)$$

Letting $a^b = 1$ and $a^w \rightarrow a$, we plot the covariance as a function of a for various values of σ (Figure 3.1b) and ε (Figure 3.1a).

These figures show the effect of varying ε and σ . As ε decreases the cusps become less smooth. In the limit as $\varepsilon \rightarrow 0$, the cusps become perfectly sharp, as expected.

On the other hand, we see that the value of σ does not affect the slope of the cusps directly. The value of σ determines the degree of “fine structure” in the energy functional; $\sigma \rightarrow 0$ causes the cusp structure to become infinitely dense, as expected.

3.2 Results for homophase boundaries

The space of interface orientations is exceedingly large. Consequently we restrict the scope of the validation tests to a subset of well-understood interface classes, with the expectation that consistent behavior for these interface classes is an indicator of the predictive nature of the model. The choice of these interface classes is entirely driven by the availability of verification data. The data for interface energy, in lieu of direct experimental measurement, is taken from MD simulations.

In this section we consider homophase interfaces or grain boundaries, that is, interfaces for which a rotational transformation exists that transforms one crystal lattice to the other. We consider the following three types of interfaces: **symmetric tilt grain boundaries** (STGB), **symmetric twist grain boundaries** (STwGB), and **asymmetric twist grain boundaries** (ATwGB). Additionally, we consider materials whose lattice structure falls into one of three categories: **face-centered cubic** (FCC), **body-centered cubic** (BCC), and **hexagonal close-packed** (HCP). Two or more materials are considered for each choice of crystal structure and boundary class, with the choice of materials driven by the availability of MD data.

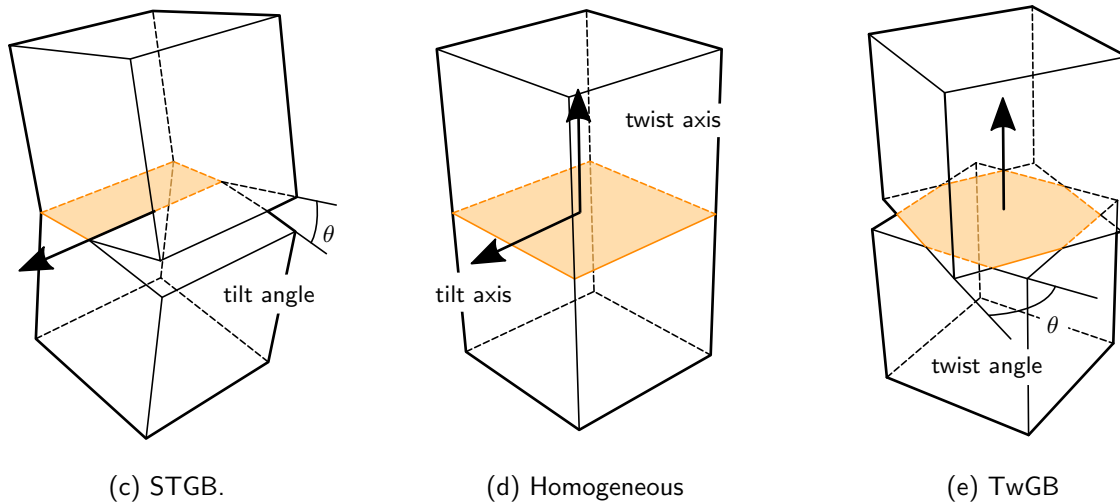


Figure 3.1: We begin with a uniform crystal with no boundary (center). A symmetric tilt grain boundary is formed by symmetric rotation about an in-plane tilt axis (left). A symmetric twist grain boundary results from asymmetric rotation about the normal twist axis (right).

3.2.1 Grain boundary geometry

Three types of grain boundary geometries are considered in this section.

Symmetric tilt grain boundaries (Figure 3.1c) are obtained by rotating two halves of a uniform crystal symmetrically with respect to a prescribed interface. Thus all STGBs are defined by i) the crystallographic direction (in Miller indices) corresponding to the constant *tilt axis* that remains constant, ii) the total *tilt angle* between the two crystals about the tilt axis, and iii) the direction corresponding to the *initial normal axis* to the homogeneous interface. Because STGBs are by definition symmetric about the constant interface plane, the tilt axes must lie within a symmetry plane of the crystal [58]; as such the class of STGBs is limited to a selection of tilt axes. For cubic materials the STGB tilt axes are $\langle 100 \rangle$, $\langle 110 \rangle$, $\langle 111 \rangle$, and $\langle 112 \rangle$, and we have found a wide selection of MD data for these STGBs [41–43, 49–51].

Symmetric twist grain boundaries (Figure 3.1e) are obtained by an antisymmetric rotation of upper and lower halves of the crystal about a common axis (the “twist axis”) that is normal to the initial interface plane. The twist axis and twist angle are sufficient to characterize any STwGB grain boundary. As with STGBs, the class of STwGBs are restricted to those associated with twist axes for which the

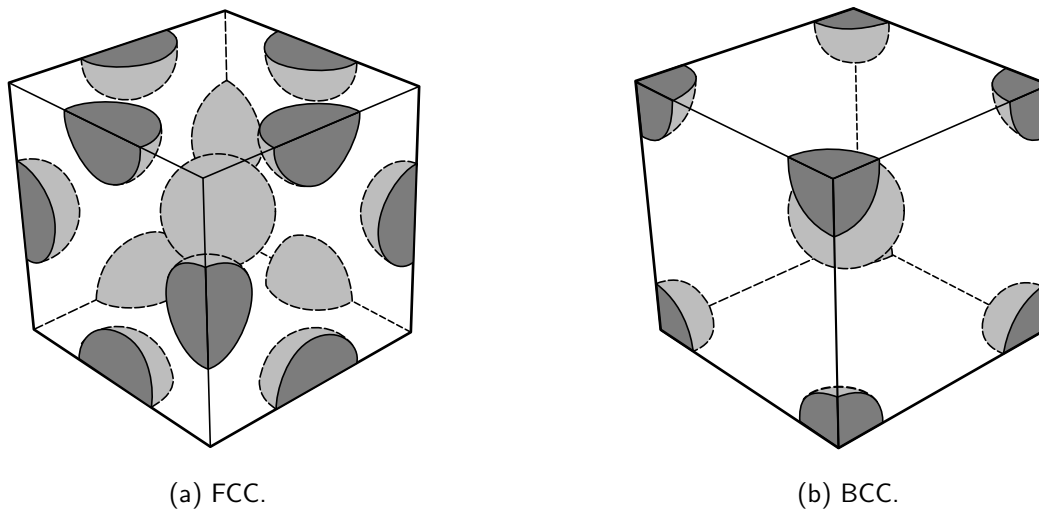


Figure 3.2: Optimal geometry of unit cells for FCC and BCC crystal structures.

corresponding normal is a symmetry plane of the material. Asymmetric twist grain boundaries are defined similarly to STwGBs, but without the restriction of a common twist axis between the materials (thereby eliminating any restrictions on the symmetry of the interface). Classes of ATwGBs are specified using the two crystallographic directions corresponding to the normal vectors of the top and bottom crystals.

3.2.2 Crystal structure and material parameters

The atomic density functions ρ for the crystals are computed in Fourier series form. The Fourier coefficients ϱ_n for a lattice are computed by integrating over the unit cell $[-a/2, a/2]^3$. Cubic lattices (FCC, BCC) have a natural rectangular unit cell that is tabulated easily. The rectangular unit cells for BCC and FCC crystal structures are illustrated in Figure 3.2, and their locations are given in Table 3.1. The unit cell for the BCC case is familiar, but we note that the choice of FCC unit cell differs from the conventional unit cell for this structure. The reason for this choice is to satisfy the positivity conditions in Proposition 3.1; proof is given in Appendix A for both structures.

Assuming a quadratic potential for the atomic displacement energy: $w(\mathbf{x}) = \frac{1}{2}E\|\mathbf{x}\|^2$, the corresponding normalized thermalization function is a Gaussian function

Table 3.1: Locations of atoms in the Fourier periodic unit cell for BCC, FCC, and HCP lattices.

Crystal structure	Unit cell E	Atomic Locations $\{\mathbf{r}_i\}$	Density $\theta(\mathbf{r}_i)$
BCC	$[-\frac{a}{2}, \frac{a}{2}]^3$	$(0,0,0)$ $(\pm\frac{a}{2}, \pm\frac{a}{2}, \pm\frac{a}{2})$	1 1/8
FCC	$[-\frac{a}{2}, \frac{a}{2}]^3$	$(0,0,0)$ $(0, \pm\frac{a}{2}, \pm\frac{a}{2}), (\pm\frac{a}{2}, 0, \pm\frac{a}{2}), (\pm\frac{a}{2}, \pm\frac{a}{2}, 0)$	1 1/4

$$\psi(\mathbf{x}) = \frac{1}{\sigma^3 \pi^{3/2}} e^{-\|\mathbf{x}\|^2/\sigma^2}, \quad (3.57)$$

where the quantity $\sigma^2 = 2kT/E$ is the dimensionless temperature. For the window function we choose a Cauchy distribution function

$$\hat{\phi}(\mathbf{k}) = e^{-\|\mathbf{k}\|/\varepsilon}, \quad (3.58)$$

which closely models the behavior of the interface energy function near energy cusps. With this choice of thermalization and window functions the energy model is dependent on three material parameters: σ , ε , and E_0 . We have determined these values by finding the optimal fit based on a wide range of MD data (Table 3.2).

The MD data chosen for comparison in this work is taken from a series of papers by Wolf [41–51], which provide comprehensive data from a wide range of interface configurations using a consistent methodology. MD data from other works was considered (including some for which an even closer fit to the covariance model was obtained, c.f. [113]); however, we found that results from different authors required different selections of E_0 . Therefore we choose a set of self-consistent MD results for validation.

Table 3.2: Material parameter values used for materials in all GB tests

	Cu (FCC)	Au (FCC)	Mo (BCC)	Fe (BCC)
$E_0(J/m^2)$	1.45	0.95	2.525	1.950
σ/α	0.175	0.175	0.19	0.19
ε	0.5	0.5	0.25	0.25

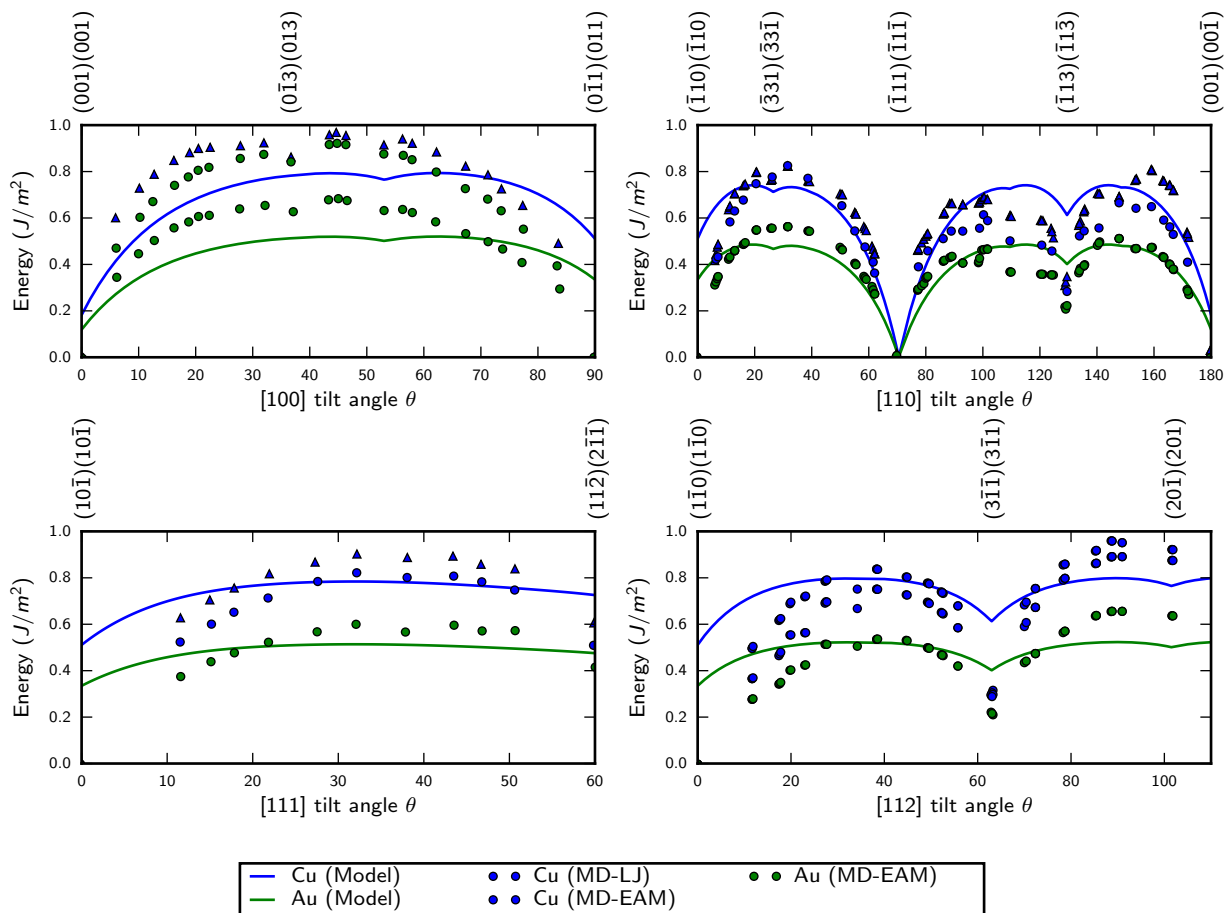


Figure 3.3: FCC STGB results of the covariance model for Copper and Gold, compared with molecular dynamics results using the Embedded Atom Method (EAM) and Lennard-Jones (LJ) potentials. MD results from [41]. Annotations on the top indicate the boundary plane for the top crystal at cusp locations.

3.2.3 FCC symmetric tilt grain boundaries

The first set considered are the FCC symmetric tilt grain boundaries. The results of the comparison for the [100], [110], [111], and [112] boundaries are presented in Figure 3.3. We compare and fit the model results to MD results from [41] for gold, using an embedded atom method (EAM) potential, and copper, using both EAM and Lennard-Jones (LJ) potentials. We computed the grain boundary energy using the covariance model (the solid line), and observed a close matching of the model to the MD results.

For the [100] tilt boundaries, the cusp corresponding to the {110} boundary is observed at $\theta = 90^\circ$. For the [110] tilt boundaries, we observe the cusps corresponding to the {111} and {113} boundaries at $\theta = 70.6^\circ$ and $\theta = 129.4^\circ$, respectively. For the [111] tilt boundaries, other than the cusp corresponding to the homogeneous case at $\theta = 0^\circ$, we do not observe any significant energy cusps. For the [112] tilt boundaries, we observe a deep cusp corresponding to the {113} boundary. The location of all of the deep energy cusps for $\theta > 0$ predicted by the MD data are matched exactly (to an arbitrary degree of precision) by the model.

We observe a discrepancy between the model and the MD data at the {100} homogeneous case ($\langle 100 \rangle$ at $\theta = 0^\circ$) and the {110} homogeneous case ($\langle 110 \rangle, \langle 111 \rangle, \langle 112 \rangle$ STGB at $\theta = 0^\circ$). Although the location of the cusps corresponding to the homogeneous case is correct, we observe that the model overpredicts the energy. To address this issue requires additional considerations of relaxation, which will be discussed in the next chapter.

3.2.4 BCC symmetric tilt grain boundaries

The next set of boundaries considered are the symmetric tilt grain boundaries for BCC crystals, with the same configurations and θ ranges as for FCC STGBs. We compare the results of the model with MD results from [49] for α -Iron (Ferrite) using a Johnson potential, and Molybdenum using a Finnis-Sinclair type potential. The model results are plotted in Figure 3.4. We observe strong agreement between the predictions of the model and with the MD results.

For the [100] tilt we observe strong energy cusps at $\theta = 0^\circ, 90^\circ$, corresponding to the {100} and {110} STGBs. A weak cusp is also present at $\theta = 37^\circ$ corresponding to the {310} STGB. For [110] tilt, we observe strong energy cusps at $\theta = 0, 109^\circ, 180^\circ$, corresponding to the {110}, {112}, {100} boundaries. We note that the cusp at $\theta = 51^\circ$ corresponding to the {332} STGB is only barely noticeable in the model, whereas it is a significant cusp in the MD data. On the other hand, the model predicts a cusp at $\theta = 70^\circ$ corresponding to the {111} STGB that is not present in the MD data. We refer the reader to alternative MD simulations (e.g., [113]) of the same boundaries that also do not predict the {332} cusp. For the [111] tilt boundaries we observe deep cusps at $\theta = 0^\circ$ and $\theta = 90^\circ$,

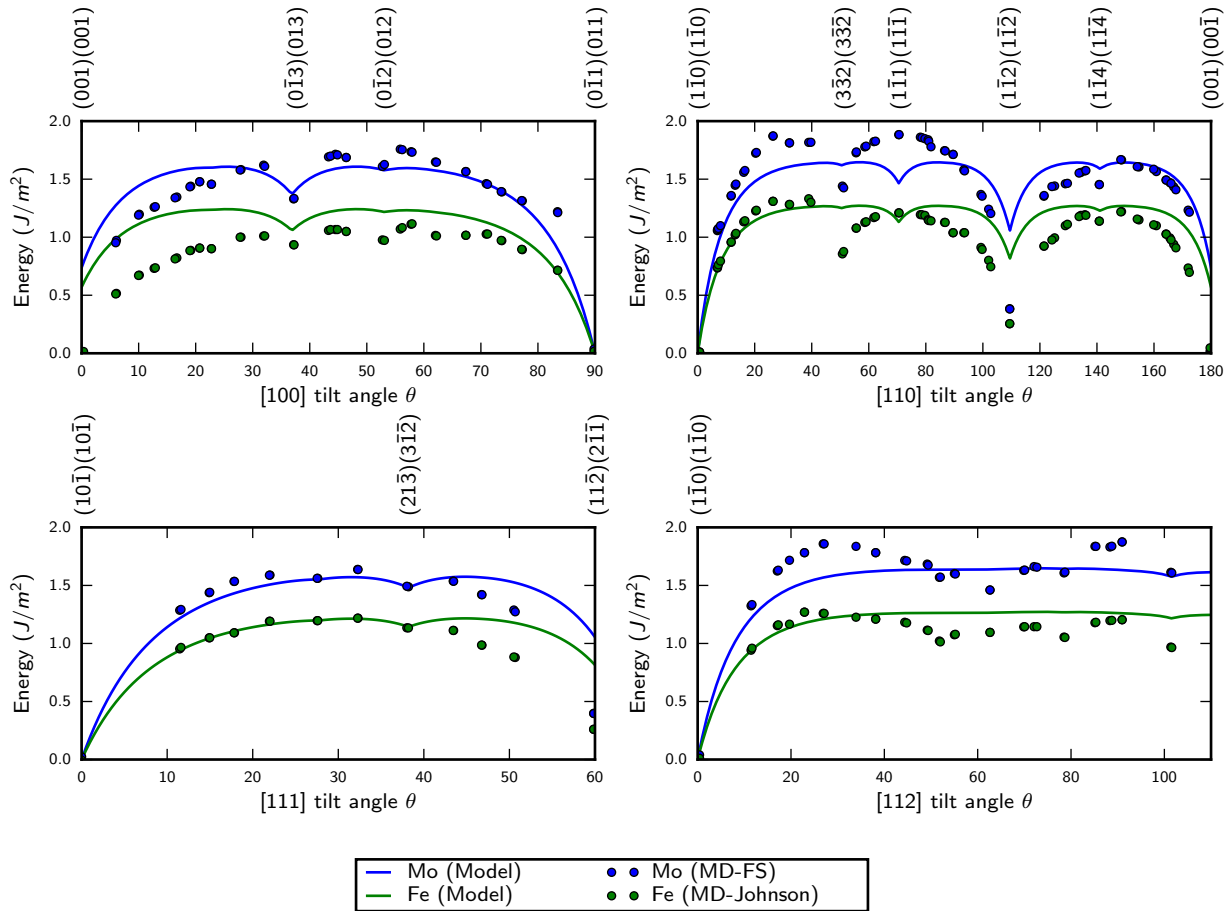


Figure 3.4: BCC STGB results of the covariance model for Molybdenum and α -Iron, compared with MD results using FS (for Mo) and Johnson (for Fe) potentials. MD results from [49]. Annotations on the top indicate the boundary plane for the top crystal at cusp locations.

corresponding to the $\{100\}$ and $\{110\}$ STGBs. A minor cusp is observed at $\theta = 38^\circ$ corresponding to the $\{231\}$ STGBs.

3.2.5 FCC twist grain boundaries

The next set of boundaries considered are the FCC twist grain boundaries. There are two types of these boundaries: asymmetric twist (ATwGB) and symmetric twist (STwGB). The STwGBs are created by beginning with a homogeneous crystal, defining a twist axis, and rotating the top and bottom crystals symmetrically about it. ATwGBs are a more general class of boundaries, and are defined by the two

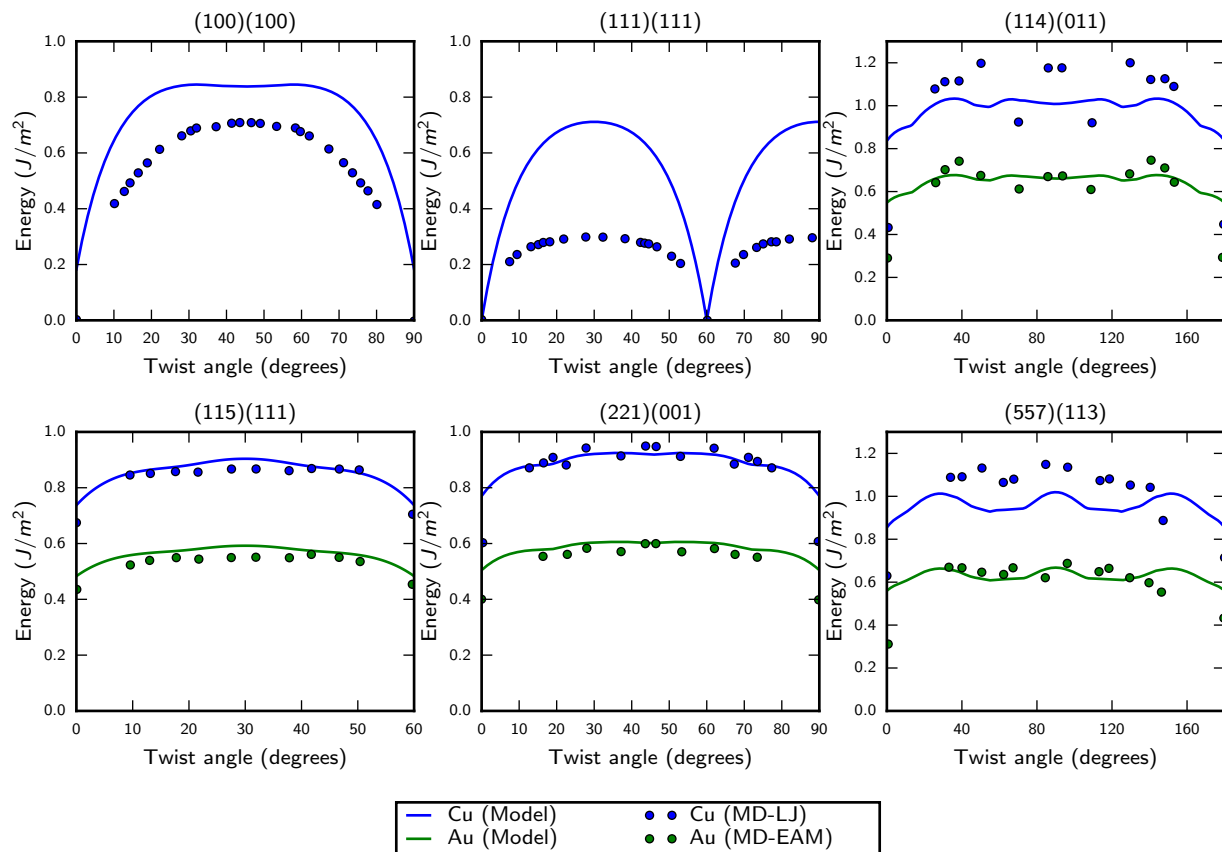


Figure 3.5: FCC TwGB results of the covariance model for Copper and Gold, compared with MD results using EAM (for gold) and LJ (for copper). The boundary planes (constant for all twist angles) are indicated by the graph labels. MD results for symmetric twist from [42], asymmetric twist from [43].

grain boundary planes of the top and bottom crystals.

The results for the STwGBs are, in general, as expected, with deep cusps corresponding to the homogeneous cases at $\theta = 0, 90^\circ$ and $\theta = 0, 60^\circ$. Results are compared to MD work by Wolf [43] in the first two plots in Figure 3.5. However we see a greater difference for the STwGBs than any other of the FCC tests; the $\{111\}$ STwGB showing a particularly high value above the MD results. It appears that the results differ only by a multiplicative constant and we note that the model results could easily be re-scaled for a better fit. However, as the same set of material parameters are used for all GB calculations, it would not be possible to adjust E_0 without significantly altering the fit to other data. We suggest as possible explanations that i) the MD results attain a relaxation state that is inaccessible

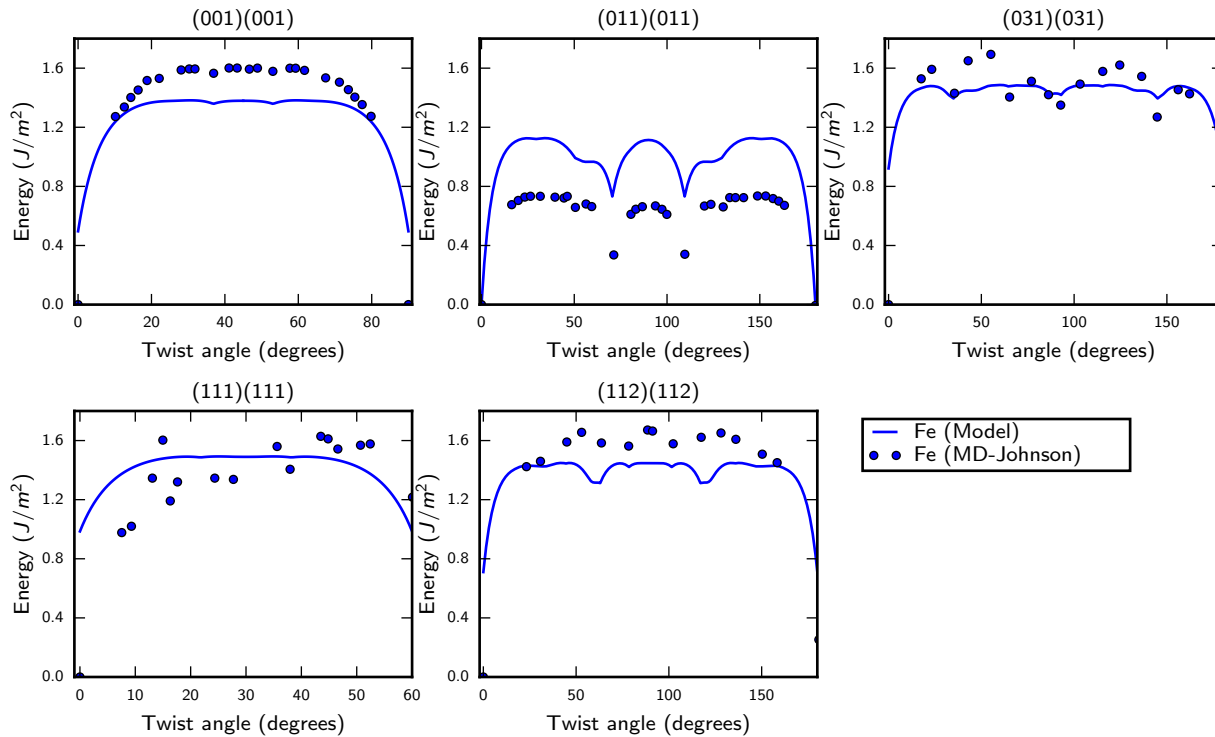


Figure 3.6: BCC StwGB results of the covariance model for α -Iron, compared with MD results using a Johnson potential. MD data from [50, 51].

by the model or ii) the potential used for these MD results differ by a multiplicative constant.

Notably, the results for the asymmetric twist boundaries are more accurate. The results are again compared to MD work by Wolf [43] in the last four plots in Figure 3.5. We notice almost exact agreement for the (115)(111) and (221)(001) boundaries, and a fairly close estimate of the energy for the (114)(011) and (557)(113) boundaries. In addition, we note that the cusp location is predicted exactly as well. The cusp magnitude for some of the cases, particularly (114)(011) and (221)(001), differ significantly.

3.2.6 BCC twist grain boundaries

The final set of grain boundaries investigated were BCC STwGB and ATwGB configurations. The selection of the investigated boundaries was driven by the available MD data.

The results for the model for STwGB boundaries are compared against MD data from Wolf [50, 51]

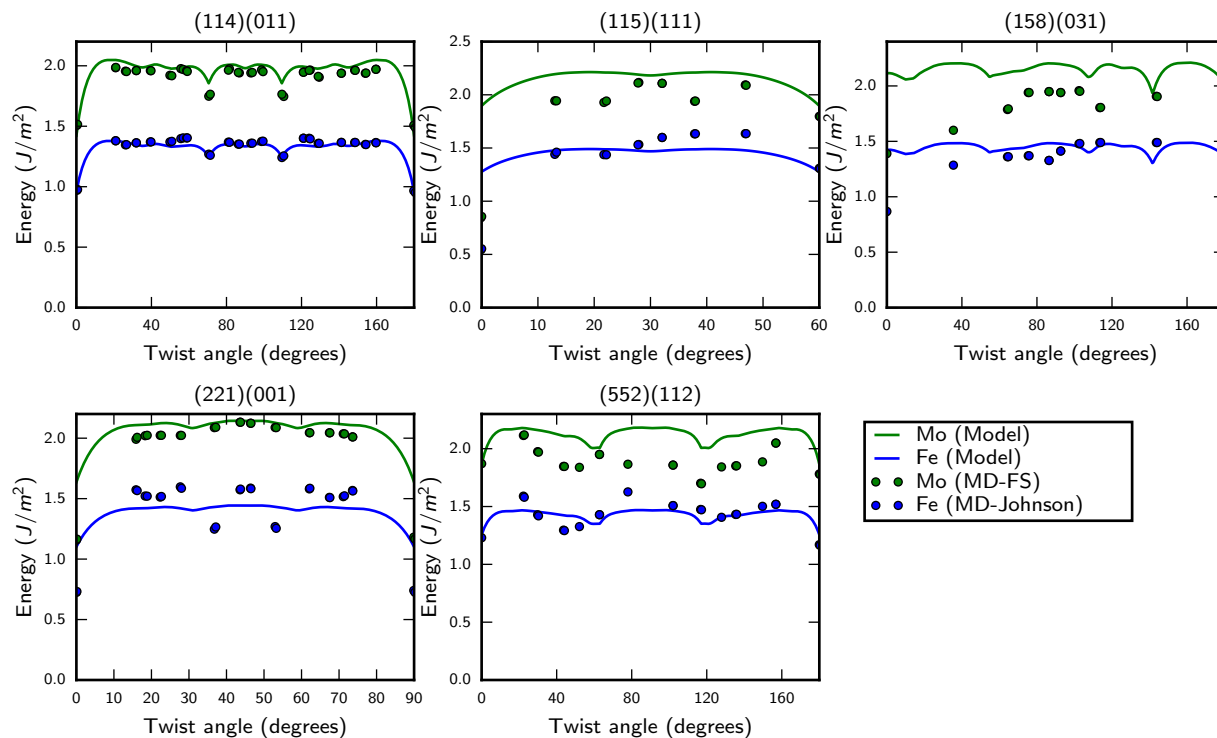


Figure 3.7: BCC ATwGB results of the covariance model for Molybdenum and α -Iron, compared with MD results using a Finnis-Sinclair (FS) potential for Mo and a Johnson potential for Fe. MD results from [51].

in Figure 3.6. For the $\{001\}$ STwGB we notice close agreement with the MD data, matching the minor cusps at $\theta = 37^\circ, 53^\circ$. The results for $\{011\}$ are very similar to the MD results, differing only by a multiplicative factor. For the $\{031\}$, $\{111\}$ and $\{112\}$ boundaries, the MD data is somewhat chaotic and we do not observe a significant trend in the data or the presence of cusps. Further, we notice that the symmetry present in these lattices does not appear to be present in the MD data. Finally we note that, as with previous examples, the absolute values of many of the deep energy cusps differs from that predicted by the model.

Finally, the results for BCC ATwGBs are presented with MD data from Wolf [51] in Figure 3.7. For the (114)(011) we notice an exceedingly close match, with all of the cusps and magnitudes almost identical. For the other families of ATwGBs we notice a somewhat chaotic tendency in the MD data without many distinguishing features. One exception is the data for Fe in the (221)(001) configuration—

we observe apparent cusps at $\sim 37^\circ$ and $\sim 53^\circ$ that are not captured by the data. However, in this case, the cusps are clearly not present in the Mo case, an apparent example of material dependence in the behavior of the energy landscape.

3.3 Conclusions and future work

The aim of this present work was to develop a geometry-based, general, predictive, and general model for the energy anisotropy of grain boundaries. In the formulation of the model, the concept of a lattice density measure is introduced and, from it, the thermalized lattice density function is defined. Based on these definitions we propose a geometric quantity, the covariance, between two thermalized lattice density functions, and we hypothesize that the covariance correlates strongly with the interface energy. Finally, we formulate an energy model based on the covariance.

In the second part of the paper, we specialize the covariance energy model to realistic materials by selecting crystal structures, thermalization mollifiers, and window functions. For each material, three material parameters are introduced, σ, ε, E_0 and these are characterized by comparisons with extensive suites of MD data. The same three parameters are used for all MD comparisons, and are not adjusted on a plot-by-plot basis. We find that the model predicts cusp locations reasonably well, captures trends in the energy closely, and serves as a good approximation of the large-angle tilt boundary energy data. Because all results are given using consistent material parameters and no information regarding cusp location or magnitude, we find this to be strong validation of the predictive ability of the model for a wide range of grain boundary orientations.

Some of the differences between MD and the covariance model are consequences of the uncertainty in the pair potentials used in the MD data, resulting in an unreliable calculation of the absolute value for the excess energy [51]. We can attribute some of the error to the restriction of the model to planar interfaces. Toward resolving this issue, ongoing work will be dedicated to implementing energy relaxation via complex morphology [2]. Finally, we acknowledge that due to the complex energy-relaxing structures that are formed at some interfaces, some energy states are outside of the scope of any low-parameter model. However, we expect that the discrepancy due to these differences to be small.

The encouraging results from this model prompt a wide range of future research directions. Only a small subset of all possible interface orientations has been explored, and we anticipate extensions of the model to alternative orientations, such as asymmetric tilt grain boundaries, to other crystal structures, such as hexagonal close-packed, and to multiphase/multi-material boundaries, such as FCC-BCC Kurdjumov-Sachs. The model has immediate applications to the study of multiple mesoscopic phenomena, such as recrystallization, solidification, severe plastic deformation, etc. We also anticipate the computational adaption of this model to integrate interfacial dynamics into large-scale computational models.

3.4 Acknowledgements

Brandon Runnels and Michael Ortiz would like to thank the NNSA's High Energy Density Laboratory Plasmas program under award number DE-NA0001805. Brandon Runnels thanks the Los Alamos National Laboratory Seaborg Institute for support during Summer 2014. Irene Beyerlein would like to acknowledge support by a Laboratory Directed Research and Development program award number 20140348ER.

Chapter 4

The Convexification Algorithm for Relaxed Energy and Morphology

The previous chapter constructed a model for strictly planar interfaces. In this chapter, we develop a method for computing the energy and morphology of non-planar interfaces by applying relaxation to a planar model. This work builds on many of the developments in the mathematics and materials science community. The result that the faceting construction recovers the convexification of the interface energy function has been reached independently in a number of previous results. In this work, we present the development of the construction and connect it with previous work. The main contribution is the application of the relaxation as a computational algorithm and its ability, when applied using the covariance model, to accurately predict interface energy, morphology, and thermally induced morphological transformations. nn

4.1 Theory

Let us consider an interface between two materials, where the orientation relationship (OR) between the crystals is fixed and the interface energy per unit area is given by $\gamma_\pi : G(3, 2) \rightarrow \mathbb{R}^+$, given the selection of a coordinate system such that the embedding of π aligns with \mathbb{R}^2 . (Here, $G(m, n)$ is the Grassmannian, or the set of n -dimensional linear subspaces in \mathbb{R}^m .) We also define $\hat{\gamma}_\pi : \mathbb{R}^2 \rightarrow \mathbb{R}^+$, the interface energy as a function of the gradient of the interface. In this coordinate system, let the interface between the crystals be \mathbb{R}^2 . Following a formalization along the lines of [98], in the relaxed

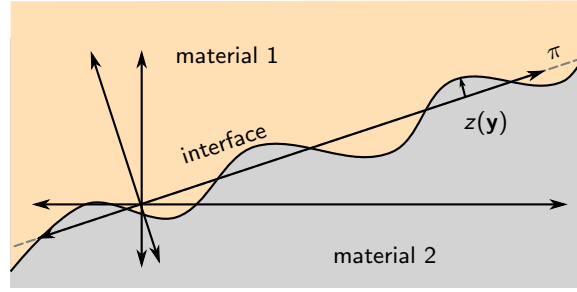


Figure 4.1: We choose a coordinate system between the materials and add z , a perturbation to the interface.

case we let the materials be separated by an interface S that is parameterizable by a single piecewise differentiable graph $z : \mathbb{R}^2 \rightarrow \mathbb{R}$ as shown in Figure 4.1. Then we write the total interface energy with the morphology given by z as

$$\Gamma[z] = \int \hat{\gamma}_\pi(\nabla z(\mathbf{y})) |z(\mathbf{y})| d\mathbf{y}, \quad (4.1)$$

where $|z(\mathbf{y})| = \sqrt{1 + |\nabla z|^2}$ is the density of z at \mathbf{y} , and the integral is over \mathbb{R}^2 . We note that the domain of integration is infinite. Consequently because there is no guarantee of the integrability of $\hat{\gamma}_\pi(\nabla \mathbf{z})|z|$, we conclude that (4.1) is not evaluable in general. Instead, we introduce a normalization to compute the relaxed energy per unit area, and the following notation

$$\int f(\mathbf{y}) d\mathbf{y} \stackrel{\text{def}}{=} \lim_{L \rightarrow \infty} \frac{1}{L^2} \int_{[-\frac{L}{2}, \frac{L}{2}]^2} f(\mathbf{y}) d\mathbf{y}. \quad (4.2)$$

Then we define the energy per unit area as

$$\gamma(\pi, z) = \int \hat{\gamma}_\pi(\nabla z(\mathbf{y})) |z(\mathbf{y})| d\mathbf{y}, \quad (4.3)$$

where we see that the planar energy per unit area follows as a special case of (4.3) for $z = 0$:

$$\gamma(\pi, 0) = \int \hat{\gamma}_\pi(\mathbf{0}) d\mathbf{y} = \gamma(\pi). \quad (4.4)$$

Suppose we attempt to find the minimizing z for the functional in (4.3). Let $z = \boldsymbol{\xi} \cdot \mathbf{y}$. Then

$$\gamma(\boldsymbol{\pi}, z) = \int \hat{\gamma}_{\boldsymbol{\pi}}(\boldsymbol{\xi}) \sqrt{1 + |\boldsymbol{\xi}|^2} d\mathbf{y} = \hat{\gamma}_{\boldsymbol{\pi}}(\boldsymbol{\xi}) \sqrt{1 + |\boldsymbol{\xi}|^2} \quad (4.5)$$

whence we see that the optimal graph z^* is given by $z^*(\mathbf{y}) = \boldsymbol{\xi}^* \cdot \mathbf{y}$, where

$$\boldsymbol{\xi}^* = \operatorname{arginf}_{\boldsymbol{\xi}} \hat{\gamma}_{\boldsymbol{\pi}}(\boldsymbol{\xi}) \sqrt{1 + |\boldsymbol{\xi}|^2}. \quad (4.6)$$

Apparently, minimization of (4.3) results in a divergent planar graph. But we are interested in finding the z that minimizes (4.3) without large-scale deviation from the planar interface. To effect this behavior we introduce the Moreau-Yosida regularization

$$\gamma_{\varepsilon}(\boldsymbol{\pi}, z) = \int \hat{\gamma}_{\boldsymbol{\pi}}(\nabla z) |z(\mathbf{y})| d\mathbf{y} + \frac{1}{\varepsilon} \int_{\pi} z^2 d\mathbf{y}, \quad (4.7)$$

where ε is a penalty parameter that drives $z \rightarrow 0$ as $\varepsilon \rightarrow 0$. Let $\{z_n\}_{n=0}^{\infty}$ be a sequence of graphs converging to 0 as $n \rightarrow \infty$. If

$$\lim_{\varepsilon \rightarrow 0, n \rightarrow 0} \gamma_{\varepsilon}(\boldsymbol{\pi}, z_n) \geq \gamma(\boldsymbol{\pi}, 0) \quad (4.8)$$

then γ is said to be *lower-semicontinuous*. In this case then $z = 0$ is a minimizer for (4.7), the minimizing interface is said to be *planar*.

The interesting behavior happens when γ lacks lower-semicontinuity. In this case, the minimizer z^* for (4.7) is not attained in general, and the best one can hope for is to choose a sequence of functions that approaches the infimum of (4.7) [86]. If a sequence of functions $\{z_n\}$ satisfies

$$\lim_{z_n \rightarrow 0} \gamma_{\varepsilon}(\boldsymbol{\pi}, z) = \inf_z \gamma_{\varepsilon}(\boldsymbol{\pi}, z) \quad (4.9)$$

then $\{z_n\}$ is said to be a *minimizing sequence*. Given the existence of a minimizing sequence [86], the functional

$$\gamma_C(\boldsymbol{\pi}) = \lim_{\varepsilon \rightarrow 0} \inf_z \gamma_{\varepsilon}(\boldsymbol{\pi}, z) \quad (4.10)$$

is said to be the *relaxed* interface energy per unit area or, alternatively, the *relaxation of* γ . We note that i) γ_C is itself lower-semicontinuous and therefore is its own relaxation and ii) two planar interface energy per area functions γ_1, γ_2 may have the same relaxation.

4.1.1 Faceting construction

With the introduction of the “faceting” terminology, we acknowledge the two meanings of the word *facet* in the literature, and to avoid ambiguity we clarify here our use of the word. The first meaning is used to describing the geometry of a large polyhedral crystal, the planar faces are referred to as facets. The second refers to the zig-zag structure observed on the atomic scale. In this work we shall use the latter definition. When it is necessary to distinguish between the two we shall refer to the former as *macrofacets* and the latter as *microfacets*.

Using facets, we seek to find a minimizing sequence that approaches the infimum of γ_ε , in order to construct γ_C . Let us make the following definition:

Definition 4.1 (Facet sequence). *A sequence of piecewise differentiable functions $\{z_n\}_{n=0}^\infty$ is said to be an m -facet sequence if it satisfies the following properties:*

i) *Piecewise affine: for each n there is a cover $\{\Omega_i^n\}_{i=1}^m$ of \mathbb{R}^2 and a collection $\{\xi_i\}_{i=1}^m \subset G(3, 2)$ so that*

$$\nabla z_n(\mathbf{y}) = \xi_i \quad \forall \mathbf{y} \in \Omega_i^n \quad i = 1 \dots m, \quad (4.11a)$$

and there is a collection $\{\mu_i\}_{i=1}^m$ so that

$$\mu_i = \lim_{L \rightarrow \infty} \frac{|\Omega_i^n \cap [-\frac{L}{2}, \frac{L}{2}]^2|}{L^2} \quad (4.11b)$$

for all n .

ii) *Pointwise convergence:*

$$\lim_{n \rightarrow \infty} |z_n(\mathbf{y})| = 0 \quad \forall \mathbf{y} \in \mathbb{R}^2 \quad (4.11c)$$

iii) *Weak derivative convergence:*

$$\int \nabla z \, d\mathbf{y} = \mathbf{0} \quad (4.11d)$$

The substitution of (4.11a) into (4.11d) yields the linear system

$$\int \boldsymbol{\xi} \, d\mathbf{y} = \sum_{i=1}^m \mu_i \boldsymbol{\xi}_i = \mathbf{0}. \quad (4.12)$$

Let $\{z_n\}$ be an m -facet sequence with gradients $\{\boldsymbol{\xi}_i\}$ and area fractions $\{\mu_i\}$. Then the relaxation corresponding to z_n of the energy is

$$\gamma_\varepsilon(\boldsymbol{\pi}, z_n) = \int \hat{\gamma}_\pi(\nabla z_n) \sqrt{1 + |\nabla z|^2} \, d\mathbf{y} + \frac{1}{\varepsilon} \int z^2 \, d\mathbf{y} = \sum_{i=1}^m \mu_i \hat{\gamma}_\pi(\boldsymbol{\xi}_i) \sqrt{1 + |\boldsymbol{\xi}_i|^2} + \frac{1}{\varepsilon} \int z^2 \, d\mathbf{y}. \quad (4.13)$$

By (4.11c), in the limit as $n \rightarrow \infty$,

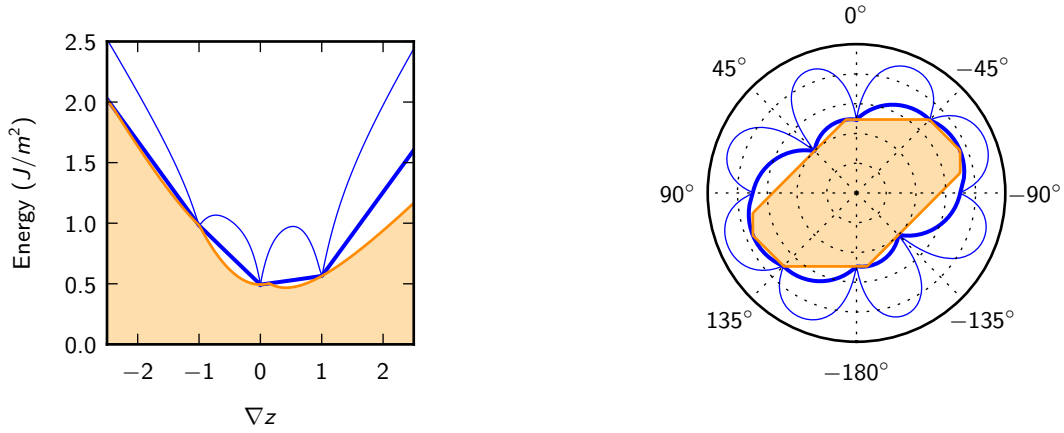
$$\lim_{n \rightarrow \infty} \gamma_\varepsilon(\boldsymbol{\pi}, z_n) = \sum_{i=1}^m \mu_i \hat{\gamma}_\pi(\boldsymbol{\xi}_i) \sqrt{1 + |\boldsymbol{\xi}_i|^2}. \quad (4.14)$$

Substituting into (4.10), and restricting to a minimization over all m -facet sequences, we obtain the following discrete optimization problem

$$\begin{aligned} \gamma_C(\boldsymbol{\pi}) &= \inf_{\{\boldsymbol{\xi}_i\}, \{\mu_i\}} \sum_{i=1}^m \mu_i \hat{\gamma}_\pi(\boldsymbol{\xi}_i) \sqrt{1 + |\boldsymbol{\xi}_i|^2} \\ &\text{subject to } \sum_{i=1}^m \mu_i \boldsymbol{\xi}_i = \mathbf{0} \quad \sum_{i=1}^m \mu_i = 1 \quad \mu_i \geq 0. \end{aligned} \quad (4.15)$$

The solution of (4.15) over the set of m -facet sequences is said to be the m -relaxation of γ . If $m \geq 3$ then the solution of (4.15) is the *convexification* of γ [114]. Solutions of (4.15) are a set of optimal facet gradients and area fractions; the corresponding facet graph is referred to as the *optimal facet pattern*. We note that (4.15) also generates the Young measure [115]

$$\nu = \sum_{i=1}^n \mu_i^* \delta_{\boldsymbol{\xi}_i^*}, \quad (4.16)$$



(a) Convexification (bold line) of $\sqrt{1 + |\nabla z|^2} \gamma$ (light line) projected as a function of ∇z , the gradient of the interface.

(b) 1-sphere convexification (bold line) of γ (light line) projected as a function of \mathbf{n} , the normal vector to the interface.

Figure 4.2: Two plots of the same data demonstrating the connection between convexity in gradient space and convexity on the unit sphere. The “convex hull” on the unit sphere is equivalent to the convex hull of the energy multiplied by $\sqrt{1 + |\nabla z|^2}$. (The shaded region is the Wulff construction.)

where μ_i^*, ξ_i^* are solutions of (4.15) and δ_x are the Dirac measures centered at \mathbf{x} .

4.1.2 Convexification on the unit sphere

The formulation of the convexification problem using graphs and gradients is useful for connection with other gradient problems; however, the formulation (4.15) proves cumbersome in application. In addition, that the problem is posed in terms of gradients is problematic because i) we cannot guarantee differentiability of the interface and ii) solutions may drive the gradient to be infinite.

There exists a natural duality between $G(3,2)$, and $S_2 = \{\mathbf{x} \in \mathbb{R}^3 : |\mathbf{x}| = 1\}$, the unit 2-sphere in 3D. We use the Hodge star operator $*$ to convert between the two dual spaces. For S_2 we define the embedding $f : S_2 \rightarrow \mathbb{R}^3$ and the submersion $g : \mathbb{R}^3 \rightarrow S_2$. Finally, we define the homeomorphism $h : \mathbb{R}^2 \rightarrow S_2$

$$f(h(\xi)) = \frac{1}{\sqrt{1 + |\xi|^2}} \begin{bmatrix} -\xi_1 \\ -\xi_2 \\ 1 \end{bmatrix}, \quad (4.17)$$

which, interpreted informally, converts the gradient of a plane to its normal vector. These definitions enable us to write (4.15) as

$$\begin{aligned} \gamma_C(\boldsymbol{\pi}) &= \inf_{\{\boldsymbol{\xi}_i\}, \{\mu_i\}} \sum_{i=1}^m \gamma_{\boldsymbol{\pi}}(*h(\boldsymbol{\xi}_i)) (\mu_i \sqrt{1 + |\boldsymbol{\xi}_i|^2}) \\ \text{subject to } & \sum_{i=1}^m \frac{\mu_i \sqrt{1 + |\boldsymbol{\xi}_i|^2}}{\sqrt{1 + |\boldsymbol{\xi}_i|^2}} \boldsymbol{\xi}_i = \mathbf{0} \quad \sum_{i=1}^m \frac{\mu_i \sqrt{1 + |\boldsymbol{\xi}_i|^2}}{\sqrt{1 + |\boldsymbol{\xi}_i|^2}} = 1 \quad \mu_i \sqrt{1 + |\boldsymbol{\xi}_i|^2} \geq 0. \end{aligned} \quad (4.18)$$

The first and second constraints combine in the following way:

$$\sum_{i=1}^m \frac{\mu_i \sqrt{1 + |\boldsymbol{\xi}_i|^2}}{\sqrt{1 + |\boldsymbol{\xi}_i|^2}} \begin{bmatrix} (\boldsymbol{\xi}_i)_1 & \boldsymbol{\xi}_i)_2 \\ 1 \end{bmatrix} = \sum_{i=1}^m \mu_i \sqrt{1 + |\boldsymbol{\xi}_i|^2} f(h(\boldsymbol{\xi}_i)) = \begin{bmatrix} 0 \\ 0 \\ 1 \end{bmatrix}. \quad (4.19)$$

Let $\lambda_i = \mu_i \sqrt{1 + |\boldsymbol{\xi}_i|^2}$ and let $\boldsymbol{\pi}_i = *h(\boldsymbol{\xi}_i)$. Then

$$\gamma_C(\boldsymbol{\pi}) = \inf_{\{\boldsymbol{\pi}_i\}, \{\lambda_i\}} \sum_{i=1}^m \lambda_i \gamma_{\boldsymbol{\pi}}(\boldsymbol{\pi}_i) \quad \text{subject to} \quad \sum_{i=1}^m \lambda_i f(*\boldsymbol{\pi}_i) = \begin{bmatrix} 0 \\ 0 \\ 1 \end{bmatrix}, \quad \lambda_i \geq 0. \quad (4.20)$$

Finally, transforming coordinates, we have the result for convexity on the unit sphere

$$\gamma_C(\boldsymbol{\pi}) = \inf_{\{\boldsymbol{\pi}_i\}, \{\lambda_i\}} \sum_{i=1}^m \lambda_i \gamma(\boldsymbol{\pi}_i) \quad \text{subject to} \quad \sum_{i=1}^m \lambda_i f(*\boldsymbol{\pi}_i) = f(*\boldsymbol{\pi}), \quad \lambda_i \geq 0 \quad (4.21)$$

whence we see that the facet minimization problem of Cahn [92] is equivalent to the standard convexification (4.15). The solution to this program yields both i) the value for the relaxed energy γ_C and ii) the minimizing facet planes $\{\boldsymbol{\pi}_i\}$ and their area fractions $\{\lambda_i\}$. We note that the usual constraint $\sum_i \mu_i = 1$ is effectively replaced by $\sum_i \lambda_i \geq 1$. For the relaxed energy to remain bounded, it is necessary that the energy provided by γ be nonnegative.

The problem of convexification was previously treated by Jean Taylor, who presented an alternative

method for finding the convexification γ_C of a function γ on the unit sphere [93].

$$\gamma_C(\boldsymbol{\pi}) = \sup_{\boldsymbol{\pi}_1} \inf_{\boldsymbol{\pi}_2} \frac{(\boldsymbol{\pi}_1, \boldsymbol{\pi})}{|(\boldsymbol{\pi}_1, \boldsymbol{\pi}_2)|} \gamma(\boldsymbol{\pi}_2) \quad (4.22)$$

While the same result is produced, information about the facet sequence morphology is lost.

4.2 Implementation

The relaxation construction relies on the existence of a general interface energy function $\gamma(\boldsymbol{\pi})$. Here, we present an algorithm for computing energy and morphology of grain boundaries by using the relaxation algorithm with the covariance model.

4.2.1 Covariance model for interface energy

We begin with a brief overview of the covariance method for interface energy. [1] is a general reference for this section. The key element of the covariance method is the construction of “density measures” $\varrho : C_0(\mathbb{R}^3) \rightarrow \mathbb{R}^+$ defined by

$$\int_B d\varrho(\mathbf{x}) = \langle N_B \rangle \quad \forall \text{ measurable } B \subset \mathbb{R}^3, \quad (4.23)$$

where $\langle N_B \rangle$ is the expected number of atoms in B . The density measure is periodic allowing ϱ to be expressed in terms of a Fourier series; however, it is necessary to regularize ϱ in order to make the Fourier series summable. This is effected by thermalization using the MaxEnt formalism. The end result is that the rigid lattice density measure ϱ is convolved with a thermalization function ψ to give a regularized lattice density function ρ . The thermalization function is determined by the choice of atomic embedding energy potential. As in the previous work we choose a quadratic potential, resulting in a Gaussian thermalization function

$$\psi(\mathbf{x}) = \frac{1}{\sigma^3 \pi^{3/2}} e^{-\|\mathbf{x}\|^2/\sigma^2}, \quad (4.24)$$

Table 4.1: Material parameters for covariance model

	Cu (FCC)	Au (FCC)	Al (FCC)	Mo (BCC)	Fe (BCC)
$E_0(J/m^2)$	1.45	0.95	750	2.525	1.950
σ/α	0.175	0.175	.175	0.19	0.19
ε	0.5	0.5	.175	0.25	0.25

where the quantity $\sigma^2 = 2k_B T/w_0$, k_B is Boltzmann's constant, T is the absolute temperature in Kelvins, and w_0 is a material parameter for the quadratic potential. The interface energy is computed as a linear function of the covariance, a geometric quantity given as

$$c[\rho^b, \rho^w] = \int \rho^b(P^T \mathbf{y}) \rho^w(P^T \mathbf{y}) \phi(\mathbf{y}) d\mathbf{y}, \quad (4.25)$$

where $P^T : \mathbb{R}^2 \rightarrow \mathbb{R}^3$ embeds \mathbb{R}^2 in \mathbb{R}^3 and $\phi(\mathbf{y})$ is a window function. We choose a window function ϕ so that

$$\hat{\phi}(\mathbf{k}) = e^{-\|\mathbf{k}\|/\varepsilon}, \quad (4.26)$$

where ε is a material parameter. With these definitions the interface energy is given in terms of the covariance as

$$\gamma(\rho^b, \rho^w) = E_0 \left(1 - \frac{c[\rho^b, \rho^w]}{\sqrt{c_0[\rho^b] c_0[\rho^w]}} \right), \quad (4.27)$$

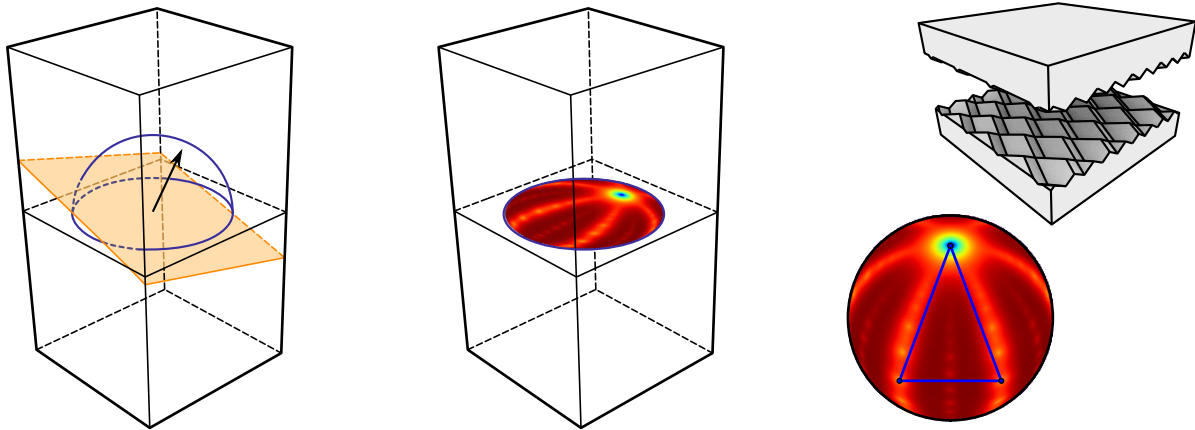
where

$$c_0[\rho^{b,w}] = \inf_{R \in SO(3)} c[\rho^{b,w}(\cdot, R), \rho^{b,w}(\cdot, R)]. \quad (4.28)$$

Generally, there are three parameters for each test: E_0 , σ , and ε . Consistent values for these parameters are used for all tests in this work, and values are given in Table 4.1.

4.2.2 Stereographic projections of interface energy surfaces

The behavior of $\gamma(\mathbf{n})$ drastically affects the faceting behavior (and consequently the relaxed energy) of the interface, so it is crucial that the surface be visualized in an intuitive way. In this work we visualize the energy surface via a stereographic projection. Figure 4.3 illustrates the process for generating



(a) Fixing the orientation relationship between the upper and lower crystals, all remaining interface configurations are determined by normal vector, mapping interface energy to the unit sphere.

(b) The upper unit 2-hemisphere is homeomorphic to the unit 2-ball over which the energy is plotted. For example, the value at the center corresponds to the normal vector $\mathbf{n} = [0\ 0\ 1]^T$.

(c) The relaxation algorithm is used to compute the energy-minimizing facets. Facet configurations are represented as nodes on the stereographic plot or visualized as a faceted surface.

Figure 4.3: Faceting algorithm

stereographic visualizations: the orientation relationship is fixed and the interface is allowed to vary. The set of all normal vectors is equivalent to the unit sphere, and therefore it is convenient to associate the energy of each interface inclination with its corresponding point on the unit sphere, generating a plot of energy over the sphere. γ is clearly parity invariant, that is, $\gamma(\mathbf{n}) = \gamma(-\mathbf{n})$, indicating that the interface need not be oriented. As a consequence, the unit hemisphere ($S_2^+ = \{\mathbf{x} \in \mathbb{R}^3 : |\mathbf{x}| = 1, x_3 \geq 0\}$) is sufficient to capture all of the interface behavior. Because it is homeomorphic to the unit 2-ball, we use the projection $(n_1, n_2, n_3) \mapsto (n_1, n_2)$ to visualize the energy surface.

Energy surface plots provide a convenient means of describing optimal facet patterns. A collection of normal vectors can be visualized as a collection of points, and the resultant facet pattern as a convex polygon connecting them. We see that the constraint in (4.21) indicates that a set of facet vectors $\{\mathbf{n}\}$ form a facet pattern only if their convex hull contains the origin; consequently a polyhedral representation of a facet pattern gives an immediate indication of their compatibility.

4.2.3 Procedure

We implement a basic grid search algorithm to compute the relaxation of γ . We use the following procedure for each relaxed energy point. First the orientation relationship of the crystals is fixed, so that $\gamma = \gamma(\mathbf{n})$. A uniform grid of normal vectors $\{\mathbf{n}_i\} \subset \mathcal{S}_2^+$ is generated, and the interface energy model is used to compute the energy at each point, giving a set of values $\{\lambda_i\} \subset \mathbb{R}^+$.

We refer to “m-relaxation” as the relaxation given by solving (4.21) in the space of m-facet sequences; e.g. a 2-relaxation returns the optimal 2-facet pattern and the corresponding relaxed energy. Since m-facets \subset (m+1)-facets, it follows that $\gamma_C^m \geq \gamma_C^{m+1}$ with the superscript of γ_C denoting the order of the relaxation.

Algorithm 1 outlines the general procedure for computing the 3-relaxation; the algorithm for other relaxation orders (particularly, 2) is almost identical differing only by the number of nested loops. The basic procedure has $\mathcal{O}(n^m)$ time complexity, where n is the number of grid points and m is the order of the faceting. A number of filters can be exploited that improve the efficiency of the computation, such as selective sampling, partitioning of the domain, and numerical annealing. In addition, by exploiting known symmetries of γ , the search space can be significantly reduced. However, we find that the basic method does not require extensive improvement in order to return results.

4.2.4 Computation of results

The planar results were generated using the same C++ code as the previous chapter, with additional code added to compute the faceting relaxation. Threading was implemented using pthreads so that the program was run with 7-8 processes. The computation of each set of data (with high enough resolution for the relaxation method to accurately find the minimal cusp value) was generally generally completed in 1-2 seconds, although this number varied depending on the value of the dimensionless temperature. The relaxation method was used on each dataset to compute the optimal faceting pattern. For many cases the 2- and 3-relaxation results were identical, although in some cases it was necessary to run a full 3-relaxation. With datasets large enough to find cusps accurately and with no data reduction, each relaxation computation took approximately 1-2 seconds to complete.

Algorithm 1 Grid search algorithm to compute $\gamma_C(\mathbf{n})$

```

Require:  $\mathbf{n} \cdot \mathbf{n} = 1$ 
create tuple  $(\{\mathbf{n}_i\}, \{\gamma_i\})$  using planar model
 $\gamma_{\min} = \infty$ 
for all  $(\mathbf{n}_1, \gamma_1)$  in  $(\{\mathbf{n}_i\}, \{\gamma_i\})$  do
  for all  $(\mathbf{n}_2, \gamma_2)$  in  $(\{\mathbf{n}_i\}, \{\gamma_i\})$  do
    for all  $(\mathbf{n}_3, \gamma_3)$  in  $(\{\mathbf{n}_i\}, \{\gamma_i\})$  do
       $N = [\mathbf{n}_1, \mathbf{n}_2, \mathbf{n}_3]$ 
      if  $\det N = 0$  then
        continue
      end if
       $\boldsymbol{\lambda} = N^{-1}\mathbf{n}$ 
      if not  $\boldsymbol{\lambda} \in \mathbb{R}^{3+}$  then
        continue
      end if
      if  $\gamma_{\min} > \lambda_1\gamma_1 + \lambda_2\gamma_2 + \lambda_3\gamma_3$  then
         $\gamma_{\min} = \lambda_1\gamma_1 + \lambda_2\gamma_2 + \lambda_3\gamma_3$ 
      end if
    end for
  end for
end for
 $\gamma_C = \gamma_{\min}$ 
return  $\gamma_C$ 

```

4.3 Examples

We validate the use of the convexification method algorithm by using the covariance method for the unrelaxed planar model. The range and scope of the covariance model with the enhancements provided by convexification is demonstrated through comparison to a wide range MD and experimental data for several grain boundary configurations. In this section we use MD results from consistent authors where possible, though more recent MD results are available in some cases. In Appendix B we include additional comparisons with results from more recent MD calculations, as well as experimental results and low-angle tilt models.

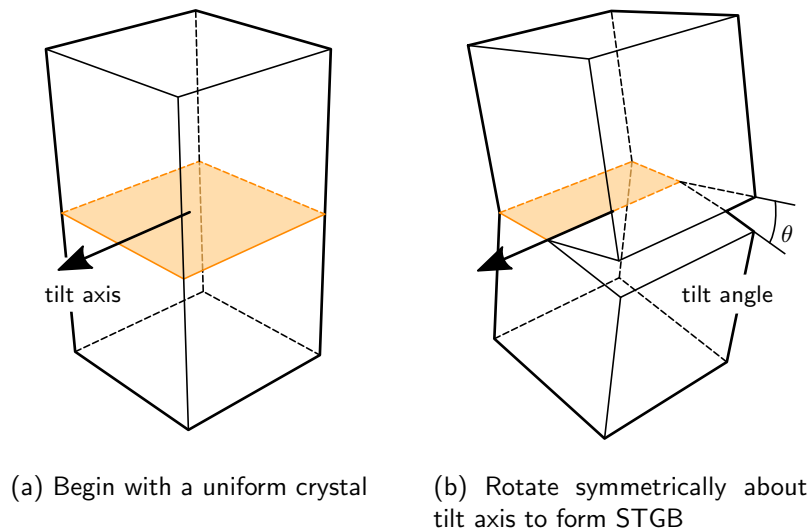


Figure 4.4: Geometry of symmetric tilt grain boundaries

4.3.1 Symmetric tilt grain boundaries

The set of symmetric tilt grain boundaries (STGBs) forms one of the most basic classes of nontrivial grain boundaries. STGBs are obtained by beginning with a uniform crystal and rotating the upper and lower halves symmetrically with respect to a tilt axis contained in the prescribed interface (Figure 4.4). Consequently, STGBs are defined by i) the crystallographic direction (in Miller indices) corresponding to the *tilt axis* that remains constant, ii) the total *tilt angle* between the two crystals about the tilt axis, and iii) the direction corresponding to the *initial normal axis* to the homogeneous interface. Because STGBs are by definition symmetric about the constant interface plane, the tilt axes must lie within a symmetry plane of the crystal [58]; as such the class of STGBs is limited to a selection of tilt axes. For cubic materials the STGB tilt axes are $\langle 100 \rangle$, $\langle 110 \rangle$, $\langle 111 \rangle$, and $\langle 112 \rangle$, and we use a wide selection of MD data for comparison [41, 49].

The results in this section and in section 4.3.2 follow the results in the previous work by the authors on the covariance model for interface energy [1]. As discussed in the original formulation, the planar restriction on the covariance model results in overprediction of the energy of some boundaries, particularly for boundaries in homogeneous crystals. For many of the cases described we find that the planar model

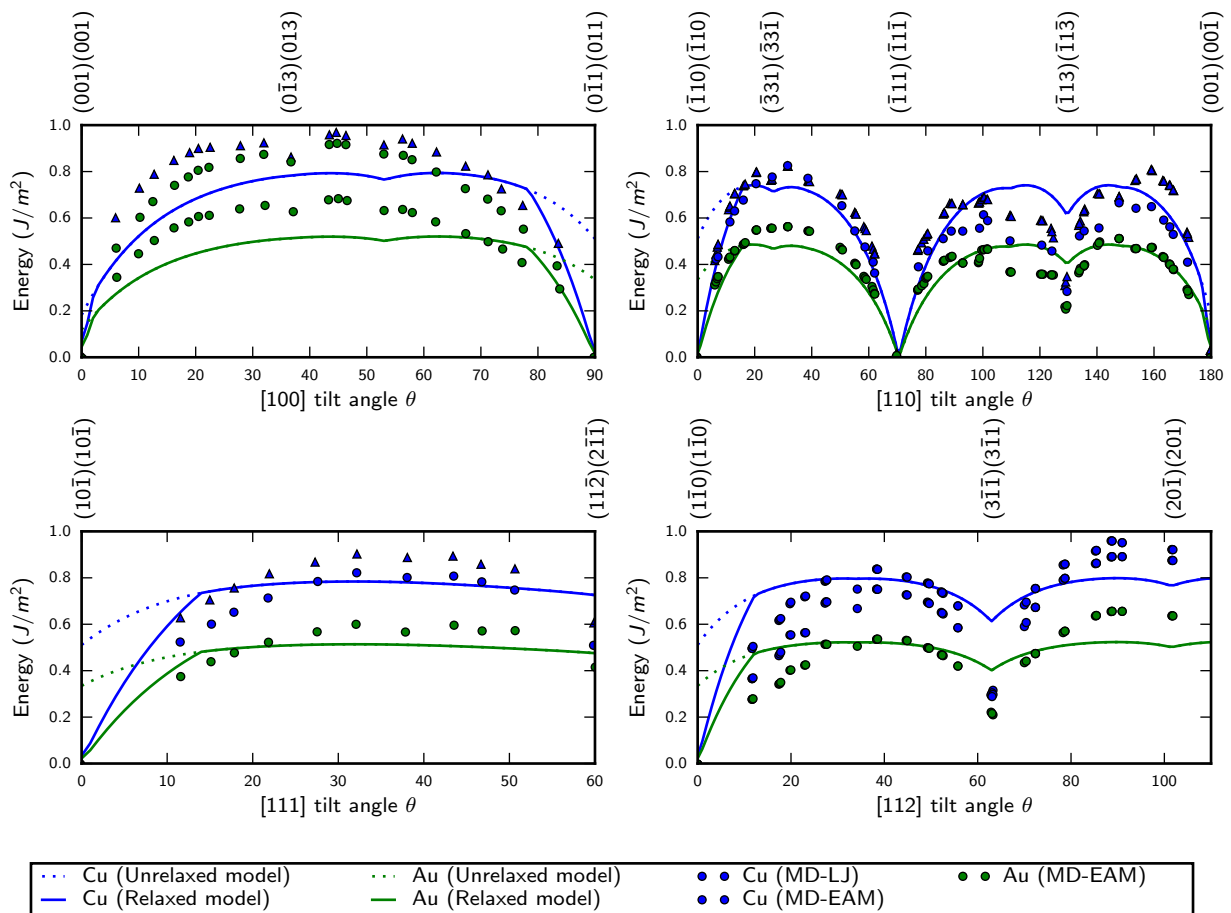


Figure 4.5: FCC STGB results of the covariance model (relaxed and unrelaxed) for Copper and Gold, compared with molecular dynamics results using the Embedded Atom Method (EAM) and Lennard-Jones (LJ) potentials. MD results from [41]. Annotations on the top indicate the boundary plane for the top crystal at cusp locations.

suffices and that no change is effected by relaxation. For a thorough discussion of the behavior of the grain boundary energy for the unrelaxed regions we refer the reader to the original analysis. In this work we are concerned with the effect of relaxation; consequently we discuss the improvements on the unrelaxed results only.

In Figure 4.5 we observe the effect of relaxation on the set of FCC STGBs. The original results for the planar model are plotted using a finely dashed line and the results for the relaxed model are plotted using a solid line; results for Copper and Gold are plotted in blue and green, respectively. We note that, in general, the unrelaxed and relaxed results are coincident; relaxation only occurs in the regions where

they diverge.

For tilt about the [100] axis, relaxation occurs for $0^\circ \leq \theta < 5^\circ$ and $75^\circ < \theta \leq 90^\circ$. The result for the $0^\circ \leq \theta < 5^\circ$ region corrects a discrepancy in the planar model; at $\theta = 0$ the crystal is uniform and should therefore have zero grain boundary excess energy. The relaxation method effects this energy reduction by creating facets for the $\{111\}$ boundary planes, obtained by rotating the interface about the $\{110\}$ axes. That the resultant energy would be reduced to zero follows by the observation that the $\{111\}$ family of STGBs are energy minimizers; from the [110] tilt plot we see that the unrelaxed energy is zero for the $\{111\}$ case. Consequently we observe that this relaxation construction occurs for all $\{100\}$ symmetric tilt boundaries, (the other occurring for [110] tilt at $175^\circ < \theta \leq 180^\circ$).

For the [110], [111], and [112] tilt boundaries we observe significant relaxation for $0^\circ \leq \theta < 15^\circ$, all of which correspond to the case of near-uniform crystals. As before, by examining the energy plot we see that the relaxation to zero is effected by convexification with zero-energy $\{111\}$ facets.

In Figure 4.6 we perform a similar set of tests using materials with BCC crystal structure, Molybdenum (blue) and α phase Iron (green). As with the FCC results, the results from the planar model are plotted with a hashed line, while the relaxed model results are plotted using a solid line. For almost the entire range of tilt angles for all four cases, no relaxation occurs and the relaxed plot is consequently coincident with that of the planar model. The only relaxation that is observed to occur in these figures is: for [100] tilt, $0^\circ \leq \theta < 5^\circ$; for [110] tilt, $175^\circ < \theta \leq 180^\circ$. The reason for the relaxation occurring exclusively for these configurations is intuitive and is consistent with that of the FCC tilt case. Evaluation of the covariance model in the uniform crystal case shows that there exists an anisotropy in the energy. The absolute minimum energy value is attained in the uniform crystal orientation corresponding to the most densely packed plane: for FCC the $\{111\}$ plane and for BCC the $\{110\}$, and the energy for all uniform crystal orientations is reduced to zero by convexifying between these minimal energy orientations. As a result, no relaxation occurs in the BCC STGB case when the uniform crystal boundary is already minimized; because $\theta = 0$ corresponds to a $\{110\}$ plane for most of the cases, no relaxation occurs.

At this point the reader may raise an objection regarding the consistency of the use of a relaxation

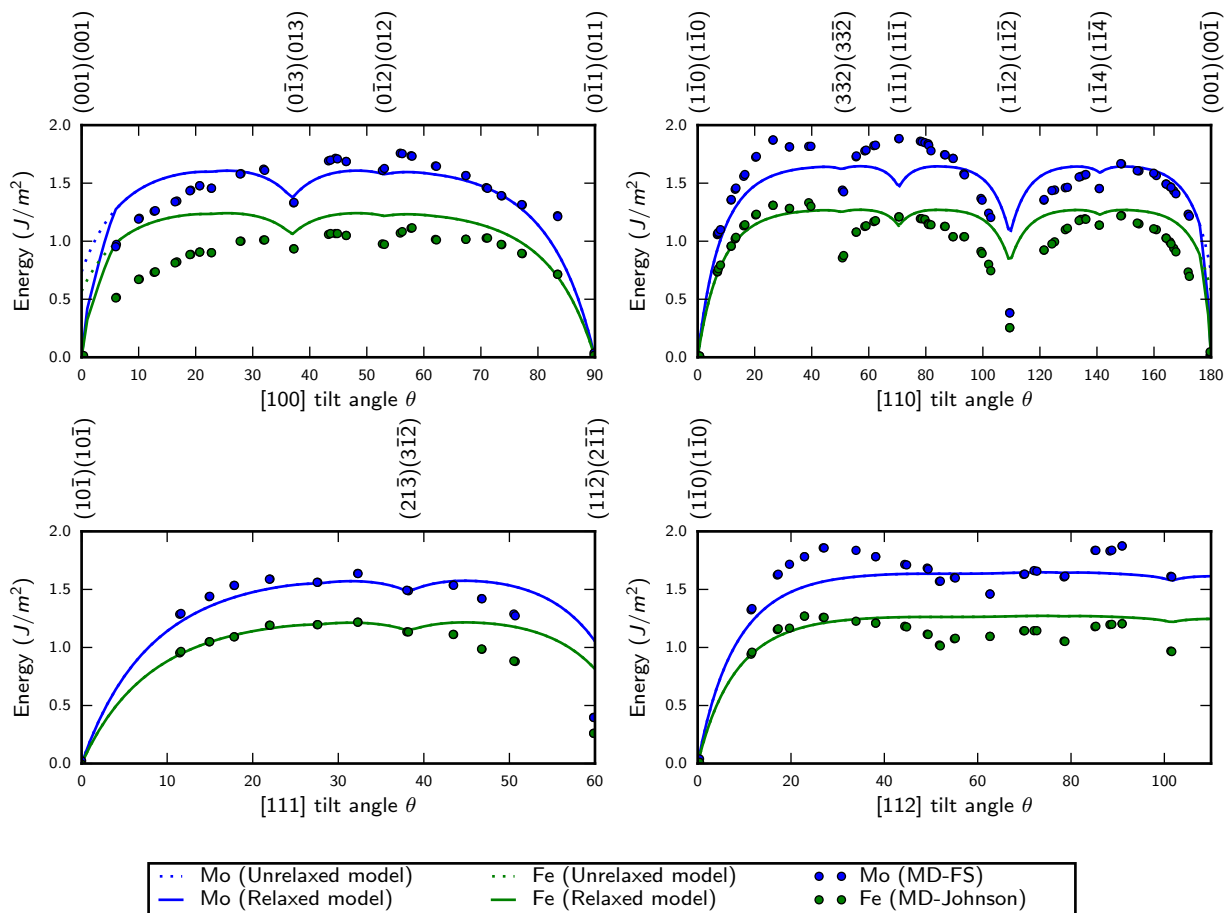


Figure 4.6: BCC STGB results of the covariance model (relaxed and unrelaxed) for Molybdenum and α -Iron, compared with MD results using FS (for Mo) and Johnson (for Fe) potentials. MD results from [49]. Annotations on the top indicate the boundary plane for the top crystal at cusp locations.

construction with symmetric tilt grain boundaries: STGBs are generally observed to be planar, so any faceting construction of the interface results in a departure from observed (and simulated) behavior. In response we remark that all relaxation for STGBs occurs at or very near to the uniform crystal case. Uniform crystals by definition have no physical boundary; the supposed interface between them is reduced to a construction. Thus there is no reason why the constructed interface need be planar; on the contrary, because we expect the constructed boundary in a uniform crystal to be densely packed, we would expect that it follows the densely packed regions to some extent.

We also note that relaxation does not occur for the majority of the tilt configurations. That is, the

energy surface for most STGBs is sufficiently convex so that it is not possible to reduce the energy by faceting. Consequently we conclude that the observed planar behavior of STGBs may be explained by the observation that planar STGBs (except in the uniform crystal case) are energy minimizers.

The relaxation resolves the original discrepancy of nonzero energy at uniform boundaries in the results for the unrelaxed model. For all of the symmetric tilt grain boundaries, and for the FCC cases in particular, we observe that the covariance model used with the relaxation theory produces results that very closely match results from MD calculations.

4.3.2 Twist grain boundaries

For every possible grain boundary there exists a corresponding set of twist grain boundaries (TwGB). TwGBs are generated by rotating the top and bottom crystals of any grain boundary antisymmetrically about a twist axis that is normal to the interface plane (Figure 4.7.) Any TwGB is described by its two boundary planes and the twist angle. A subset of the family of TwGBs are symmetric twist grain boundaries (STwGB). A TwGB is a STwGB if the crystal is uniform when the twist angle $\theta = 0$. A TwGB is specified by a single boundary plane. The set of asymmetric twist grain boundaries (ATwGB) are all the TwGBs that are not STwGBs.

The selection of TwGBs that we use for comparison is driven by the availability of molecular dynamics data. For FCC-FCC TwGBs we compare with two STwGB cases and four ATwGB cases. The results for the comparison are included in Figure 4.8. As with the previous section, the planar results are represented with a hashed line, and the relaxed with a solid line. Only data for copper was available for the FCC STwGB case, so we only include the results for copper STwGB. For the remainder of the cases we compare results for both copper and gold. As with the previous work, we observe the greatest discrepancy in the case of the FCC STwGBs. While the shape and cusp location match well, both appear to differ by some multiplicative constant.

For the (111) case, no relaxation occurs because, as expected, the planar model attains its minimum for $\theta = 0^\circ$. For the (100) case we observe relaxation occurring near $\theta = 0^\circ, 90^\circ$. As with STGBs, relaxation using $\{111\}$ facets in FCC materials is necessary to correctly recover the value of 0 for uniform

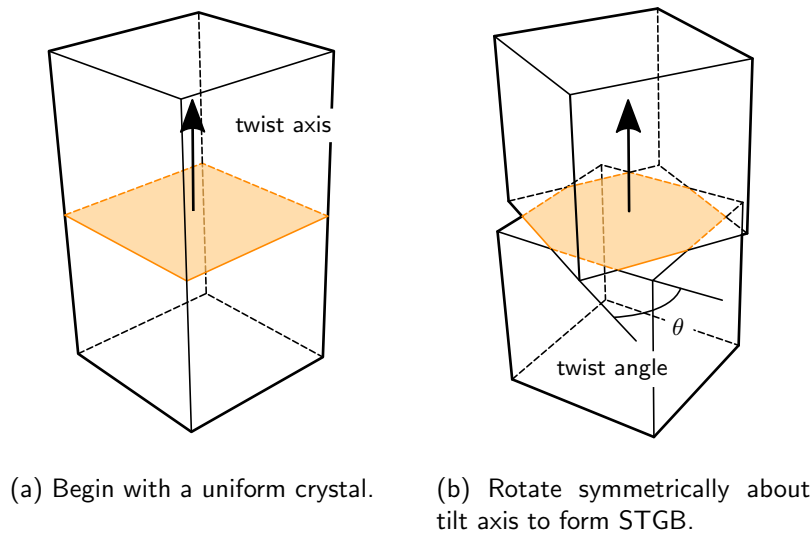


Figure 4.7: Geometry of asymmetric tilt grain boundaries.

crystals. For (115)(111) and (221)(001) asymmetric twist we observe very good agreement between the molecular dynamics data and the results of the model. The improvement on the (115)(111) case by relaxation is negligible but unnecessary given the high correlation of the unrelaxed results. For (221)(001) the planar model overpredicts the value of the energy at the cusps for $\theta = 0^\circ, 90^\circ$; however, the relaxed model corrects the energy value to give an almost exact matching of the cusp magnitude. For the remaining two ATwGBs we observe more chaotic energy data in the MD results as well as the relaxed and unrelaxed model. For (114)(011) ATwGB we see a marked difference between the behavior of the MD data for copper vs for gold, indicating that for this type of interface, grain boundary energy may not be dominated by geometry. We see a considerable improvement on the planar model at the energy cusps for $\theta = 0^\circ, 180^\circ$. The model already predicted cusps at those locations, but relaxation corrects the magnitudes for an almost exact match. For (557)(113) there is a slight improvement in the energy for the cusps at $\theta = 0^\circ, 180^\circ$, though the energy match is not exact. It is interesting to note that small energy reductions by relaxation occur through the range of θ for both (114)(011) and (557)(113) TwGBs. An examination of the stereographic energy surface visualizations for those values do not yield any interesting insight into their morphology, but we observe that continuous, slight relaxation seems to correspond to more “chaotic” boundaries that invariably have more disordered morphology. This is

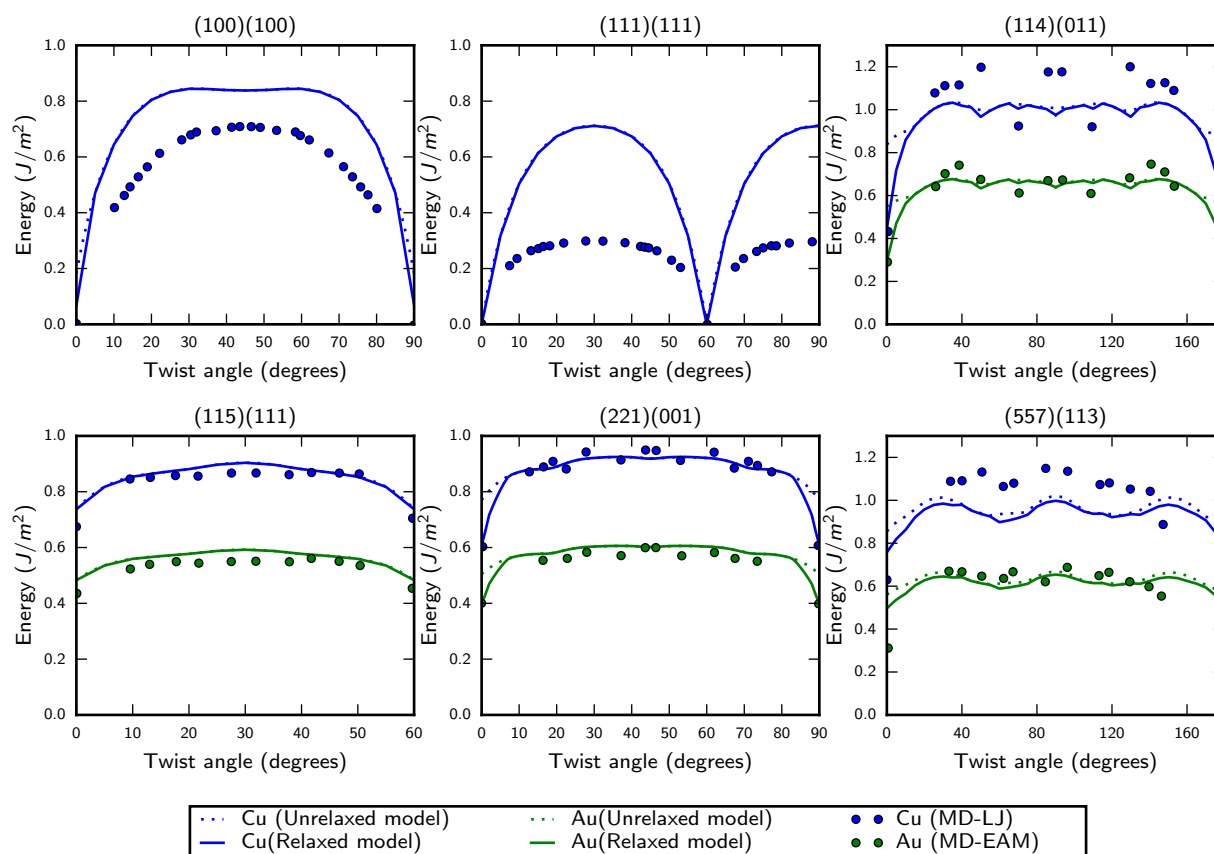


Figure 4.8: FCC TwGB results of the covariance model (relaxed and unrelaxed) for Copper and Gold, compared with MD results using EAM (for gold) and LJ (for copper). The boundary planes (constant for all twist angles) are indicated by the graph labels. MD results for symmetric twist from [42], asymmetric twist from [43].

a trend that we will observe in the following BCC twist cases as well.

A broader range of BCC twist grain boundary data are available, giving us a greater dataset for validation. For symmetric twist only data for alpha-phase iron was found, so we include only the iron results. For asymmetric twist we compare against both alpha-phase iron and molybdenum.

The results for BCC symmetric twist grain boundaries are plotted in Figure 4.9. As we expect for (100) symmetric twist relaxation occurs near the end cusps, as a result of the fact that (100) boundaries for uniform crystals in BCC require convexification with (110) boundaries to reduce the energy to zero. For the remainder of this region the match is close, and coincident with the planar model. No relaxation

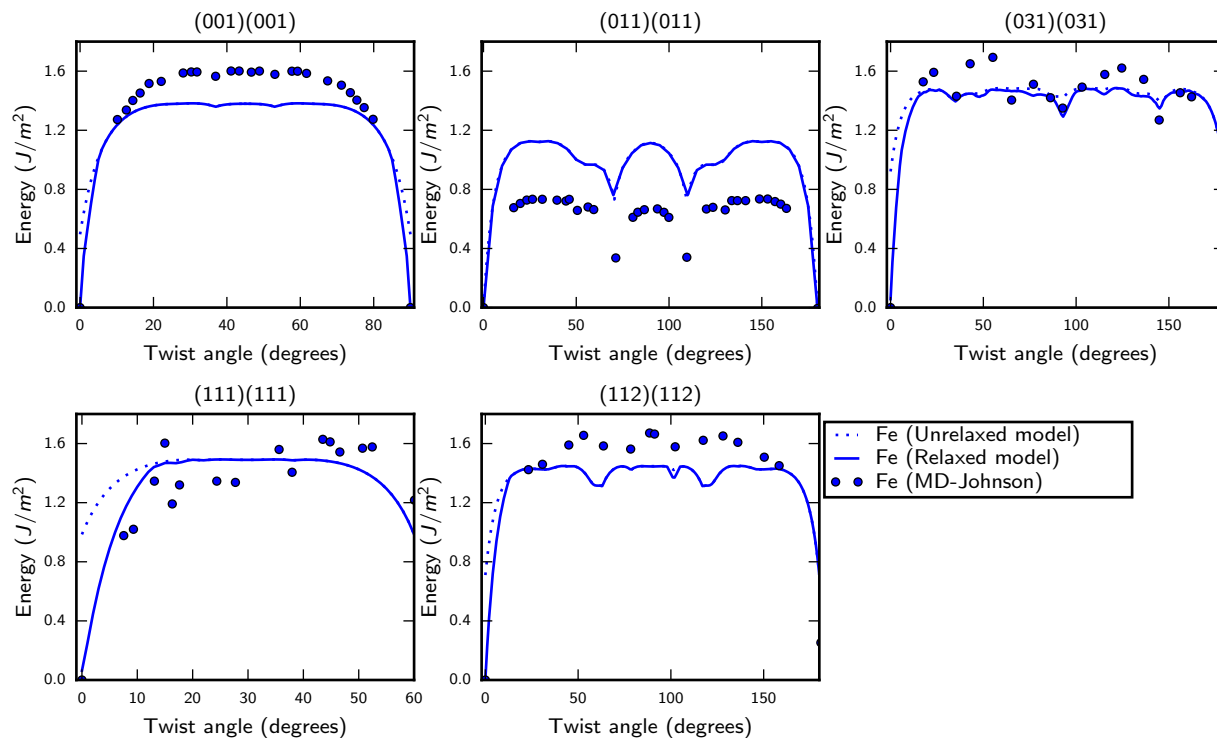


Figure 4.9: BCC StwGB results of the covariance model (relaxed and unrelaxed) for α -Iron, compared with MD results using a Johnson potential. MD data from [50, 51].

occurs for the (110) STwGB set of boundaries; the planar model recovers $\gamma = 0$ at the end cusps and apparently the remainder of the interfaces are planar. As in the previous work we note that the shape of the energy matches very closely, differing only by a multiplicative constant. For (031)(031) symmetric twist, the relaxation model correctly adjusts the cusp at $\theta = 0^\circ$ to zero. The resultant matching of both end cusps is very good. We see a fairly chaotic pattern in both the MD and the model data, with the relaxed energy diverging slightly from the unrelaxed at multiple points. The match of the general trend is good, and neither MD nor the model predict the existence of a well-defined cusp that the other does not. For (111)(111) symmetric twist we find again that the model correctly adjusts the $\theta = 0^\circ$ to zero as expected; no other relaxation occurs, and the matching of the energy trends and cusp magnitudes is very close. Finally, as with most of the other cases, we observe $\theta = 0^\circ$ cusp correction to zero for (112)(112).

The results for BCC asymmetric twist grain boundaries are plotted in Figure 4.10. For (114)(011)

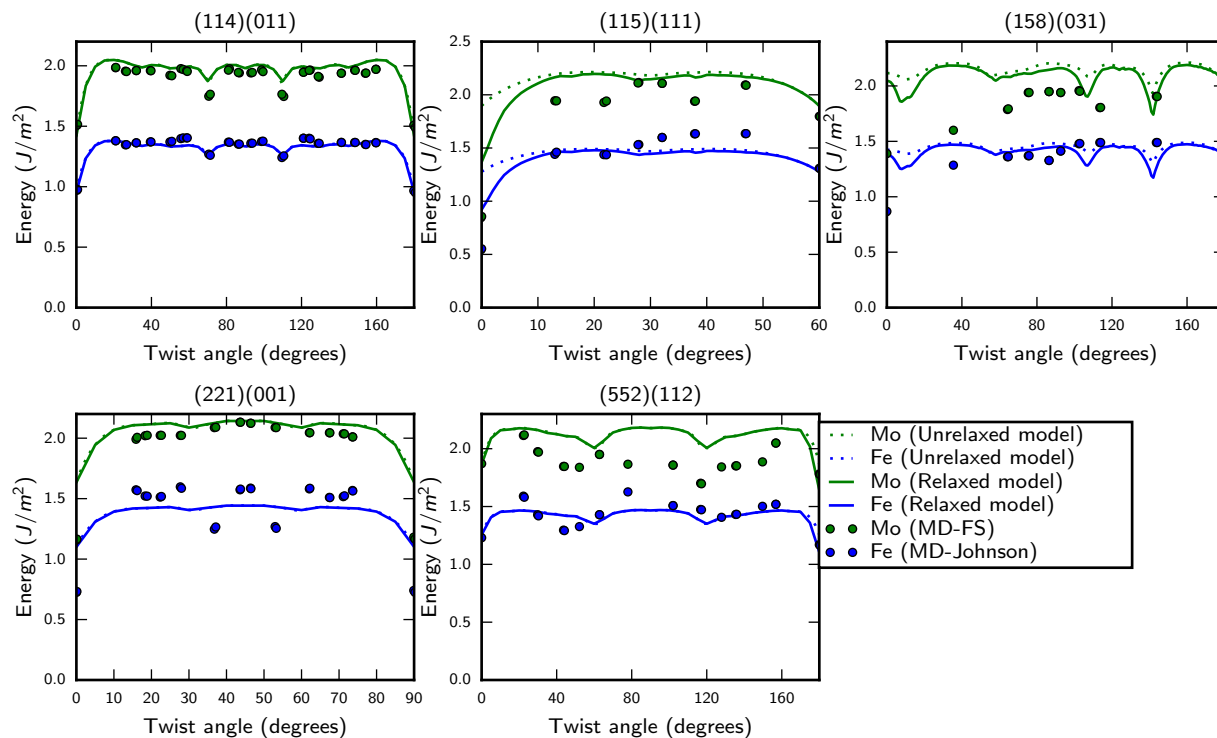


Figure 4.10: BCC ATwGB results of the covariance model (relaxed and unrelaxed) for Molybdenum and α -Iron, compared with MD results using a Finnis-Sinclair (FS) potential for Mo and a Johnson potential for Fe. MD results from [51].

twist almost an exact match exists between the planar model and the MD data. No relaxation is observed, (or needed). For (115)(111) twist we observe a slight reduction of energy by relaxation for $\theta < 50^\circ$, and a significant reduction at the cusp $\theta = 0^\circ$. The cusp matching is not precise, but the relaxation clearly improves the planar results considerably. For (158)(031) we observe a significantly chaotic pattern in both MD data and the model. The relaxation behavior is unique for this set of data in that additional minima are formed by the creation of relaxation structures. Additionally we do not observe any correction of the values at the end points, although neither endpoint appears to correspond to a cusp in either the model or MD results. For the (221)(001) case we observe no relaxation and, interestingly, the value of the energy at the cusps does not change either. Good agreement is observed for molybdenum in particular. An energy structure in the MD data is observed for iron that differs from molybdenum. As with some of the the low-symmetry FCC cases, this difference may indicate a

departure from the interface energy behavior from dependence on geometry, at least for this specific type of grain boundary. Finally, for the (552)(112) case we observe majority coincidence of the planar model with the relaxed model. However, relaxation occurs near $\theta = 180^\circ$ that improves the matching of the energy cusps. Otherwise we find good agreement between the model and the MD results.

In conclusion for the discussion of twist grain boundaries, we believe that the combination of the covariance model with relaxation produces a wide range of results that match very well with molecular dynamics data. Some outlying cases exist; however, we find almost universal agreement of the predicted cusp location. Because the model was designed primarily as a means of locating cusps, this serves as validation within the mission space of the model. Further, the primary discrepancies between the model and the MD data are generally cases where the results are still almost identical up to a multiplicative constant. Closer matching could be obtained by adjusting the model parameters for those sets specifically, but a departure from a consistent set of parameters would compromise the model's predictive ability. A number of explanations may be offered for these differences ranging from the inability of the model to access certain relaxation mechanisms, to an inaccuracy of the MD potentials [51].

4.3.3 Asymmetric tilt grain boundaries

The last set of grain boundaries that we consider are the set of asymmetric tilt grain boundaries (ATGBs). The space of possible ATGBs is very large, encompassing almost any type of grain boundary. In this work we restrict our use of the ATGB nomenclature to a particular type of asymmetric tilt grain boundary.

ATGBs are defined by the way in which they are constructed. Figure 4.11 illustrates the procedure for generating an ATGB from a uniform crystal. The uniform crystal boundary is transformed to a symmetric tilt grain boundary by symmetric rotation about an in-plane axis. Then a different in-plane axis is selected and the interface is rotated with the orientation relationship of the crystals remaining fixed. (Alternatively, the top and bottom crystals are tilted antisymmetrically about the in-plane axis.) The axis about which the interface is rotated is referred to as the inclination axis, and the angle of rotation ϕ as the inclination angle. In this work we refer to a class of ATGBs using the following system: a $\{lmn\}\langle pqr \rangle$ set of ATGBs is one for which ϕ corresponds to inclination of the interface about a mutual

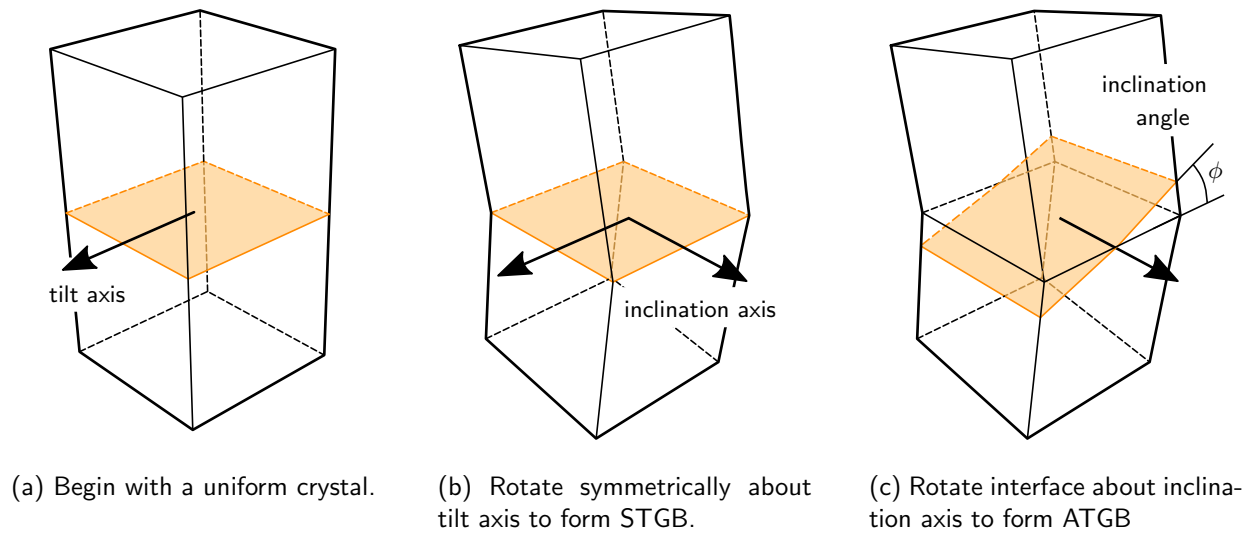


Figure 4.11: Geometry of asymmetric tilt grain boundaries

$\langle pqr \rangle$ axis, and $\phi = 0^\circ$ corresponds to a $\{lmn\}$ STGB. One major disadvantage to this categorization system is that ATGBs can sometimes be constructed more than one way, resulting in a nonunique notation.

ATGBs are of interest because they are relatively simple and have a high degree of symmetry, yet tend to have complex morphology. ATGBs are ideal for observing the behavior of the relaxation model to determine its ability to predict not only the relaxed energy but the corresponding morphology as well. In this work we study three different ATGBs. As before, our choice of GB cases is driven by the availability of published experimental and molecular dynamics data. For the first two cases, $\{111\}\langle 110 \rangle$ and $\{111\}\langle 112 \rangle$, we compare energetic data with results from MD and compare the morphological prediction of the relaxed model with experimental observation. For the final case, $\{113\}\langle 110 \rangle$, we examine the effect of changing the dimensionless temperature σ to determine its effect on faceting behavior and the relationship to thermalization in experimental observation.

$\{111\}\langle 110 \rangle$ ATGB

The energetic results for the $\{111\}\langle 110 \rangle$ ATGB for various FCC materials are shown in Figure 4.12. Comparison is made of copper and aluminum data with MD results, and the relaxed results for gold

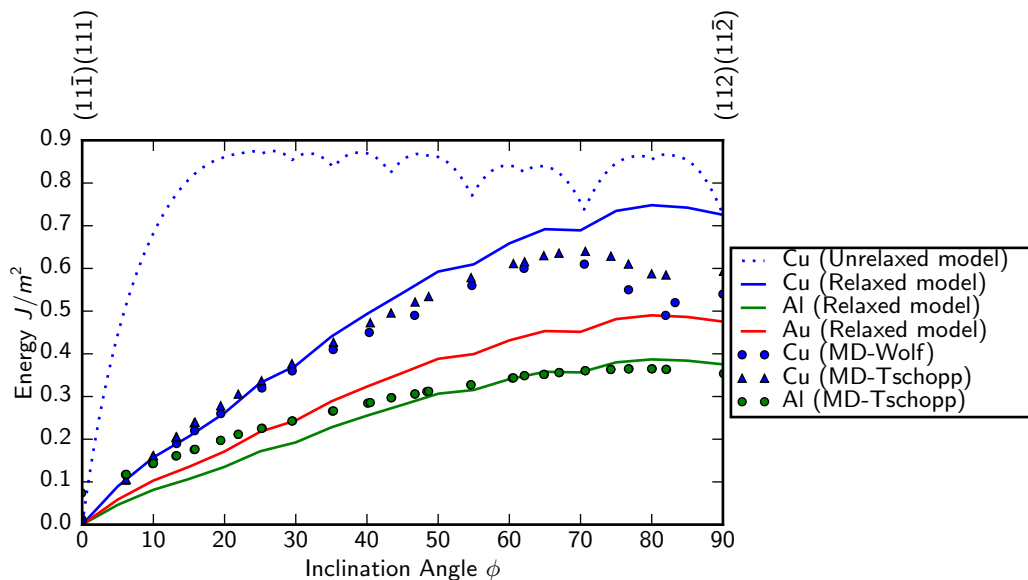


Figure 4.12: MD data for Cu from [45,47]. MD data for Al from [47].

are included as well. As with the other tests the unrelaxed results are plotted as a hashed line with the relaxed results plotted with a solid line. (Unrelaxed results for are included for copper only; including it for gold and aluminum obfuscates the visibility of the other plots.) We observe a major difference between the unrelaxed and the relaxed results. Order 2 faceting occurs for all points $0^\circ < \phi < 90^\circ$, where facets are created corresponding to the 0° and 90° orientations. The energy appears to match closely, and the resultant 2-facet pattern is consistent with observation of the MD results.

In the original paper containing the MD data, Wolf proposed a scheme for approximating the energy of the faceted interface given the energy per unit area of the two individual facets [45]. Here we note that this formula is recoverable as a special case of the relaxation model. Let $\gamma(\phi)$ be the planar energy as a function of inclination angle, and let $\phi_1 = 0^\circ$ and $\phi_2 = 90^\circ$ correspond to the optimal facet orientations. Then the optimal normal vectors are

$$\mathbf{n}_1(\phi) = \begin{bmatrix} 0 \\ \sin(\phi_1 - \phi) \\ \cos(\phi_1 - \phi) \end{bmatrix} = \begin{bmatrix} 0 \\ -\sin(\phi) \\ \cos(\phi) \end{bmatrix} \quad \mathbf{n}_2(\phi) = \begin{bmatrix} 0 \\ \sin(\phi_2 - \phi) \\ \cos(\phi_2 - \phi) \end{bmatrix} = \begin{bmatrix} 0 \\ \cos(\phi) \\ \sin(\phi) \end{bmatrix}. \quad (4.29)$$

We use the constraint of the optimization problem to obtain λ_1, λ_2 :

$$\begin{bmatrix} -\sin(\phi) & \cos(\phi) \\ \cos(\phi) & \sin(\phi) \end{bmatrix} \begin{bmatrix} \lambda_1 \\ \lambda_2 \end{bmatrix} = \begin{bmatrix} 0 \\ 1 \end{bmatrix} \implies \begin{bmatrix} \lambda_1 \\ \lambda_2 \end{bmatrix} = \begin{bmatrix} \cos(\phi) \\ \sin(\phi) \end{bmatrix}. \quad (4.30)$$

Then the relaxed energy is

$$\gamma(\phi) = \cos(\phi) \gamma(\phi_1) + \sin(\phi) \gamma(\phi_2), \quad (4.31)$$

which corresponds to Wolf's approximation where $\gamma_1 = \gamma(\phi_1)$, $\gamma_2 = \gamma(\phi_2)$.

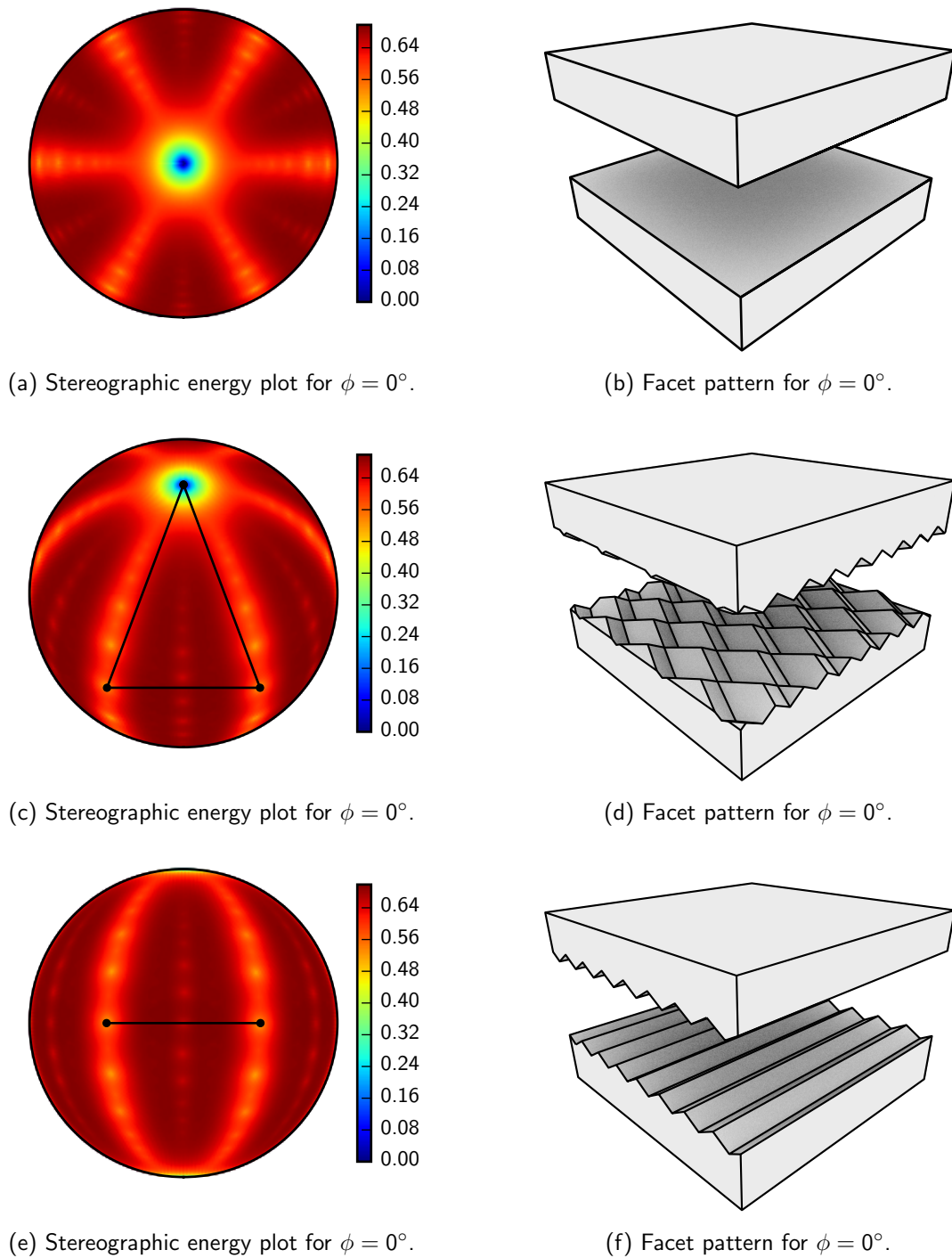
$\{111\}\langle 112 \rangle$ ATGB

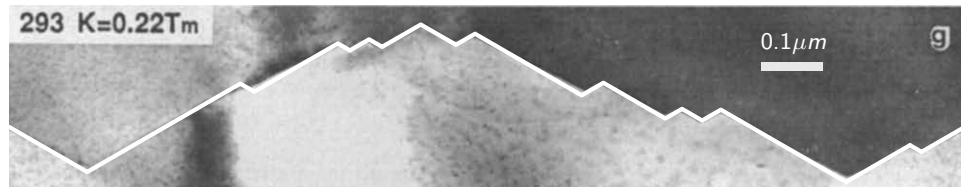
Next we consider a similar set of ATGB data. These grain boundaries are obtained by beginning with the same STGB as in the previous section, but inclining the interface about the mutual $\langle 112 \rangle$ axis instead of the $\langle 110 \rangle$ axis. This family of ATGBs demonstrates a wide range of morphological behavior, varying from planar in the STGB case to 3-faceted for $0^\circ < \phi < 90^\circ$ to 2-faceted for 90° . The evolution of the F3 plot and the corresponding morphology is given in Figure 4.13.

One particularly interesting thing to note about the evolution of this morphology is that the 2-facet direction for $\phi = 90^\circ$ is *orthogonal* to the inclination axis. As a result, an observer looking at a 2D cross section with the inclination axis as a normal will not be able to detect the 2-facets. However, the case of $\phi = 90^\circ$ is interesting because it lies in the intersection of $\{111\}\langle 112 \rangle$ ATGBs *and* $\{112\}\langle 111 \rangle$ ATGBs.

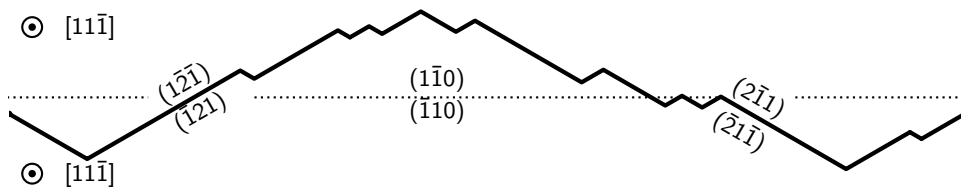
$\{112\}\langle 111 \rangle$ ATGBs have been studied experimentally. The relaxation model gives the precise orientation of the facets formed for the 90° case, and can be used to construct a faceting pattern. In Figure 4.14, experimental observations of faceting in this interface configuration are compared with results from the model by overlaying the observed interface with a reconstructed one using predicted faceting slopes. We observe that the matching is almost exact.

We note that the facets have the length scale of approximately $100nm$. As stated earlier, the length scale may be determined in some cases by the energy of edge defects (such as dislocations), although in this case edge effects are likely negligible. The more likely explanation is that the energetic barrier for

Figure 4.13: Evolution of the facet microstructure for ϕ varying from 0° to 90° .



(a) Faceting in Au [116, Figure 7]. Overlay is a trace of the facet pattern using relaxation method-predicted facets.



(b) Average ("prescribed") boundary plane and the predicted facet planes.

Figure 4.14: Comparison of experimentally observed faceting in a $\{111\}\langle 112 \rangle$ ATGB with the relaxation method's predicted facet pattern.

interfacial migration and restructuring is prohibitively high at this scale. Regardless of the length scale, the matched optimal interface orientations provides strong verification for the relaxation method.

Finally, we compare the computed relaxed energy of the ATGB with that determined using molecular dynamics in Figure 4.15. We observe that the energy match is consistent, although the molecular dynamics data increases sharply as $\phi \rightarrow 90^\circ$. Because the MD results for $\phi = 90^\circ$ did not indicate the presence of 2-faceting, one possible reason for the difference may be that the MD results were high because the system did not relax. Nevertheless, we conclude that the experimental faceting matches well with the predicted faceting and that the molecular dynamics data matches well with the predicted relaxed energy.

$\{113\}\langle 110 \rangle$ ATGB

Here we investigate the effect of thermalization on faceting configurations. We compare with results from Hsieh and Balluffi who examined the results of temperature on faceted interfaces, and concluded that a de-faceting transition can take place as the result of elevated temperature [116]. The thermal regularization in the covariance model admits a convenient way of examining the effect of elevated

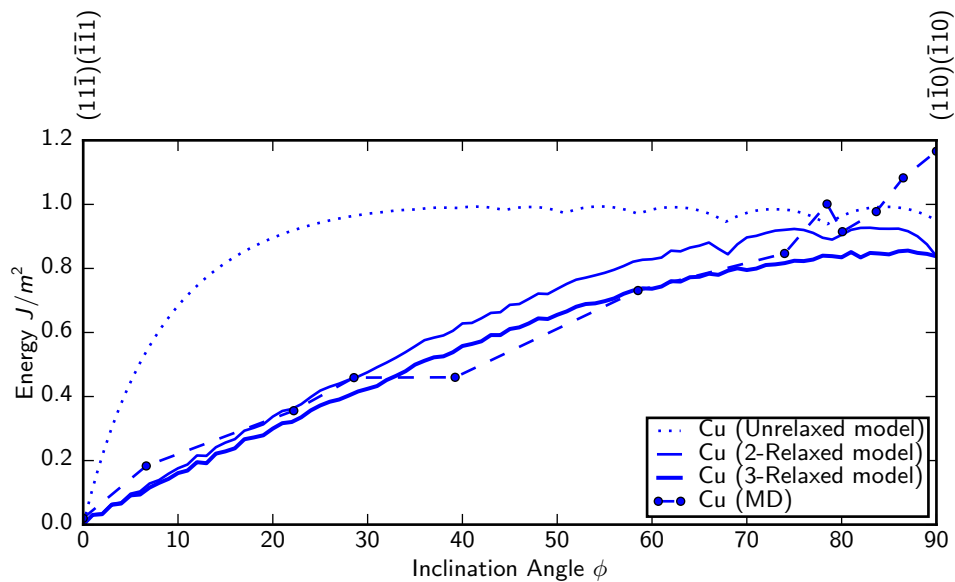


Figure 4.15: Model prediction of energy for $\{111\}\langle 112 \rangle$ ATGBs in Copper. Results are presented for the planar model (dash), relaxed using 2-facets (thin), relaxed using 3-facets (thick). MD results computed with an EAM potential are included for comparison (dot-dash). MD data from [44].

temperature on grain boundaries. If a quadratic potential is used for the atomic embedding function w , then the parameter $\sigma = k_B T/w_0$ models the dimensionless temperature of the interface. We consider the effect of thermalization on the $\{113\}\langle 110 \rangle$ asymmetric tilt grain boundary in Al, where the inclination angle is 25.24° so that the mean (“prescribed”) upper and lower boundary planes are $\{002\}$ and $\{667\}$.

For interfaces of this type we find that there are no facet patterns of order greater than two. Thus we restrict to two-dimensional faceting, which speeds up the analysis. In Figure 4.16 we plot the energy for several values of σ and all rotations of the interface about the shared $[110]$ axis. The thin blue curve corresponds to the planar energy for the ATGB as a function of interface orientation, where the value at $\theta = 0^\circ$ (the “north” end of the plot) is the energy for the planar interface without relaxation.

The thick blue line corresponds to the relaxed energy *for each rotation of the interface*. As expected, we recover the maximal convex energy (in the sense of crystalline integrands [93]), that is, the convexification γ_C . In general we find that computation of γ_C is infeasible for the full range of $\mathbf{n} \in \mathcal{S}_2$; however, it is possible here by restriction to $\mathbf{n} \in \mathcal{S}_1 \subset \mathcal{S}_2$.

Also of interest (albeit extraneous to the observation of faceting structure) is the *crystal of the energy*,

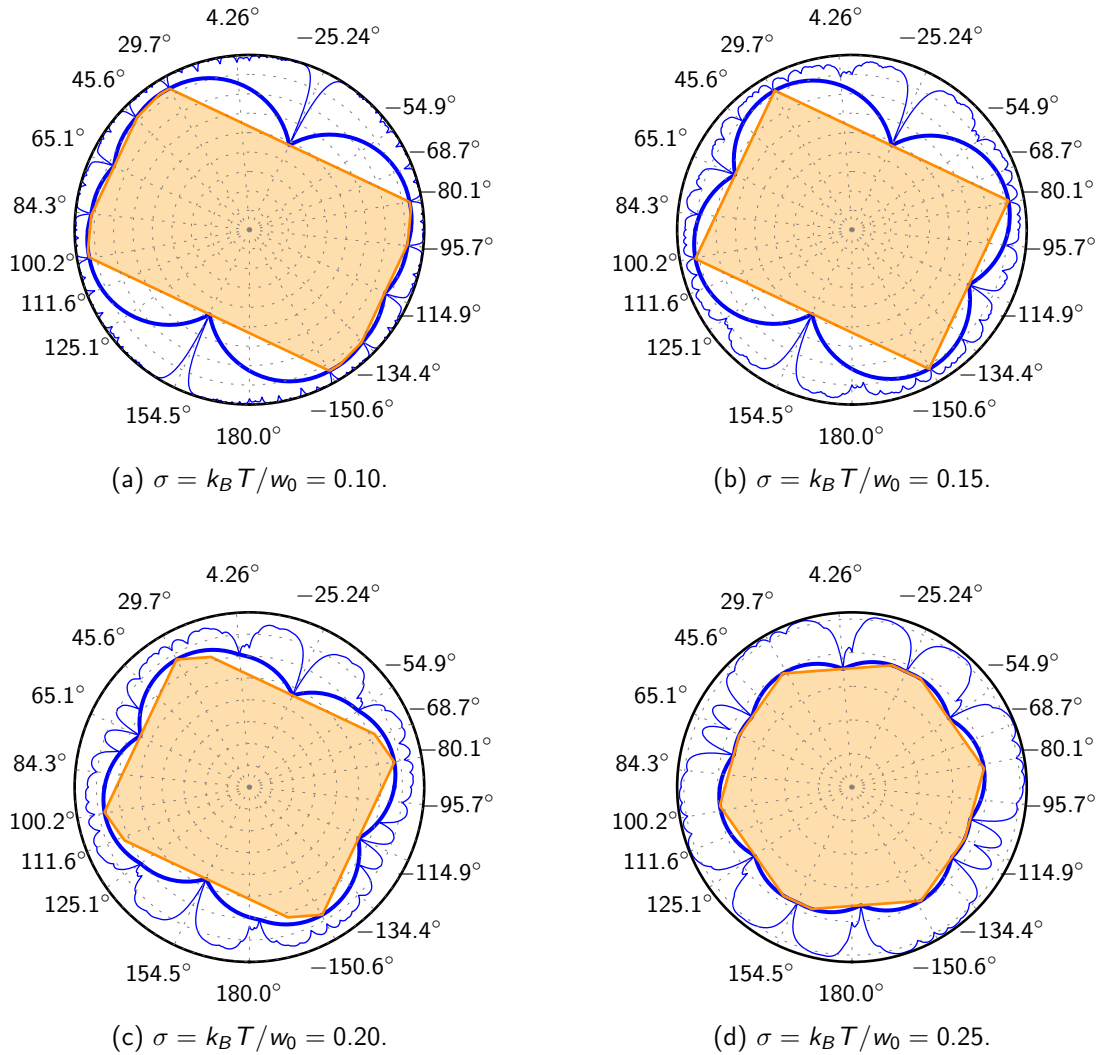


Figure 4.16: Predicted evolution of the planar energy surface (thin line) and the relaxed energy surface (thick line) with the temperature σ ; shaded region is Wulff shape.

or the *Wulff shape*, shown as the shaded region. The Wulff shape is a construction corresponding to the energy-minimizing shape of an inclusion given a specified volume; that is, the optimal shape that one crystal would take if it is an inclusion in the other. Here the boundary of the Wulff shape is computed by solving

$$\gamma_c(\mathbf{n}) = \inf_{\bar{\mathbf{n}} \in S_1} \frac{w(\bar{\mathbf{n}})}{\bar{\mathbf{n}} \cdot \mathbf{n}}. \quad (4.32)$$

Clearly the Wulff shape undergoes significant change as the temperature increases. We see that for higher temperatures the structure becomes more amorphous, whereas lower temperatures produce a crystal with sharper edges.

We observe that as the temperature increases the minimizing facet pattern changes. For $\sigma = 0.1, 0.15$ the optimal facets form at $\theta = 4.26^\circ, -25.24^\circ$ corresponding to interfaces with $(001)(6\bar{6}7)$ and $(1\bar{1}3)(\bar{1}13)$ boundary planes, respectively. In Figure 4.17a we observe that this faceting construction corresponds very well to the observed morphology. On the other hand, for $\sigma = 0.2, 0.25$ the $\{113\}$ STGB boundary plane facets remain, but the other facet plane is the incoherent $\sim (1\bar{1}19) \sim (37\bar{3}7\bar{5}0)$ boundary. In Figure 4.17b we observe that the high temperature faceting pattern is also observed experimentally.

We note the following observations: 1) the faceting transition behavior occurs independently of the value of E_0 , which acts as a scaling constant and does not affect the convexification; 2) material dependence can be introduced via the w_0 parameter, the atomic embedding energy constant. As a result we expect that a faceting phase transition of this type will take place in all FCC materials, but the transition temperature for different materials will differ for different values of w_0 .

The lengthscale of the facets here is approximately an order of magnitude smaller than those in the previous FCC ATGB case. As before, the edge energies are likely too small to be the factor determining the lengthscale. We may speculate that the smaller lengthscale is the result of the higher temperature, allowing the reconfiguration of the interface to become accessible. Causes for the resultant lengthscale notwithstanding, the facet orientation provides strong validation for the use of thermalization with the relaxed covariance model.

4.4 Conclusion

The purpose of this work was twofold: first, to review and reformulate the theory of relaxation for surfaces in such a way as to use an existing planar interface energy model to predict relaxed energy and morphology; second, to use the relaxation framework with the covariance model as developed in previous work to validate the model by application to a wide range of existing computational and

Runnels and Michael Ortiz both acknowledge support from the NNSA's High Energy Density Laboratory Plasmas program under award number DE-NA0001805. Irene Beyerlein would like to acknowledge support by a Laboratory Directed Research and Development program, award number 20140348ER.

Chapter 5

Conclusions and Future Work

5.1 Summary

The aim of this work has been to present a novel approach for modeling interface energy by formulating models for predicting energy and morphology. In this work the main application has been towards grain boundaries; however the approach does not exclude an extension to multi-phase interfaces.

In Chapter 2 we motivated the need for a new grain boundary energy model by surveying the broad spectrum of existing models. Current approaches include molecular dynamics, dislocation-based models, geometrical constructions, and MD-informed interpolative models. In our search through the literature, we found that the construction of a model that is rapidly evaluable, general (i.e., able to find cusp locations), and predictive (i.e., minimal number of adjustable parameters) remains an open objective. Regarding the relaxation portion of the work, we surveyed the literature in mathematics and materials science regarding the method of convexification by faceting. We found that the observation of relaxation by faceting is made independently by several authors but, because a sufficiently general model is not available, the construction has yet to be applied in a predictive analysis.

In Chapter 3 we formulated the planar covariance model for interface energy. The fundamental definition upon which the model is constructed is the *density measure*, ϱ , a functional on a subset of the spatial domain that return's the domain's occupancy. We showed using an argument from statistical thermodynamics that we can account for thermalization of the density measure while simultaneously effecting a numerical regularization. The crux of the first part of the thesis is the definition of *covariance*,

a geometric measure of atomic coincidence. Covariance was defined for all possible interface orientations, and because the thermalized density functions are expressible in Fourier series form, an expression for covariance can be found in closed-form, resulting in a computationally efficient formulation. The covariance energy model was constructed as a linear function of covariance, introducing an additional material parameter, resulting in three material parameters total. To validate the covariance model, we used it to evaluate the energy for 19 separate classes of grain boundaries including symmetric/asymmetric tilt/twist configurations for copper, gold, molybdenum, and α -iron, using a consistent set of parameters for each material. We compared the results with 45 sets of MD data for the same materials with multiple potentials and demonstrate that there is very strong agreement.

In Chapter 4 we investigated whether the frequently-observed faceting patterns in grain boundaries (and interfaces) can be explained in terms of a planar energy model by nonconvexity, and that facet patterns arise to minimize the energy. This observation is not new; equivalent statements of the same idea have been made in both mathematics and materials science literature. However, the statements are purely observational, due to an inability to compute energy for strictly planar interfaces. In this work we formulated the variational interface energy problem, present the convexification relaxation both in the graph and the unit sphere descriptions of interface configurations, and show that they are equivalent. We then presented the method as an algorithm for computing relaxed energy and morphology. This method was then applied using the planar covariance model developed in the previous chapter. We applied the relaxation method to all of the grain boundary configurations in the previous section, and showed that the results were significantly improved. In addition, we applied the method to a set of asymmetric tilt grain boundaries that are known to exhibit faceting. We showed that the relaxed model predicts the facet pattern precisely and, for those for which the data is available, gives a good match with MD energy data. An additional test included examining the dependence of faceting configurations on temperature. We showed that by adjusting the nondimensional temperature in the covariance model, a distinct transition occurred in the facet pattern, matching the experimentally-observed effect.

The combination of the convexification algorithm with the planar covariance model has been demonstrated to predict anisotropic grain boundary energy and morphology with a high degree of success, and

to be efficient enough for use in a continuum-level simulation.

5.2 Future work

The model as presented, though shown to give accurate results, is still fundamentally a geometric construction. As such, it requires continual testing to determine what the limits of its application are; thus the immediate task is to continue to test the model for additional grain boundary data, possibly requiring the generation of additional data from experiment or molecular dynamics for comparison.

The model has been tested exclusively with grain boundaries thus far, but extending it towards general interfaces would be beneficial in characterizing bimetallic interfaces. (However, it remains to be seen if a geometric construction is sufficient for characterizing interfaces of this complexity.) Additionally, other challenges are immediately apparent, such as determining the correct definition of the ground state covariance c_0 .

Appendix A

Positivity of Fourier Coefficients for FCC and BCC Lattices

Here we validate the positivity of the Fourier coefficients for the Fourier expansions of FCC and BCC crystals with unit cells described in Table 3.1.

For BCC lattices the Fourier coefficients are given by

$$\varrho_{\mathbf{n}}^{bcc} = \frac{1}{|E|} \sum_{\mathbf{n} \in I_E} \theta_E(\mathbf{r}(\mathbf{n})) e^{-i\mathbf{k}(\mathbf{n}) \cdot \mathbf{r}(\mathbf{n})} \quad (\text{A.1})$$

$$= \frac{1}{\alpha_1 \alpha_2 \alpha_3} \left[1 + \frac{1}{8} \left(e^{\pm i\pi n_1 \pm i\pi n_2 \pm i\pi n_3} \right) \right] \quad (\text{A.2})$$

$$= \frac{1}{\alpha_1 \alpha_2 \alpha_3} \left[1 + \frac{1}{8} \left(\text{Re}(e^{\pm i\pi n_1}) \times 2 \text{Re}(e^{\pm i\pi n_2}) \times 2 \text{Re}(e^{\pm i\pi n_3}) \right) \right] \quad (\text{A.3})$$

$$= \frac{1}{\alpha_1 \alpha_2 \alpha_3} [1 + \cos(n_1 \pi) \cos(n_2 \pi) \cos(n_3 \pi)] \quad (\text{A.4})$$

$$= \frac{1}{\alpha_1 \alpha_2 \alpha_3} [1 + (-1)^{n_1 + n_2 + n_3}] \geq 0, \quad (\text{A.5})$$

demonstrating the coefficient positivity for this choice of unit cell.

For FCC lattices the Fourier coefficients are given by

$$\varrho_{\mathbf{n}}^{fcc} = \frac{1}{|E|} \sum_{\mathbf{n} \in I_E} \theta_E(\mathbf{r}(\mathbf{n})) e^{-i\mathbf{k}(\mathbf{n}) \cdot \mathbf{r}(\mathbf{n})} \quad (\text{A.6})$$

$$= \frac{1}{\alpha_1 \alpha_2 \alpha_3} \left[1 + \frac{1}{4} \left(e^{\pm i\pi n_2 \pm i\pi n_3} + e^{\pm i\pi n_3 \pm i\pi n_1} + e^{\pm i\pi n_1 \pm i\pi n_2} \right) \right] \quad (\text{A.7})$$

$$= \frac{1}{\alpha_1 \alpha_2 \alpha_3} [1 + \cos(n_2 \pi) \cos(n_3 \pi) + \cos(n_3 \pi) \cos(n_1 \pi) + \cos(n_1 \pi) \cos(n_2 \pi)] \quad (\text{A.8})$$

$$= \frac{1}{\alpha_1 \alpha_2 \alpha_3} [1 + (-1)^{n_2+n_3} + (-1)^{n_3+n_1} + (-1)^{n_1+n_2}]. \quad (\text{A.9})$$

It is obvious that the expression in the brackets cannot be lower than -2 . But for this to be true, $n_2 + n_3, n_3 + n_1, n_1 + n_2$ must all be odd. However, $n_2 + n_3, n_3 + n_1$ both odd implies that n_1 and n_2 are either both even or both odd, either case leading to $n_1 + n_2$ even. Thus we see that the expression is either equal to $1 + 1 + 1 + 1 = 4$ or $1 + 1 - 1 - 1 = 0$, so we see that $\varrho_{\mathbf{n}}^{fcc} \geq 0$, concluding the proof.

We note that the usual FCC lattice structure does not satisfy the positivity constraint. The unit cell has atoms placed at $(\pm\alpha_1/2, \pm\alpha_2, \pm\alpha_3)$ ($\theta = \frac{1}{8}$) and at $(\pm\alpha_1/2, 0, 0), (0, \pm\alpha_2/2, 0), (0, 0, \pm\alpha_3/2)$, ($\theta = \frac{1}{2}$). Then the coefficients are

$$\varrho_{\mathbf{n}}^{fcc} = \frac{1}{|E|} \sum_{\mathbf{n} \in I_E} \theta_E(\mathbf{r}(\mathbf{n})) e^{-i\mathbf{k}(\mathbf{n}) \cdot \mathbf{r}(\mathbf{n})} \quad (\text{A.10})$$

$$= \frac{1}{\alpha_1 \alpha_2 \alpha_3} \left[1 + \frac{1}{8} \left(e^{\pm i\pi n_1 \pm i\pi n_2 \pm i\pi n_3} \right) + \frac{1}{2} \left(e^{\pm i\pi n_1} + e^{\pm i\pi n_2} + e^{\pm i\pi n_3} \right) \right] \quad (\text{A.11})$$

$$= \frac{1}{\alpha_1 \alpha_2 \alpha_3} \left[1 + (-1)^{n_1+n_2+n_3} + \frac{1}{2} \left((-1)^{n_1} + (-1)^{n_2} + (-1)^{n_3} \right) \right]. \quad (\text{A.12})$$

Choosing odd values for n_1, n_2, n_3 produces a value of $-3/2$ in the brackets; as a result this choice of Fourier expansion is not optimal.

Appendix B

Supplementary Validation

In the main part of this work, we use consistent MD results for verification of the model in order to avoid the need to adjust material parameters to accommodate discrepancies between authors. The disadvantage of using consistent results is the possibility that both the model and the MD results are wrong about something. Therefore, in this section we present additional verification and validation examples for the relaxed covariance model by comparing it to i) more modern MD simulations, ii) experimentally measured grain boundary energy, and iii) the Read-Shockley low-angle tilt model.

B.1 Molecular Dynamics

The molecular dynamics results from Wolf for tilt and twist grain boundaries in FCC and BCC metals provide valuable data for validation. However, because of the significant progress made in the field of atomistic simulations, as well as advances in computational resources, it is important to ensure that the model captures behavior of modern GB MD results.

Here we compare against MD results for iron in both FCC and BCC phases using a Finnis-Sinclair potential by Shibuta *et al* [113]. The MD results were computed for 2-3 values of a normalized temperature, T_N . (It is apparent from the MD results that the effect of changing the temperature is very small, consequently we do not adjust the nondimensionalized temperature in our model.)

Material parameters of $E_0 = 2.4 \frac{J}{m^2}, 2.25 \frac{J}{m^2}$, $\sigma/\alpha = 0.175, 0.19$, and $\varepsilon = 0.5, 0.25$ were used for FCC and BCC Iron, respectively.

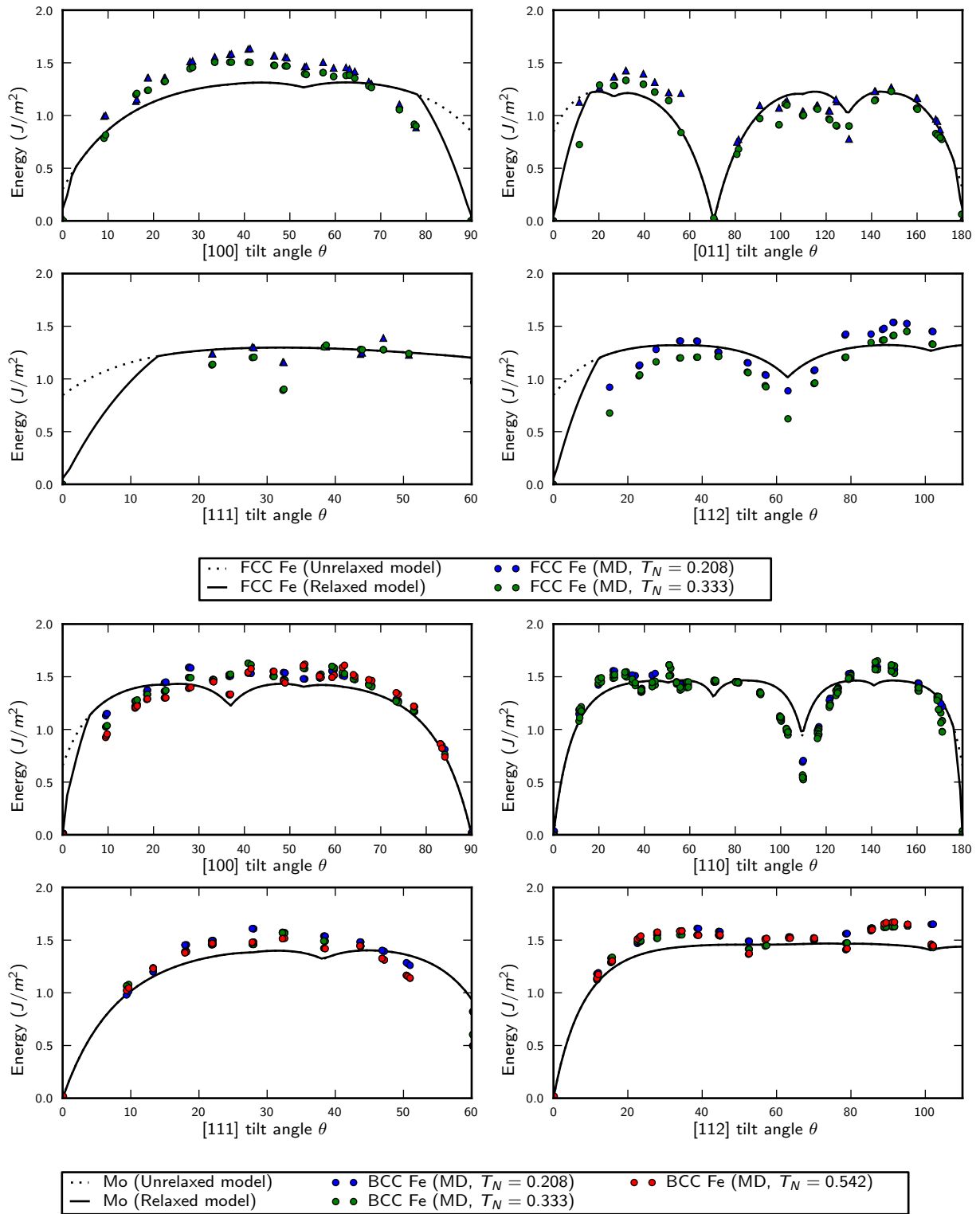


Figure B.1: Model comparison with MD results for FCC and BCC Iron [113].

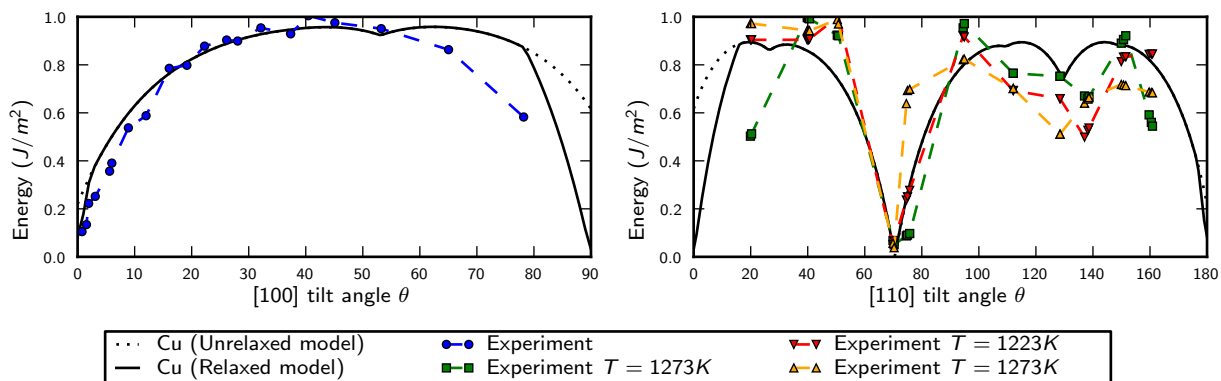


Figure B.2: Comparison of the relaxed covariance model with experimental data for [100] and [110] STGBs in Cu. Experimental data for [100] STGBs from [29], for [110] STGBs from [118]

Figure B.1 includes a comparison of the model results to the MD results. For the FCC case, we see that the match is very close, with the cusps lining up exactly and the large angle tilt values reasonably approximated by the model. Similarly for the BCC case, the locations of the cusps are predicted exactly and the large angle tilt values are matched well; indeed, the modern BCC-Fe results match much more closely than the original ones. In particular, for 110 BCC tilt, a cusp predicted in the original MD but missing in the model at around $\theta \approx 40^\circ$ is also missing in the Shibuta *et al* MD results.

B.2 Experimental Energy Data

Experimental grain boundary anisotropy data provide a useful method for validation of any grain boundary model. We compare the results of the relaxed covariance model with measured grain boundary energy data in Figure B.2. Here a multiplier of $E_0 = 1750K$ is used instead of that used for MD comparison.

It is important to note that the experimental measurements were taken for a very high value of energy. However, apparently, the increased temperature does not significantly affect the general shape of the energy landscape, in accordance with the recent observations that energy depends most strongly on the mismatch of the ideal lattices [117]. We again observe a satisfying match between the relaxed covariance model and the experimental measurements.

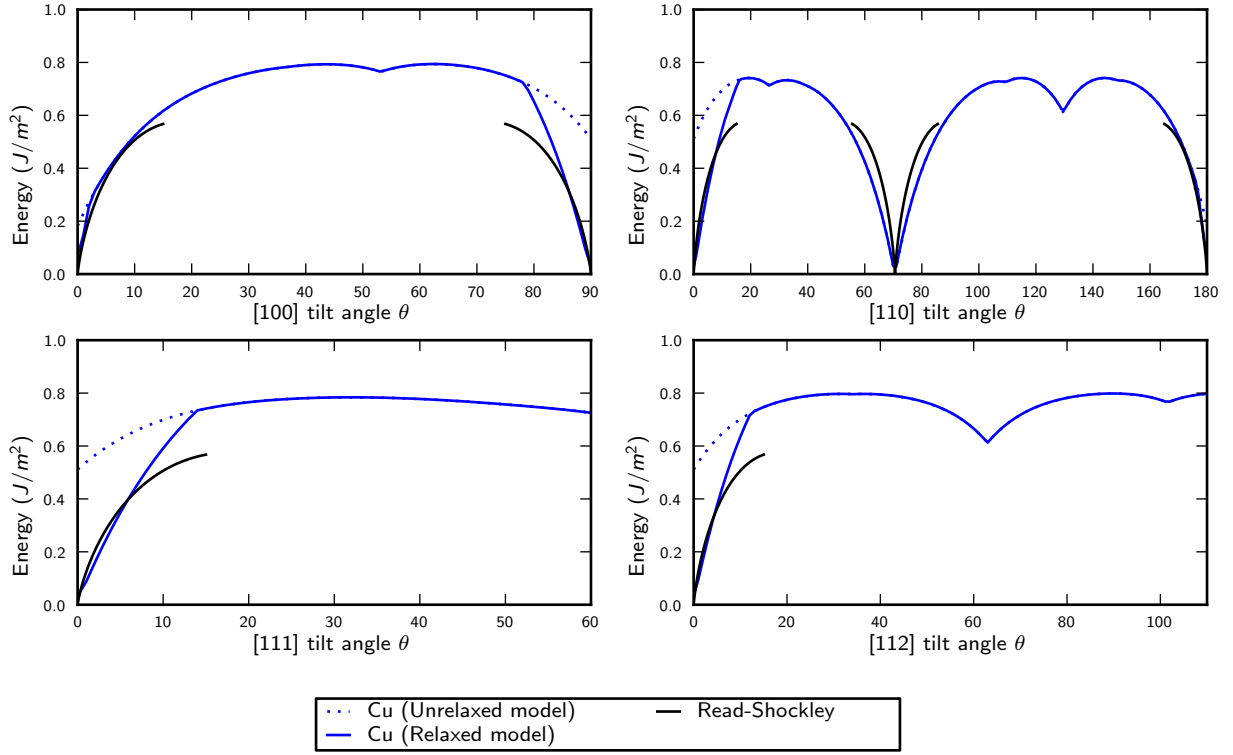


Figure B.3: Model results for FCC Cu compared with the Read-Shockley model

B.3 Read-Shockley Comparison

The Read-Shockley model was the first to capture grain boundary energy by treating interfacial defects as ordered arrays of non-interacting dislocations. By computing the density of the geometrically necessary dislocations, classical dislocation theory was used to determine the energy density [56]. The model for grain boundary energy per unit area as a function of misorientation angle is

$$\gamma = E_0\theta[A - \ln(\theta)], \quad (\text{B.1})$$

where the constants E_0 and A are given by

$$E_0 = \frac{a}{4\pi} \frac{C_{44}}{1 - \sigma_{100}} \sqrt{\frac{2(1 - \sigma_{100})}{\alpha(1 + \alpha(1 - 2\sigma_{100}))}} \quad \sigma_{100} = \frac{C_{12}}{C_{11} + C_{12}} \quad \alpha = \frac{2C_{44}}{C_{11} - C_{12}}$$

$$A = 1 + \ln\left(\frac{a}{2\pi r_0}\right)$$

where C_{11} , C_{12} , C_{44} are the cubic elastic constants, a is the lattice constant, and r_0 is the dislocation core cutoff radius. For copper, $C_{11} = 168.40 \text{ GPa}$, $C_{12} = 121.40 \text{ GPa}$, $C_{75.40}$, $a = 3.597 \text{ \AA}$, and a cutoff radius of $r_0 = a/2$ is used.

The results are plotted in Figure B.3. Because the Read-Shockley model is only valid for small angle tilt, comparisons are only included for the regions $\theta_{TB} - 15^\circ \leq \theta \leq \theta_{TB} + 15^\circ$ where θ_{TB} is the location of the energy cusp. Additionally, it is important to note that the locations of the cusps for the Read-Shockley model were included explicitly; i.e. RS does not predict cusp locations.

In general the relaxed covariance model recovers Read-Shockley. We note some differences in the slope particularly around $\theta = 70^\circ$ for $[110]$ tilt. The RS model begins to diverge from the relaxed covariance model (and MD data) at $|\theta - \theta_{TB}| = 10^\circ$, as expected given the low-angle assumption.

Bibliography

- [1] B. Runnels, I. J. Beyerlein, and M. Ortiz, "A geometry-based model for the energy of grain boundaries," *JMPS (in review)*, 2015.
- [2] B. Runnels, I. J. Beyerlein, S. Conti, and M. Ortiz, "A relaxation method for the energy and morphology of grain boundaries," (*in preparation*), 2015.
- [3] R. Doherty, D. Hughes, F. Humphreys, J. Jonas, D. Jensen, M. Kassner, W. King, T. McNelley, H. McQueen, and A. Rollett, "Current issues in recrystallization: a review," *Materials Science and Engineering: A*, vol. 238, pp. 219–274, Nov. 1997.
- [4] T. Watanabe and S. Tsurekawa, "The control of brittleness and development of desirable mechanical properties in polycrystalline systems by grain boundary engineering," *Acta Materialia*, vol. 47, pp. 4171–4185, Nov. 1999.
- [5] A. Demirel, MC and Kuprat, AP and George, DC and Rollett, "Bridging Simulations and Experiments in Microstructure Evolution," *Physical Review Letters*, vol. 90, p. 016106, Jan. 2003.
- [6] K. Kang, J. Wang, S. J. Zheng, and I. J. Beyerlein, "Minimum energy structures of faceted, incoherent interfaces," *Journal of Applied Physics*, vol. 112, no. 7, p. 73501, 2012.
- [7] I. J. Beyerlein, J. Wang, K. Kang, S. J. Zheng, and N. A. Mara, "Twinability of bimetal interfaces in nanostructured composites," *Materials Research Letters*, vol. 1, pp. 89–95, June 2013.

-
- [8] M. J. Demkowicz and L. Thilly, "Structure, shear resistance and interaction with point defects of interfaces in Cu–Nb nanocomposites synthesized by severe plastic deformation," *Acta Materialia*, vol. 59, pp. 7744–7756, Dec. 2011.
- [9] D. A. Molodov, T. Gorkaya, and G. Gottstein, "Dynamics of grain boundaries under applied mechanical stress," *Journal of Materials Science*, vol. 46, pp. 4318–4326, Jan. 2011.
- [10] D. A. Molodov, T. Gorkaya, and G. Gottstein, "Migration of the $\Sigma 7$ tilt grain boundary in Al under an applied external stress," *Scripta Materialia*, vol. 65, pp. 990–993, Dec. 2011.
- [11] Z. Hong-da, W. Xiao-dan, W. Chong-ming, J. Bo, and X. Hai-long, "Selective SVM Ensembles Based on Modified BPSO," in *2008 IEEE Pacific-Asia Workshop on Computational Intelligence and Industrial Application*, vol. 1, pp. 243–246, IEEE, Dec. 2008.
- [12] J. Taylor and J. Cahn, "Shape accommodation of a rotating embedded crystal via a new variational formulation," *Interfaces and Free Boundaries*, 2007.
- [13] H. Zhang, "Atomistic simulation of sliding of [1010] tilt grain boundaries in Mg," *Journal of Materials Research*, vol. 24, pp. 3446–3453, Jan. 2011.
- [14] Z. Trautt, A. Adland, A. Karma, and Y. Mishin, "Coupled motion of asymmetrical tilt grain boundaries: Molecular dynamics and phase field crystal simulations," *Acta Materialia*, vol. 60, pp. 6528–6546, Nov. 2012.
- [15] J. K. Chen, G. Chen, and W. T. Reynolds, "Interfacial structure and growth mechanisms of lath-shaped precipitates in Ni-45 wt% Cr," *Philosophical Magazine A*, vol. 78, pp. 405–422, Aug. 1998.
- [16] H.-S. Park, K. T. Lorenz, R. M. Cavallo, S. M. Pollaine, S. T. Prisbrey, R. E. Rudd, R. C. Becker, J. V. Bernier, and B. A. Remington, "Viscous Rayleigh-Taylor instability experiments at high pressure and strain rate," *Physical review letters*, vol. 104, p. 135504, Apr. 2010.
-

-
- [17] H.-S. Park, N. Barton, and J. Belof, "Experimental results of tantalum material strength at high pressure and high strain rate," *Proceedings of the Conference of the American Physical Society Topical Group on Shock Compression of Condensed Matter*, 2012.
- [18] K. Bhattacharya, *Microstructure and Martensite: Why it Forms and how it Gives Rise to the Shape-memory Effect*. Oxford Series on Materials Modelling Series, Oxford University Press, Incorporated, 2003.
- [19] L. Wayne, K. Krishnan, S. DiGiacomo, N. Kovvali, P. Peralta, S. Luo, S. Greenfield, D. Byler, D. Paisley, and K. McClellan, "Statistics of weak grain boundaries for spall damage in polycrystalline copper," *Scripta Materialia*, vol. 63, pp. 1065–1068, Nov. 2010.
- [20] M. Xiang, H. Hu, and J. Chen, "Spalling and melting in nanocrystalline Pb under shock loading: Molecular dynamics studies," *Journal of Applied Physics*, vol. 113, p. 144312, Apr. 2013.
- [21] S.-N. Luo, T. Germann, D. L. Tonks, and Q. An, "Shock wave loading and spallation of copper bicrystals with asymmetric Σ_3 $\{110\}$ tilt grain boundaries," *Journal of Applied Physics*, vol. 108, p. 093526, Nov. 2010.
- [22] I. J. Beyerlein, N. A. Mara, J. S. Carpenter, T. Nizolek, W. M. Mook, T. A. Wynn, R. J. McCabe, J. R. Mayeur, K. Kang, S. Zheng, J. Wang, and T. M. Pollock, "Interface-driven microstructure development and ultra high strength of bulk nanostructured Cu-Nb multilayers fabricated by severe plastic deformation," *Journal of Materials Research*, vol. 28, pp. 1799–1812, Apr. 2013.
- [23] S. Zheng, I. J. Beyerlein, J. S. Carpenter, K. Kang, J. Wang, W. Han, and N. A. Mara, "High-strength and thermally stable bulk nanolayered composites due to twin-induced interfaces.," *Nature communications*, vol. 4, p. 1696, Jan. 2013.
- [24] S. Zheng, J. Carpenter, and J. Wang, "An interface facet driven Rayleigh instability in high-aspect-ratio bimetallic nanolayered composites," *Applied Physics Letters*, 2014.
-

-
- [25] D. L. Olmsted, S. M. Foiles, and E. A. Holm, "Survey of computed grain boundary properties in face-centered cubic metals: I. Grain boundary energy," *Acta Materialia*, vol. 57, pp. 3694–3703, Aug. 2009.
- [26] D. L. Olmsted, "A new class of metrics for the macroscopic crystallographic space of grain boundaries," *Acta Materialia*, vol. 57, pp. 2793–2799, May 2009.
- [27] C. Herring, "Structure and properties of solid surfaces," *Journal of Chemical Education*, p. 5, 1954.
- [28] C. Herring, *The physics of powder metallurgy*. McGraw-Hill, 1951.
- [29] N. Gjostein and F. Rhines, "Absolute interfacial energies of [001] tilt and twist grain boundaries in copper," *Acta Metallurgica*, vol. 7, pp. 319–330, May 1959.
- [30] A. Wright and S. Atlas, "Density-functional calculations for grain boundaries in aluminum," *Physical Review B*, vol. 50, pp. 15248–15260, Nov. 1994.
- [31] J. Hartford, "Interface energy and electron structure for Fe/VN," *Physical Review B*, vol. 61, pp. 2221–2229, Jan. 2000.
- [32] P. Suryanarayana, K. Bhattacharya, and M. Ortiz, "Coarse-graining Kohn–Sham Density Functional Theory," *Journal of the Mechanics and Physics of Solids*, vol. 61, pp. 38–60, Jan. 2013.
- [33] I. Steinbach, F. Pezzolla, and B. Nestler, "A phase field concept for multiphase systems," *Physica D: Nonlinear Phenomena*, 1996.
- [34] A. Jaatinen, C. Achim, K. Elder, and T. Ala-Nissila, "Thermodynamics of bcc metals in phase-field-crystal models," *Physical Review E*, vol. 80, p. 031602, Sept. 2009.
- [35] H. Emmerich, H. Löwen, R. Wittkowski, T. Gruhn, G. I. Tóth, G. Tegze, and L. Gránásy, "Phase-field-crystal models for condensed matter dynamics on atomic length and diffusive time scales: an overview," *Advances in Physics*, vol. 61, pp. 665–743, Dec. 2012.
-

-
- [36] K. R. Elder and M. Grant, "Modeling elastic and plastic deformations in non-equilibrium processing using phase field crystals," *arXiv preprint cond-mat/0306681*, pp. 1–20, 2008.
- [37] Y. Mishin, M. Asta, and J. Li, "Atomistic modeling of interfaces and their impact on microstructure and properties," *Acta Materialia*, vol. 58, pp. 1117–1151, Feb. 2010.
- [38] H. J. C. Berendsen, J. R. Grigera, and T. P. Straatsma, "The missing term in effective pair potentials," *The Journal of Physical Chemistry*, vol. 91, pp. 6269–6271, Nov. 1987.
- [39] M. Daw and M. Baskes, "Embedded-atom method: Derivation and application to impurities, surfaces, and other defects in metals," *Physical Review B*, 1984.
- [40] M. S. Daw, S. M. Foiles, and M. I. Baskes, "The embedded-atom method: a review of theory and applications," *Materials Science Reports*, vol. 9, pp. 251–310, Mar. 1993.
- [41] D. Wolf, "Structure-energy correlation for grain boundaries in F.C.C. metals—III. Symmetrical tilt boundaries," *Acta Metallurgica et Materialia*, vol. 38, pp. 781–790, May 1990.
- [42] D. Wolf, "Structure-energy correlation for grain boundaries in F.C.C. metals I: Boundaries on the (111) and (100) planes," *Acta Metallurgica*, vol. 37, pp. 1983–1993, July 1989.
- [43] D. Wolf, "Structure-energy correlation for grain boundaries in f.c.c. metals IV: Asymmetrical twist (general) boundaries," *Acta Metallurgica et Materialia*, vol. 38, pp. 791–798, May 1990.
- [44] C. Schmidt, M. W. Finnis, F. Ernst, and V. Vitek, "Theoretical and experimental investigations of structures and energies of $\Sigma = 3$, [112] tilt grain boundaries in copper," *Philosophical Magazine A*, vol. 77, pp. 1161–1184, May 1998.
- [45] U. Wolf, F. Ernst, T. Muschik, M. W. Finnis, and H. F. Fischmeister, "The influence of grain boundary inclination on the structure and energy of $\sigma = 3$ grain boundaries in copper," *Philosophical Magazine A*, vol. 66, pp. 991–1016, Dec. 1992.
- [46] K. L. Merkle and D. Wolf, "Low-energy configurations of symmetric and asymmetric tilt grain boundaries†," *Philosophical Magazine A*, vol. 65, pp. 513–530, Feb. 1992.
-

-
- [47] M. A. Tschopp and D. L. McDowell, "Structures and energies of Σ 3 asymmetric tilt grain boundaries in copper and aluminium," *Philosophical Magazine*, vol. 87, pp. 3147–3173, Aug. 2007.
- [48] M. A. Tschopp and D. L. McDowell, "Asymmetric tilt grain boundary structure and energy in copper and aluminium," *Philosophical Magazine*, vol. 87, pp. 3871–3892, Sept. 2007.
- [49] D. Wolf, "Correlation between the energy and structure of grain boundaries in b.c.c. metals. II. Symmetrical tilt boundaries," *Philosophical Magazine A*, vol. 62, pp. 447–464, Oct. 1990.
- [50] D. Wolf, "Correlation between the energy and structure of grain boundaries in b.c.c. metals I. Symmetrical boundaries on the (110) and (100) planes," *Philosophical Magazine Part B*, vol. 59, pp. 667–680, June 1989.
- [51] D. Wolf, "Structure and energy of general grain boundaries in bcc metals," *Journal of Applied Physics*, vol. 69, p. 185, Jan. 1991.
- [52] J. Wang and I. J. Beyerlein, "Atomic structures of symmetric tilt grain boundaries in hexagonal close packed (hcp) crystals," *Modelling and Simulation in Materials Science and Engineering*, vol. 20, p. 024002, Mar. 2012.
- [53] J. Wang and I. J. Beyerlein, "Atomic Structures of [0-110] Symmetric Tilt Grain Boundaries in Hexagonal Close-Packed (hcp) Crystals," *Metallurgical and Materials Transactions A*, vol. 43, pp. 3556–3569, May 2012.
- [54] K. Kang, J. Wang, and I. J. Beyerlein, "Atomic structure variations of mechanically stable fcc-bcc interfaces," *Journal of Applied Physics*, vol. 111, no. 5, p. 53531, 2012.
- [55] G. I. Taylor, "The mechanism of plastic deformation of crystals. Part II. Comparison with observations," *Proceedings of the Royal Society of London. Series A, Containing Papers of a Mathematical and Physical Character*, pp. 388–404, 1934.
-

-
- [56] W. Read and W. Shockley, "Dislocation Models of Crystal Grain Boundaries," *Physical Review*, vol. 78, 1950.
- [57] D. Wolf, "A read-shockley model for high-angle grain boundaries," *Scripta Metallurgica*, vol. 23, pp. 1713–1718, Oct. 1989.
- [58] A. P. Sutton and R. Balluffi, *Interfaces in crystalline materials*. Clarendon Press, 1995.
- [59] J. H. van der Merwe, "On the Stresses and Energies associated with Inter-Crystalline Boundaries," *Proceedings of the Physical Society. Section A*, vol. 63, pp. 616–637, June 1950.
- [60] G. Schoeck, "The generalized Peierls–Nabarro model," *Philosophical Magazine A*, vol. 69, pp. 1085–1095, June 1994.
- [61] J. H. Van Der Merwe, "Crystal Interfaces. Part I. Semi-Infinite Crystals," *Journal of Applied Physics*, vol. 34, p. 117, Jan. 1963.
- [62] R. Bullough, V. Tewary, and F. Nabarro, "Dislocations in Solids," *FRN- Nabarro ~ North-Holland, Amsterdam*, 1979.
- [63] E. A. Holm, D. L. Olmsted, and S. M. Foiles, "Comparing grain boundary energies in face-centered cubic metals: Al, Au, Cu and Ni," *Scripta Materialia*, vol. 63, pp. 905–908, Nov. 2010.
- [64] D. Brandon, B. Ralph, S. Ranganathan, and M. Wald, "A field ion microscope study of atomic configuration at grain boundaries," *Acta Metallurgica*, vol. 12, pp. 813–821, July 1964.
- [65] D. Brandon, "The structure of high-angle grain boundaries," *Acta Metallurgica*, vol. 14, pp. 1479–1484, Nov. 1966.
- [66] P. Goodhew and D. Smith, "Can the CSL model fail?," *Scripta Metallurgica*, vol. 14, pp. 59–61, Jan. 1980.
- [67] V. Randle, "The coincidence site lattice and the 'sigma enigma'," *Materials Characterization*, vol. 47, pp. 411–416, Dec. 2001.
-

-
- [68] G. Bishop and B. Chalmers, "A coincidence — Ledge — Dislocation description of grain boundaries," *Scripta Metallurgica*, vol. 2, pp. 133–139, Feb. 1968.
- [69] G. H. Bishop and B. Chalmers, "Dislocation structure and contrast in high angle grain boundaries," *Philosophical Magazine*, vol. 24, pp. 515–526, Sept. 1971.
- [70] M. Weins, B. Chalmers, H. Gleiter, and M. Ashby, "Structure of high angle grain boundaries," *Scripta Metallurgica*, vol. 3, pp. 601–603, Aug. 1969.
- [71] M. Weins, H. Gleiter, and B. Chalmers, "Structure of symmetric tilt boundaries in F. C. C. metals," *Scripta Metallurgica*, vol. 4, pp. 235–238, Mar. 1970.
- [72] M. J. Weins, "Computer Calculations of the Structure and Energy of High-Angle Grain Boundaries," *Journal of Applied Physics*, vol. 42, p. 2639, Dec. 1971.
- [73] F. Frank, "The resultant content of dislocations in an arbitrary intercrystalline boundary," *Symposium on The Plastic Deformation of Crystalline Solids, Mellon Institute, Pittsburgh*, (NAVEXOS-P-834), 1950.
- [74] B. A. Bilby, "Report of the Conference on Defects in Crystalline Solids," Tech. Rep. 12, Physical Society, Dec. 1954.
- [75] W. Bollmann, *Crystal defects and crystalline interfaces*. Springer-Verlag, 1970.
- [76] A. J. Vattré and M. J. Demkowicz, "Determining the Burgers vectors and elastic strain energies of interface dislocation arrays using anisotropic elasticity theory," *Acta Materialia*, 2013.
- [77] A. P. Sutton, "An analytic model for grain-boundary expansions and cleavage energies," *Philosophical Magazine A*, Sept. 2006.
- [78] E. J. Widjaja and L. D. Marks, "Coincidence of reciprocal lattice planes model for quasicrystal-crystal epitaxy," *Physical Review B*, vol. 68, no. 13, p. 134211, 2003.
- [79] N. H. Fletcher, "Crystal interfaces," *Journal of Applied Physics*, vol. 35, no. 1, pp. 234–240, 1964.
-

-
- [80] J. Li, "Disclination model of high angle grain boundaries," *Surface Science*, vol. 31, pp. 12–26, June 1972.
- [81] K. K. Shih and J. Li, "Energy of grain boundaries between cusp misorientations," *Surface Science*, vol. 50, no. 1, pp. 109–124, 1975.
- [82] V. V. Bulatov, B. W. Reed, and M. Kumar, "Grain boundary energy function for fcc metals," *Acta Materialia*, vol. 65, pp. 161–175, Feb. 2014.
- [83] J. M. Ball and R. D. James, "Fine Phase Mixtures as Minimizers of Energy," *Analysis and Continuum Mechanics*, pp. 647–686, 1989.
- [84] M. Ortiz and G. Gioia, "The morphology and folding patterns of buckling-driven thin-film blisters," *Journal of the Mechanics and Physics of Solids*, vol. 42, pp. 531–559, Mar. 1994.
- [85] R. D. James and D. Kinderlehrer, "Theory of magnetostriction with applications to Tb x Dy 1-x Fe 2," *Philosophical Magazine Part B*, vol. 68, pp. 237–274, Aug. 1993.
- [86] B. Dacorogna, *Direct methods in the calculus of variations*, vol. 78. Springer Berlin, 1989.
- [87] H. Federer, *Geometric measure theory*. Springer, 1969.
- [88] G. Wulff, "Zur Frage der Geschwindigkeit des Wachstums und der Auflösung der Krystallflächen," *Zeitschrift für Kristallographie - Crystalline Materials*, vol. 34, Jan. 1901.
- [89] I. Fonseca, "The Wulff Theorem Revisited," *Proceedings of the Royal Society A: Mathematical, Physical and Engineering Sciences*, vol. 432, pp. 125–145, Jan. 1991.
- [90] C. Herring, "Some Theorems on the Free Energies of Crystal Surfaces," *Physical Review*, vol. 82, pp. 87–93, Apr. 1951.
- [91] J. W. Cahn and W. C. Carter, "Crystal shapes and phase equilibria: A common mathematical basis," *Metallurgical and Materials Transactions A*, vol. 27, pp. 1431–1440, June 1996.
-

-
- [92] J. Cahn and D. Hoffman, "A vector thermodynamics for anisotropic surfaces—II. Curved and faceted surfaces," *Acta Metallurgica*, vol. 22, pp. 1205–1214, Oct. 1974.
- [93] J. E. Taylor, "Crystalline variational problems," *Bulletin of the American Mathematical Society*, vol. 84, pp. 568–589, July 1978.
- [94] J. E. Taylor and J. W. Cahn, "Diffuse interfaces with sharp corners and facets: Phase field models with strongly anisotropic surfaces," *Physica D: Nonlinear Phenomena*, vol. 112, pp. 381–411, Feb. 1998.
- [95] W. K. Allard, "On the First Variation of a Varifold," *Annals of Mathematics*, vol. 95, no. 3, pp. 417–491, 1972.
- [96] F. J. Almgren, *Existence and Regularity Almost Everywhere of Solutions to Elliptic Variational Problems with Constraints*. American Mathematical Soc., 1976.
- [97] J. W. Cahn, "Transitions and phase equilibria among grain boundary structures," *Le Journal de Physique Colloques*, vol. 43, pp. C6–199–C6–213, Dec. 1982.
- [98] J. Hannon, M. Marcus, and V. J. Mizel, "A Variational Problem Modelling Behavior of Unorthodox Silicon Crystals," *ESAIM: Control, Optimisation and Calculus of Variations*, vol. 9, pp. 145–149, Sept. 2003.
- [99] N. Cabrera, "The equilibrium of crystal surfaces," *Surface Science*, vol. 2, pp. 320–345, Jan. 1964.
- [100] J. Gibbs, H. Bumstead, and W. Longley, *The collected works of J. Willard Gibbs*. Longmans, Green and Company, 1928.
- [101] A. Arya and E. Carter, "Structure, bonding, and adhesion at the ZrC (100)/Fe (110) interface from first principles," *Surface science*, 2004.
- [102] D. Jiang and E. Carter, "Prediction of strong adhesion at the MoSi₂/Fe interface," *Acta materialia*, 2005.
-

-
- [103] W. Donoghue, *Distributions and Fourier Transforms*. Academic Press, 1969.
- [104] W. Rudin, *Functional Analysis*. McGraw-Hill, 1973.
- [105] W. Rudin, *Real and Complex Analysis*. McGraw-Hill, 1966.
- [106] R. D. Levine and M. Tribus, "The Maximum Entropy Formalism," in *Maximum Entropy Formalism Conference (1978 : Massachusetts Institute of Technology)*, MIT Press, 1979.
- [107] E. Jaynes, "Information Theory and Statistical Mechanics," *Physical Review*, vol. 106, pp. 620–630, May 1957.
- [108] E. Jaynes, "Information Theory and Statistical Mechanics. II," *Physical Review*, vol. 108, pp. 171–190, Oct. 1957.
- [109] Y. Kulkarni, *Coarse-graining of atomistic description at finite temperature*. PhD thesis, California Institute of Technology, 2007.
- [110] R. K. Niven, "Jaynes' MaxEnt, Steady State Flow Systems and the Maximum Entropy Production Principle," *arXiv preprint arXiv:0908.0990*, p. 6, Aug. 2009.
- [111] E. M. Stein and G. Weiss, *Introduction to Fourier Analysis on Euclidean Spaces*. PRINCETON University Press, 1971.
- [112] D. Champeney, *Fourier Transforms and their Physical Applications*. Academic Press, 1973.
- [113] Y. Shibuta, S. Takamoto, and T. Suzuki, "A molecular dynamics study of the energy and structure of the symmetric tilt boundary of iron," *ISIJ international*, 2008.
- [114] R. T. Rockafellar, *Convex analysis*. Princeton Landmarks in Mathematics and Physics Series, PRINCETON University Press, 1997.
- [115] J. Ball, "A version of the fundamental theorem for Young measures," *PDEs and continuum models of phase transitions*, 1989.
-

-
- [116] T. Hsieh and R. Balluffi, "Observations of roughening/de-faceting phase transitions in grain boundaries," *Acta Metallurgica*, vol. 37, pp. 2133–2139, Aug. 1989.
- [117] G. S. Rohrer, "Grain boundary energy anisotropy: A review," *Journal of Materials Science*, vol. 46, pp. 5881–5895, June 2011.
- [118] H. Miura, M. Kato, and T. Mori, "Temperature dependence of the energy of Cu [110] symmetrical tilt grain boundaries," *Journal of Materials Science Letters*, vol. 13, pp. 46–48, Jan. 1994.
-